Mechanical properties of FDM-printed PLA, PETG and their various sandwich structures, composites, and recycled material structures

PhD Dissertation

by

Rawabe Fatima Faidallah

Gödöllő
2025

Doctoral school

Denomination: Doctoral School of Mechanical Engineering

Science: Mechanical Engineering

Leader: Prof. Dr. Gábor Kalácska, DSc
Institute of Technology
Hungarian University of Agriculture and Life Sciences,
Szent István Campus, Gödöllő, Hungary

Supervisors: Dr. Oldal István, and Dr. Zoltán Szakál
Institute of Technology
Hungarian University of Agriculture and Life Sciences, Szent István Campus,
Gödöllő, Hungary

……..…… ….....……

Affirmation of supervisor Affirmation of head of school

CONTENTS

NOMENCLATURE AND ABBREVIATIONS

Symbols

A_{cs}	sandwich specimens' cross-sectional area	mm^2
A_t	Cross-sectional area	mm^2
B	width of the specimens	Mm
E	Modulus of elasticity	MPa
F	Tensile force	N
H	thickness of the specimen	mm
h_c	Thickness of the core	mm
I	moment of inertia	mm^4
L	Span length between supports (bending test)	mm
L	Initial length before tensile test	mm
L0	length of the sample	mm
M	tangent's slope to the load-deflection curve's	N/mm
M	Maximum Bending Moment	N.mm
MBS	maximum bending strength	MPa
MCS	maximum compressive strength	MPa
P_{max}	maximum applied load	N
Pt	ultimate load	N
SD	standard deviation	g/mm^3
T	denotes the nominal thickness of the face	mm
t_{face}	thickness of the face sheets	mm
t_{core}	thickness of the core material	mm
V_L	Vertical compressive load applied over a large area	mm^2
V_s	Vertical compressive load applied over a small area	mm^2
ΔL	Deflection at the center	m
ΔL	Change in length after tensile test	mm

Greek symbols

Ɛb	strain at break	%
Ɛtb	nominal strain at break	%
Ɛtm	nominal strain at tensile strength	%
E	Strain	%
P	density	g/mm^3
ρ_{av}	density of the sandwich structure	g/mm^3
ρ_{pla}	density of the PLA material	g/mm^3
Σb	stress at break	MPa
σ_c	The compressive strength	MPa
σ_{face}	compressive strength of the face sheets	MPa
σ_t	tensile strength	MPa

Abbreviations

3D printing	Three-Dimensional Printing
ABS	Acrylonitrile Butadiene Styrene
AM	Additive Manufacturing
ASTM	American Society for Testing and Materials
CAD	Computer-Aided Design
CF	Carbon Fibre Reinforced

DLP	Digital Light Processing
FDM	Fused Deposition Modelling
FFF	Fused Filament Fabrication
HDPE	High Density Polyethylene
HIPS	High Impact Polystyrene
ISO	International Organization for Standardization
LOM	Laminated Objective Manufacturing
PA	Polyamide
PBF	Powder Bed Fusion
PC	Polycarbonate
PE	Polyethylene
PEI	Polyetherimide
PETG	Polyethylene Terephthalate Glycol
PEVA	Polyethylene Vinyl Acetate
PLA	Polylactic Acid
PMMA	Polymethyl Methacrylate
PP	Polypropylene
PS	Polystyrene
PTFCE	Polytrifluorochloroethylene
PTFE	Polytetrafluoroethylene
PVC	Polyvinylchloride
PVDC	Polyvinylidene Chloride
SD	Standard Deviation
SE	Secondary Electron
SEM	Scanning Electron Microscopy
SLA	Stereolithography
SLM	Selective Laser Melting
SLS	Selective Laser Sintering
STL	Surface Tessellation Language
UHDPE	Ultra High Density Polyethylene
UTS	Ultimate Tensile Strength
GF	Glass fiber
FRCs	Fiber-Reinforced Composites
FEA	finite element analysis
PET	polyethylene terephthalate
PEEK	polyether-ether-ketone
rPLA	Recycled polylactic acid
CF-PLA	carbon fiber-reinforced PLA
CF-PETG	carbon fiber-reinforced PETG
Wood/PLA	PLA-based with natural wood particles filament

1. INTRODUCTION, OBJECTIVES

This chapter describes the background and objectives of the current research.

1.1 Introduction

Additive manufacturing (AM) is the original title for what was previously known as rapid prototyping and has often been referred to as 3D printing. In many sectors, the phrase "rapid prototyping" (RP) has been used to describe a method for rapidly creating a prototype or part representation before final release or marketing. In the industry, this technique is called freeform manufacturing, layered fabrication, or additive layer manufacturing, direct digital manufacturing, quick manufacturing, and art-to-component production (Wimpenny et al., 2017). There are different methods of this technology: laminated object manufacturing (LOM) based on plastic lamination (Ahn et al., 2012), stereolithography apparatus (SLA) based on photopolymerization (J. Wang et al., 2016), selective laser sintering (SLS) (D. Slavko and K. Matic, 2010), and fused deposition modeling (FDM) (N. Turner et al., 2014) based on the melting of plastic filaments.

The FDM process is worked by extruding thermoplastic material, which has heated up to its melting point through a nozzle, then depositing the extruded layers of materials on top of each other. Currently, FDM is considered the most widely used technology of all types of 3DP technology around the globe due to the low cost of the printer device. Platform temperature, nozzle size, layer thickness, printing direction, nozzle head temperature, printing speed, and raster angle are parameters that could be controlled to improve print quality. Other researchers looked at the details of many processing parameters. According to the research, a suitable bed temperature and regulated convective heat transfer conditions can increase the bonding strength of successive layers, improving the mechanical properties of printed objects (Sun et al., 2008). Many process parameters can be controlled when producing 3D-printed part structures. Since then, the influence of process parameter settings on the mechanical qualities (e.g., tensile, flexural impact, compressive, and fatigue strength) has been described in thorough for various production scenarios. These parameters were exhaustively investigated for different categories of materials.

Tensile strength is a critical property of a material, defining its ability to withstand tension forces without failing. A deep understanding of tensile cracking and failure is essential, as these factors significantly impact the overall mechanical performance and structural integrity of materials (Onwubolu & Rayegani, 2014). Two leading organizations play a pivotal role in the field of additive manufacturing (AM): ASTM and ISO. Both are actively engaged in developing standards for the mechanical testing of AM materials and components. Their efforts focus on assessing the applicability of existing standards for mechanical tests on polymer-based AM materials and parts. These standards are divided into two primary categories: those specifically for plastics, such as D638 (ASTM, 2014) and ISO 527-2 (Iso, 2012a), and the other for composites, which include ASTM D3039 (International, 2007) and ISO527-4 (B. ISO, 2009; E. ISO, 1997).

Composite materials, created by combining different elements, play a crucial role in improving the structural and mechanical properties of engineering products. In industries such as automotive, aerospace, sports, and defense, fiber-reinforced polymer (FRP) composites are highly favored. These materials are prized for their lightweight, strength, and high tensile properties, offering a cost-effective and efficient manufacturing process. To meet growing industrial demand, large-scale production of fiber-reinforced polymers has become essential (Sonnenschein et al., 2016). Anisotropic by nature, FRP composite characteristics are influenced by the choice, volume, and

alignment of fibers, as well as the matrix's structural strength and form (J. H. Li et al., 2021). Reinforcing pure polymers with fibers yields substantial improvements in the mechanical attributes of printed polymer products. Glass fibers (GF), carbon fibers (CF), and Kevlar fibers are extensively harnessed for their reinforcing process in additive manufacturing (Faidallah et al., 2022a). These fibers, whether discontinuous or continuous, are used in Fiber-Reinforced Composites (FRCs) produced through various additive manufacturing (AM) techniques, including Fused Deposition Modeling (FDM). Continuous filament arrangement is achievable, but only with specialized printers, and even then, typically limited to a single plane. An example of such equipment is the Markforged line of composite 3D printers(*Markforged Composite and Metal 3D Printers*, n.d.).

3D printing technology has evolved to encompass the creation of a diverse array of application-specific components. Originally conceived to address the demands of product manufacturers, the multi-material concept capitalizes on the functional gradient adaptation inherent in the Fused Deposition Modeling (FDM. This adaptation enables the development of materials characterized by distinct gradients and compositions (Niu et al., 2022). The application of additive manufacturing in the production of multi-materials holds considerable promise across various industries, including medical (for bio-implants), construction (for structures), automotive (for wear-resistant coatings), and industrial 4.0 (for drones) (Faidallah et al., 2022b) (Salcedo et al., 2018).

This research will lead to better control and optimization of the 3D-printed polymer specimens using Fused Deposition Modeling (FDM) to investigate the impact of various tensile geometry shapes and printing parameters on the tensile properties. Additionally, Finite Element Method (FEM) simulations will be conducted to compare the different geometries.

The study also outlines the development of fiber-reinforced polymer composites. Laboratory re-manufacturing of pure filaments and filaments reinforced with fiber will be conducted to evaluate their tensile strength after recycling. furthermore, various compositions of functionally graded multi-materials with different gradient arrangements, including single and multiple gradients, will be created and examined for their tensile and compressive properties.

Moreover, rhombus and honeycomb structures will be designed and produced using FDM printing technology. The mechanical performance of these materials will be evaluated through tensile, three-point bending, and compression tests, with the failure modes of the specimens analyzed for each test. Furthermore, auxetic honeycomb cores will be examined to evaluate the effects of varying face layer thicknesses on three-point bending strength, considering both in-plane and out-of-plane core orientations. Compressive strength will be tested in both flatwise and edgewise positions. Additionally, finite element analysis (FEA) will be performed to gain deeper insights into stress distribution under bending and compressive loads.

This research aims to enhance the control and optimization of 3D printing parameters for polymers, while deepening our understanding of reinforcement polymer, sandwich structures, and multi-material compositions of polymeric elements. As an innovative cross-disciplinary study, it will gather unique testing data that integrates mechanical and chemical characteristics. Based on these results, recommendations will be developed for mechanical applications. The findings will be precious for industrial producers increasingly utilizing advanced additive manufacturing technologies not only for rapid prototyping but also for the production of multi-material composite products.

1.2 Objectives

FDM 3D printing techniques will be employed to print specimens using various materials and different manufacturing processes. The produced samples, with this variety of conditions, will be subject to mechanical tests. The main objectives of the present work are to investigate the following:

a) How do different tensile geometry shapes and printing parameters impact the tensile properties of PETG specimens produced using FDM, and how do these variations compare through FEM simulations?

b) How does adding fibers into polymer affect the tensile and compressive properties in different build orientations?

c) What is the impact of recycling filaments and reinforcing them with natural fibers on their filament's tensile strength?

d) How do different sandwich structures, such as honeycomb and rhombus core designs, affect the mechanical properties of PLA materials?

e) How does varying the face layer thickness of re-entrant honeycomb cores in Wood/PLA polymer affect their three-point bending and compressive strengths, and what insights can finite element analysis provide on stress distribution under these loading conditions?

f) What are the effects of different gradient arrangements in functionally graded multi-materials on their tensile properties?

2. LITERATURE REVIEW

This chapter offers a comprehensive overview of 3D printing processes, detailing the primary methods, materials used (with a focus on polymers), and their applications across various industries. It will also introduce sandwich structures, multi-materials, and the properties of recycled filaments, emphasizing the mechanical behaviour of 3D-printed polymer composites and the influence of their structures. Additionally, it will identify the gaps and challenges highlighted in the literature, which have motivated the initiation of this research.

2.1 History of 3D printing

3D printing, often referred to as additive manufacturing, has emerged as a creative process for crafting parts or components with intricate designs. Its appeal lies in its capacity to facilitate rapid prototyping and fabricating customizable elements. This means that designers can quickly produce different iterations of their ideas, allowing for cost-effective testing and evaluation. By leveraging this technology, creators can explore innovative concepts that may not have been achievable through traditional manufacturing methods(Ligon et al., 2017). The foundational principles of additive manufacturing (AM) were initially explored over 50 years ago. The 1980s and 1990s marked significant periods of innovation and expansion in the realm of 3D printing. Charles Hull, who invented the first kind of 3D printing, stereolithography, developed this technology in the late 1980s and early 1990s (SLA) (Wimpenny et al., 2017; Wohlers & Gornet, 2011), followed by the invention of other techniques like fused filament fabrication (FFF) and selective laser sintering (SLS) (Wohlers & Gornet, 2014). During the late 1990s, numerous iterations of 3D printing methods emerged and evolved rapidly, driven by advancements in computer technology. As the new millennium approached, industries such as medicine and aerospace began to widely explore the potential of 3D printing techniques. Simultaneously, the expiration of patents related to early 3D printing methods enabled many companies to develop their own brands of 3D printers, making this technology more accessible to the public. Post-2010, the widespread availability of 3D printing techniques has spurred the development of advanced printing methods with improved accuracy, precision, and speed.

Initially, AM techniques primarily utilized existing polymer materials adapted for 3D printing. However, there is now a growing emphasis on the development of specialized polymers tailored specifically for 3D printing applications, signifying a shift towards dedicated polymer development for additive manufacturing. Figure 2.1 provides an overview of the progression of 3D printing technology alongside the evolution of polymer materials.

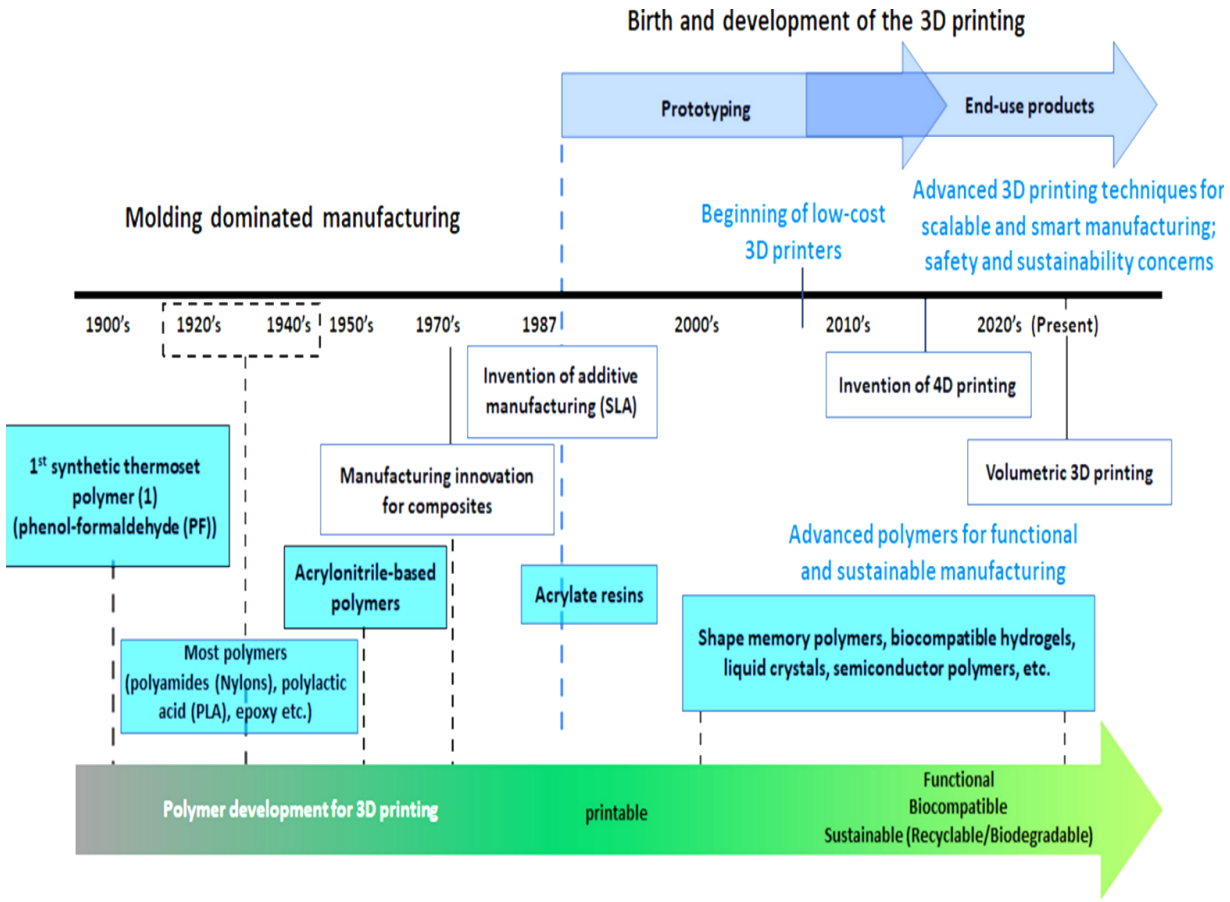

Fig. 2.1 Illustrates the historical trajectory of 3D printing and the evolution of polymer materials tailored for additive manufacturing, transitioning from rapid prototyping to scalable and customizable production (Park et al., 2022)

Today, research papers often document the properties of experimental materials used in 3D printing, most of which are developed in universities and research centers with outstanding results. The availability of commercial materials varies widely depending on the 3D printing technology used. The primary polymers employed in 3D printing are thermoplastic and thermosetting resins, each offering unique properties suitable for different technologies. Thermoplastics, which can be semi-crystalline or amorphous, can undergo multiple cycles of melting and solidification for recycling because their solidification process is reversible, without forming chemical bonds. However, each cycle typically leads to some degradation of properties. In contrast, thermosetting plastics undergo a curing process induced by heat, light, or radiation, which causes crosslinking. This crosslinked structure gives thermosetting plastics excellent engineering properties but makes them non-recyclable, as they only break down at high temperatures.

2.2 3D printing technologies

3D printing technology has recently gained significant popularity because of its simplicity and versatility. It is now applied across various fields, such as education, prototyping, construction, medicine, and the aerospace industry, among others. This technology enables the production of lightweight components that improve fuel and energy efficiency. Additionally, 3D printing permits

the customization of materials to attain specific properties like water repellency, enhanced strength, and heat resistance.

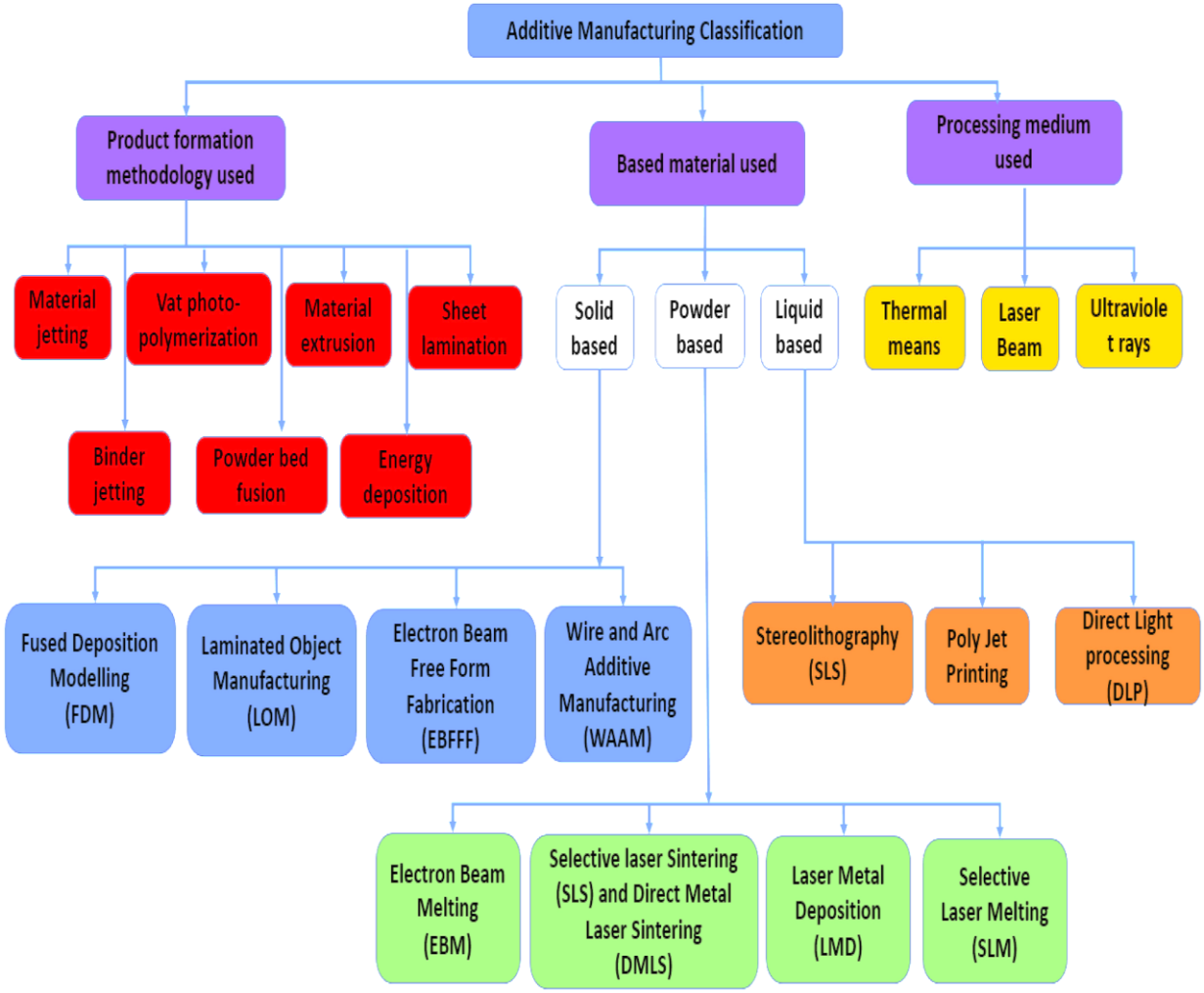

Fig. 2.2 Illustrates various contexts for classifying additive manufacturing processes.(Salifu et al., 2022)

The adaptability of additive manufacturing (AM) has made it a favored technology across various sectors, supporting the use of a wide array of materials, including ceramics, metals, polymer composites, hybrids, functionally graded materials, and hydrogels in forms such as liquid, solid, gel, and viscoelastic states. The flexibility of AM techniques enables diverse classification methods, as illustrated in Figure 2.2. As per ASTM F2792-12a, there are over 50 unique AM technologies, prompting ASTM to create standardized classifications that group AM processes into seven main categories (ISO/ASTM 52900:2015):

- Jetting
- Binder Jetting
- Powder Bed Fusion
- Vat Photopolymerization

- Directed Energy Deposition
- Material Extrusion
- Sheet Lamination

AM techniques are also categorized based on the processing medium, including ultraviolet light, thermal energy, or laser beams (Chiulan et al., 2017). Critical factors for evaluating these technologies include mechanical strength, fabrication speed, precision, cost, build size, surface finish, and overall quality. As these criteria continue to advance, AM is increasingly enabling the efficient and flexible production of larger and more intricate products.

2.2.1 Laminated object manufacturing (LOM)

, as illustrated in Figure 2.3. LOM combines additive and subtractive techniques to build parts layer by layer from sheet materials, bonded by heat, pressure, and adhesive, and cut by a CO_2 laser (Figure 2.3). It is low-cost, doesn't need supports, and can produce large parts without deformation, but results in low surface sharpness, directional material properties, and difficulty with complex cavities. It applies to paper, metal, and composite materials.

2.2.2 Stereolithography apparatus (SLA)

SLA uses lasers or projectors to cure photopolymer resin layer by layer(Castoro & Kumpaty, 2013; Kang et al., 2018). After each layer, the platform lowers into the resin to form the next. Size limitations, sensitivity to light, and uneven resin spreading are challenges. SLA is widely used for dental applications and small component fabrication like gold molds (Araya-Calvo et al., 2018; Nandi et al., 2017).

2.2.3 Selective laser sintering (SLS)

Selective Laser Sintering (SLS) is a method that employs a laser to fuse powder into a solid object, layer by layer (Technologies & Terminology, 2012). A powder vat spreads layers as the platform moves along the z-axis. Similar to SLM and EBM, it can produce end-use metal parts. Surface properties can be improved post-process with coatings like cyanoacrylate or epoxy (Y. Liu et al., 2017; Technologies & Terminology, 2012), as shown in Figure 2.3.

2.2.4 Inkjet printing and contour crafting (IJP)

In IJP, resin is extruded through a micro-nozzle to form layers following part contours and cured either by air or UV light for better strength (Shahrubudin et al., 2019), as shown in Figure 2.3.

2.2.5 Binder Jetting

Binder Jetting selectively applies a liquid binder onto thin layers of powder (ceramics, metals, sand, or composites) to form solid parts layer by layer (Gibson et al., 2021; Shahrubudin et al., 2019). The binder holds the powder together until final solidification (Figure 2.3).

2.2.6 Directed energy deposition

DED uses focused energy (laser or electron beam) to melt metal wire or powder, adding or repairing material with precision. Unlike extrusion, the nozzle moves freely. Technologies like LENS and laser deposition enable manufacturing from millimeters to meters, used widely in aerospace, transportation, and tooling (Dilberoglu et al., 2017; Shahrubudin et al., 2019). 3D printing technologies are illustrated in Figure 2.3.

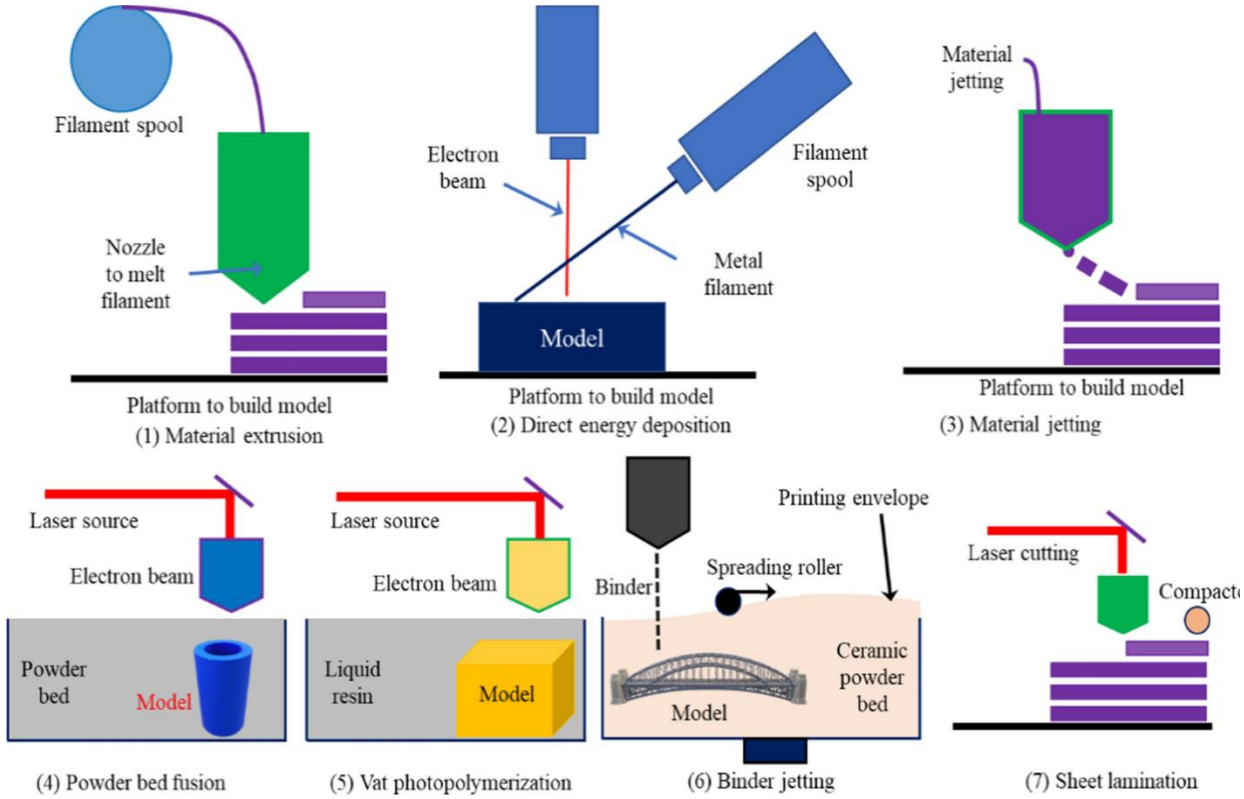

Fig 2.3 A schematic overview of the currently available 3D printing processes (Latha et al., 2024)

2.2.5 Fused Deposition Modeling (FDM) based on the melting of plastic filaments:

The FDM process is worked by extruding thermoplastic material, which uses thermoplastic filament as feedstock, the filament has heated up to its melting point and then is extruded through a nozzle in the XY plane creating a layer of solid material on the build plate. Creating a model can be done by depositing a layer contour, and then filling the inside with plasticized material by the zigzag movement of the head. After printing one layer the head moves along the Z-axis initiating the build-up of the next layer. Using this technique, we can create complex shapes with a minimum of preparatory processes. The production process begins with creating a model in the CAD program, then the model is incorporated into the program enabling control of process parameters such as head movement, feed rate, layer thickness, infill, head and table temperatures, slicing, support application, etc. Such a program generates a G-code, which is uploaded to a 3D printer enabling making a real model. The model removed from the printer needs finished machining, for instance, to remove the supports and imperfections (Bakarich et al., 2014; Dudek, 2013) .

For some designs, support materials can be easily removed but removing them from complex structures can be challenging. Ultimaker has addressed this issue by developing a water-soluble support material that dissolves completely, leaving no residue and resulting in a clean part. This innovation allows for the easy creation of dynamic structures. The accuracy of the printed part depends on several factors, including the movement of the extruder, the temperature, the speed, and the flow rate of the material through the nozzle. FDM technology (Figure 2.4) is extensively used for creating anatomical models in dentistry and for surgical exercises (Mostafa et al., 2009).

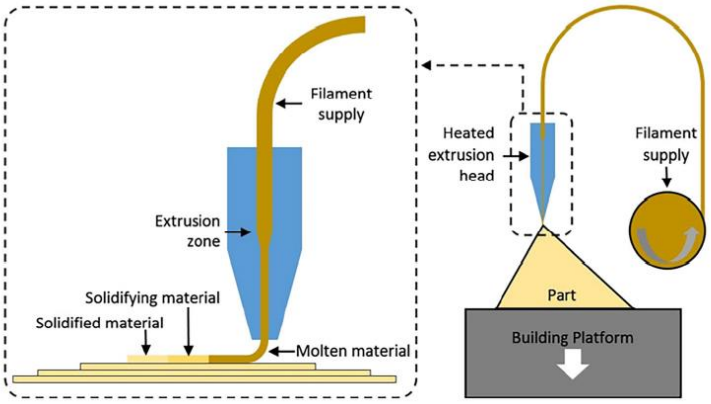

Fig. 2.4 Fusion deposition Modelling (FDM) (Penumakala et al., 2020)

2.3 Additive manufacturing using polymers

AM using polymers can be carried out successfully using a variety of polymer materials in different forms and compositions including their composites, nanocomposites, continuous/discontinuous fiber-reinforced thermoplastic composites, and hybrids. The most widely used polymer 3D printing methods and processing techniques used across polymer industries along with major global 3D printer manufacturers are highlighted in Table 2.1.

Table 2.1. Polymer additive manufacturing process and global 3D printer manufacturers (Salifu et al., 2022).

Methodology of for Mation of the Product	**Polymer AM Process Technique**	**Polymer Used**
Matrix Extrusion	Fused deposition modeling, FDM	ABS, PEEK, PC, PC-ABS, PLA, Nylon 12/Carbon Fiber, HIPS, TPU, ASA, PEEK, PEI
Vat Polymerization	Stereolithography, SLA	liquid UV-curable photopolymers Somos® stereolithography (SLA) materials Somos® 9120 (off white), Somos® BioClear (clear), Somos® Element (clear), Somos® EvoLVe 128 (white), Somos® NeXt (white), Somos® WaterClear Ultra 1012
Powder Bed Fusion	Selective laser sintering, SLS	The polymer in powder forms polycarbonate (PC) nylons (polyamide (PA)), acrylic styrene (PMMA/PS), polyamides(PA), polystyrenes(PS), thermoplastic elastomers(TPE), polyaryletherketones (PAEK)
	Multi jet Fusion	

Material Jetting	Material Jetting	Polyamide (PA12/Nylon 12), Elastic TPU Vero, Tango, Durus, Digital ABS

The most common thermoplastic polymer materials used in FDM processes are acrylonitrile butadiene styrene (ABS), polylactide (PLA), polyamide (Nylon), nylon 12, polycarbonate (PC), glass-filled nylon, and epoxy resin. Some of the commercial polymer materials that are most popular in the FDM process include ABS_M30 and polycarbonate (PC) (Jasiuk et al., 2018). Typical properties of AM components manufactured using various commercial polymers based on the datasheets of EOS GmbH; Stratasys, USA, and SYS are presented in Table 2.2 The polymers used in AM processes can be rationally classified as thermoplastics, particle-reinforced polymer composites, polymer matrix composites, fiber-reinforced polymer composites, thermo-responsive polymers, nanocomposites, and thermoplastic elastomers composites.

Table 2.2 Properties of commercial polymers used in additive manufacturing processes (Faidallah et al., 2022a).

Properties	**ABS**	**PLA**	**PC**	**Nylon12**	**PA11**	**PA23**	**Protogen O-XT 18240**	**WaterClear Ultra 10122**	**sDurus White**	**Vero RGD**	**RGD 525**
Tensile Modulus (MPa)	1627	2347	1944	1282	1600	1650	2960	2880	1200	3000	3500
Tensile Strength (MPa)	22	50	40	32	48	48	68	56	30	65	70
Density (kg/m3)	1050	1240	1200	950	990	930	1160	1130	1170	1190	1180

When choosing the right polymer for the finished product, it is important to know material properties (physical and mechanical properties) and printability. Figure 8a shows the most common types of thermoplastics, which are classified according to performance, and Figure 2.5.a presents their printability, visual quality, and mechanical properties. In Figure 2.5.b, heat resistance, impact resistance, and elongation break are the chemical and mechanical properties that resist higher temperatures, impact energy, and length deformation before breaking, respectively. The ease of printing means how easy it is to print a feedstock in terms of bed adhesion, maximum print speed, ease of feeding to the printer, and the frequency of print failures, and visual quality refers to how good the printed part looks, which is determined by the surface quality such as smoothness of the surface. These points of view will help choose materials for FDM.

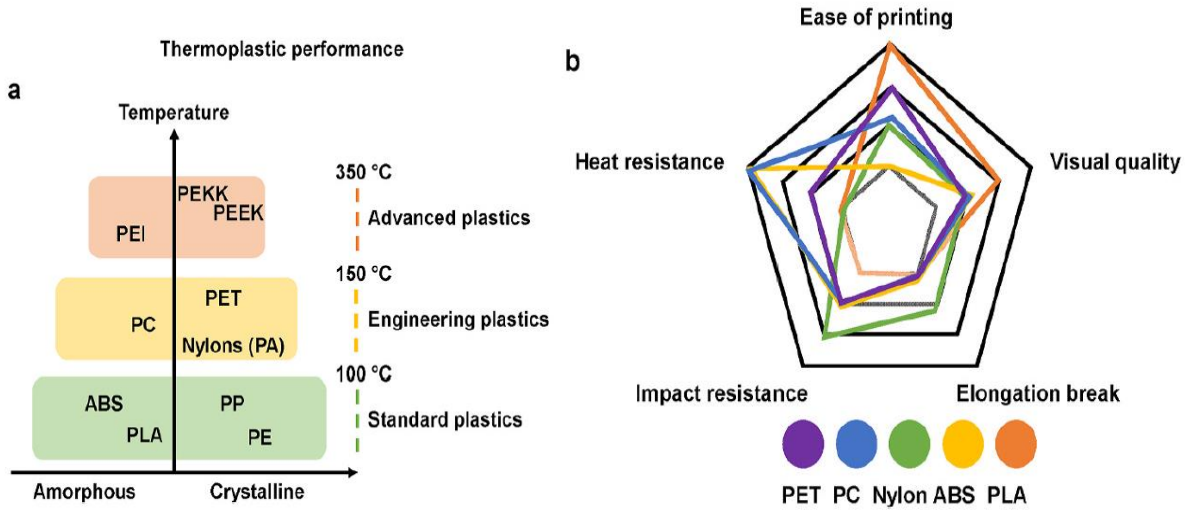

Fig. 2.5. Thermoplastics as feedstock materials for FDM. (a) Categories of thermoplastics: Standard plastics (b) A Rader plot graph showing polymer properties in terms of ease of printing, visual quality, elongation break, impact resistance, and heat resistance.(Faidallah et al., 2022a)

While: Acrylonitrile butadiene styrene (ABS), polylactic acid (PLA), polypropylene (PP), and polyethylene (PE)) are used for general parts operated under low stresses. Engineering plastics (Polycarbonate (PC), polyethylene terephthalate (PET), nylon (PA)) have good wear resistance compared to standard plastics and are applied to structural parts. Advanced plastics (Polyethyleneimine (PEI), polyether-ether-ketone (PEEK)) have high-temperature resistance as well as high wear and chemical resistance.

Fiber-reinforced polymer composites (FRPCs) are advanced materials made by combining a polymer base with strong reinforcing fibers like glass or carbon. Thanks to this combination, they offer an ideal balance of strength and lightness, making them especially valuable in applications where durability and efficiency are essential.

2.4 Additive manufacturing techniques for FRPC

According to the ASTM International Technical Committee, F42 with AM technologies (ASTM, 2007, p. 42), AM techniques for FRPC have been generally categorized into four processes: material extrusion, vat photopolymerization, sheet lamination, and powder bed fusion. Table 2.3 highlights the advantages and disadvantages of various AM methods for FRPC and offers a review of different AM techniques for FRPC.

Table 2.3. Different additive manufacturing techniques for composite materials with their advantages and disadvantages (Goh et al., 2019; Zindani & Kumar, 2019).

Techniques	Advantages	Disadvantages	Fiber alignment
Laminated object manufacturing	• Low cost. • Parts with high strength can be produced. • No requirement for post-processing. • No requirement for support structures.	• Higher wastage of material. • It is relatively difficult to build parts with complex cavities.	• Random fiber orientation • Uniform direction of the fiber

Powder bed fusion	• Support structures can be removed easily. • Composites with higher reinforcement of loading can be achieved. • Fine resolution. • Powders that remain unused can be used again.	• Rough surface finish. • Slow printing. • Not possible to fabricate composites. with long fibers. • Expensive. • High porosity in the final parts.	• Random fiber orientation
Vat photopolymerization	• Fibers can be aligned randomly. • Finer resolution	• The formation of bubbles takes place. • Limited materials can only be used. • Sedimentation of fiber in resin. • Increased resin viscosity with the addition of fibers. • The issue with the penetration of UV rays.	• Random fiber orientation. • Along the direction of the electric field. • Along the direction of the magnetic field. • Along the direction of laying. • By the fiber pattern of the mat.
Material extrusion	• Easy to fabricate. • Economical. • Multi-material capability. • Print-heads can be easily modified.	• Degradation of the nozzle. • Obvious layer-by-layer effect. • At higher reinforcement loading, the nozzle gets clogged.	• Along the direction of printing.

In their reviews, (Goh et al., 2019; Zindani & Kumar, 2019) have outlined possible future research directions for the FDM 3D printing technology of fiber-reinforced polymer composites These potentials include material development, fiber-matrix interfacial properties, fiber homogeneity, fiber alignment, interlayer bonding, porosity, and printability. Researchers also discussed challenges related to natural fiber reinforcement in FDM printing (Mazzanti et al., 2019). Furthermore, a concept map illustrating critical factors for fabricating composites using AM techniques is depicted in Figure 2.6.

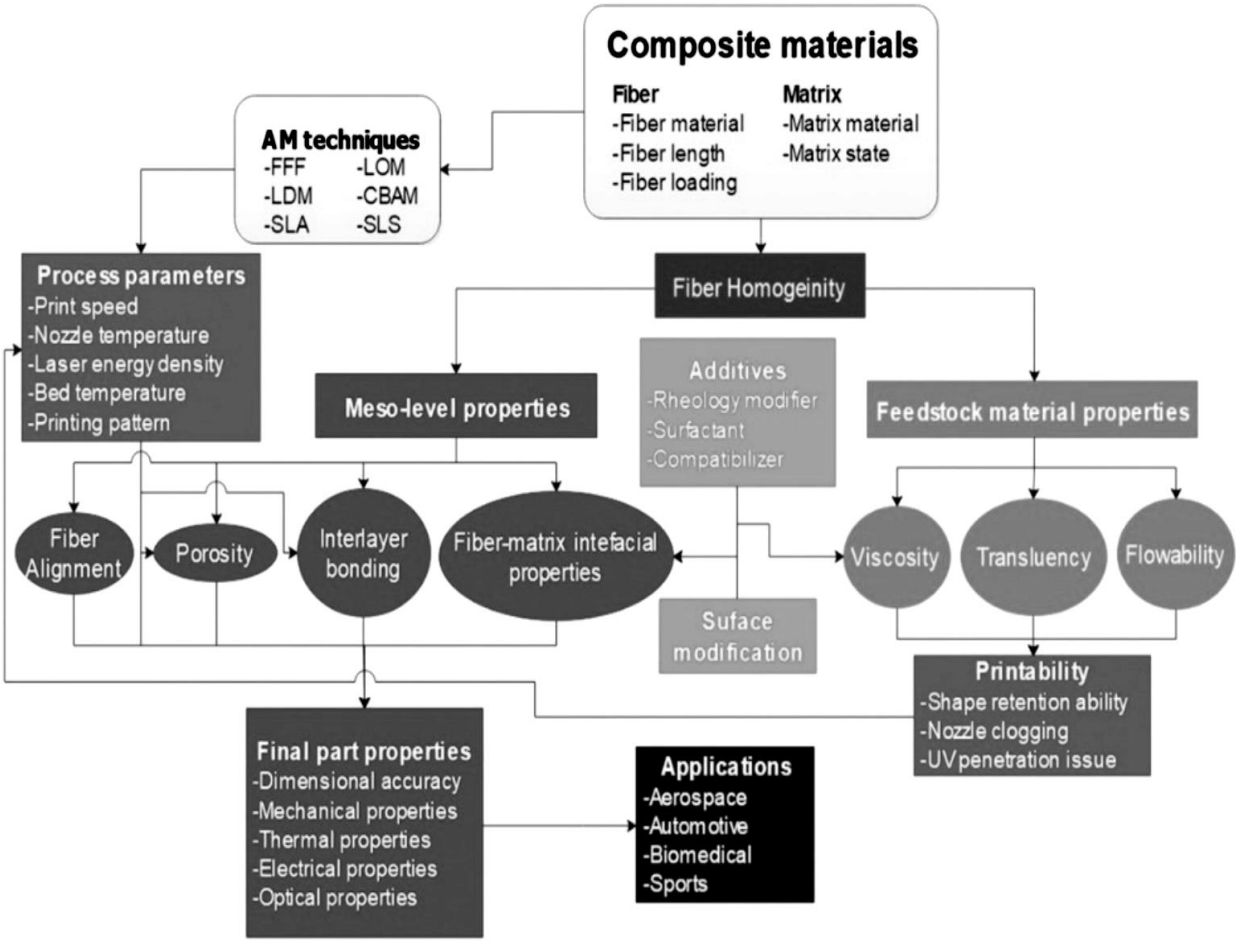

Fig. 2.6. Concept map detailing the essential factors in producing composites through AM techniques." (Mazzanti et al., 2019)

2.4.1 Fiber-reinforced polymer in FDM manufacturing.

This technique, known as Fused Deposition Modeling (FDM) (Figure 2.7), involves melting and extruding filament. Extrusion-based methods are cost-effective and relatively straightforward. Short fiber-reinforced composites can be extruded without modification, while continuous fiber-reinforced composites require only minor adjustments to the print head. Additionally, this technique can be easily adapted for multi-material printing by using multiple nozzles. However, a notable drawback of FDM is the visible layering effect in the final printed parts. This section focuses on the development of new fiber-reinforced polymer (FRP) composite materials, incorporating both nanoscale discontinuous fibers and continuous fibers, using the FDM technique.

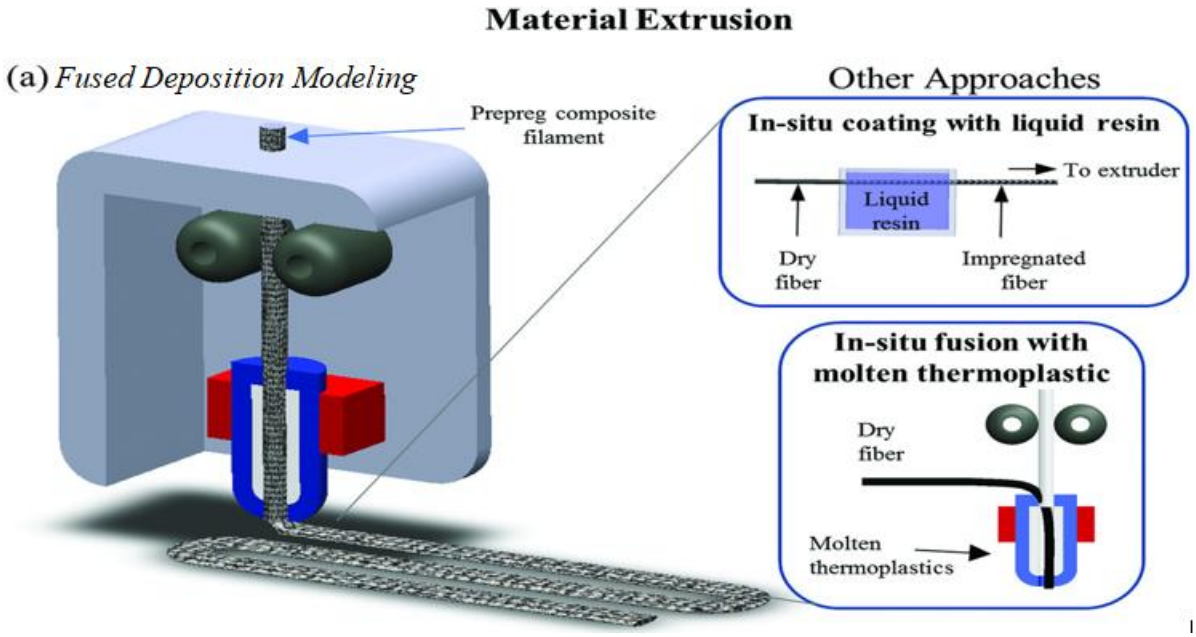

Fig. 2.7 Material extrusion process (Goh et al., 2019).

Figure 2.7 illustrates three methods for producing composite components through Fused Deposition Modeling. These methods include the extrusion of prepreg composite filament, the in situ coating of fibers with liquid resin, and the in situ fusion of fibers with molten thermoplastics. In this process, the nozzle is heated to melt the thermoplastic filament, which is then deposited selectively.

The Fused Deposition Modeling has been used to develop fiber-reinforced composite materials ranging from nano-scale to continuous fiber form. Carbon, glass, fibers of thermotropic liquid crystalline polymers in long chopped for or in the millimeter range, iron, metallic powders of copper in the micrometer range, graphene, and multi-walled and single-walled carbon nanotubes, are some of the materials that have been researched for the fabrication of composites through the fused filament fabrication technique. The commonly used matrix materials are thermoplastics. A few examples of thermoplastics requiring low processing temperatures include polypropylene, poly-lactic acid, nylon, and acrylonitrile butadiene styrene (Zindani & Kumar, 2019).

Fused Deposition Modeling is convenient for short fiber-reinforced polymeric composites. This is because they are extruded in a normal filament without need for an extra layer. However, the Fused Deposition Modeling suffers from voids and porosity. Reduced tensile strength and delamination results owing to the formation of voids in between the extruded filaments (Shofner et al., 2003). Incorporating reinforcements along the filament direction is more effective because the fibers tend to align with the direction of extrusion, resulting in improved anisotropy of mechanical properties (Dul et al., 2016).

Fiber loading is another relevant area of research that has been investigated extensively and has been demonstrated to be dependent on the reinforcement–matrix combination. Elastic modulus increases with the fiber loading up to a certain threshold limit. wettability of the fibers with the matrix materials is the cause to be attributed to the poor fiber-matrix interface. An increase in fiber loading results in increased matrix viscosity and lower flowability. This may lead to clogging of

the nozzle. Plasticizers and surfactants may be added to enhance fiber-matrix bonding. This will result in better processability of the material. The addition of Buna-N and linear low-density polyethylene were added as compatibilizers and toughening agents respectively with the reinforcing material in ABS. The tensile strength was reported to be enhanced with the addition of 1 wt% hydrogenated Buna-N and 30 wt% of linear low-density polyethylene (Goh et al., 2019; Zindani & Kumar, 2019).

The interface between fiber and matrix material has significant influences on tensile strength. The distribution of fibers was therefore also influenced whereas the fibers were generally oriented in the middle of the extrusion line (Griffini et al., 2016; Hofstätter et al., 2016). The interface between the layers was indistinct due to the remelting of material during the extrusion of the next layer, allowing for a continuous matrix material. This also resulted in an interconnected orientation of longitudinally oriented and orthogonally oriented fibers.

FDM manufacturing using CF in ABS is achievable and can result in an improved tensile strength of 42MPa at a fiber volume weight of 5% as shown by (Ning et al., 2017), The tensile strength was 34 MPa at a fiber content of 10% weight, which is closer to the tensile strength of pure ABS (depending on the composition of the ABS). With 7.5 percent fiber content in weight and a value of 2.5 GPa, Young's modulus was the highest. When fibers were added to pure ABS, toughness, and yield strength were reduced. In (Ning et al., 2015) the study showed that the influence of carbon fiber ratios and fiber length on the tensile and flexural properties of FFF-built ABS-carbon manufactured parts is investigated. Flexural stress, tensile stress, flexural modulus, and flexural toughness are all highest with a carbon fiber loading of 5%. However, Young's modulus was at its maximum value with 7.5 % carbon fiber volume in the composite, Because of the high porosity, most of the tensile and flexural parameters are at least at a 10% carbon fiber ratio. With increasing carbon contents and fiber length, ductility diminishes.

The feature described above also affects ductility. Experiments were performed with fiber lengths of 150 μm, resulting in a higher Young's modulus than with 100 μm (Ning et al., 2015), longer fibers increase stiffness and strength but reduce ductility compared to shorter fibers, highlighting a trade-off between mechanical reinforcement and material toughness.) It was concluded that adding carbon fibers to plastic materials can lead to improved tensile properties compared to pure plastic specimens.

Fused Deposition Modeling (FDM) using ABS reinforced with short glass fibers has shown promising results, with the material capable of incorporating up to 30% fiber content by weight (Zhong et al., 2001a). By treating ABS with plasticizers and compatibilizers, a more uniform distribution of fibers can be achieved, enhancing the overall quality and performance of the material. This results in consistent and predictable mechanical properties throughout the entire finished product.

PLA can be reinforced using short carbon fibers or continuous jute yarns. Carbon fibers greatly enhance tensile strength (by 435–599%) and stiffness due to their high load-bearing capacity, while jute fibers provide a more sustainable alternative but contribute less to tensile strength. Continuous fiber reinforcement generally outperforms conventional polymer composites in mechanical performance. Investigations using PLA with an embedded continuous fiber is presented in (N. Li et al., 2016b) concluded a weak interface between the fiber and the matrix and flexural strengths increased from 13.8 to 164% and storage moduli from 166% to 351% increase

compared to conventional parts. A general overview of the use of continuous fiber in a PLA matrix is given by (Bettini et al., 2017).

The fused filament fabrication process has been used for the fabrication of continuous fiber reinforced polymeric composites (Melenka et al., 2016; C. Yang et al., 2017). Additive manufacturing can simply be accomplished by a simple modification of the print head. Several different approaches have been adopted to print continuous fiber-reinforced polymeric composites, including extrusion, in situ consolidation of fibers and thermoplastic at the nozzle (Dul et al., 2016; Tian et al., 2016; C. Yang et al., 2017), and in situ fusion of fibers and thermoplastics before extrusion. In the case of in situ consolidation, viscosity affects both the traction force and the resin's viscosity. During in situ fusion at the nozzle, fibers are fused with the resin and extruded automatically without the need for a feeding device. Mechanisms such as resistive heating laser cutting (Goh & Yeong, 2018) and mechanical cutting (Der Klift et al., 2016) are required to cut the fibers at the end of each composite layer. Using continuous fibers as reinforcements results in significant improvements in tensile properties (Ivey et al., 2017). Table 2.4 presents the mechanical characteristics of composites produced through FDM manufacturing methods.

Table 2.4. Mechanical properties of composites fabricated using FDM manufacturing techniques.

Composite composition	**Mechanical Properties**	**Reference**
Carbon fiber reinforced with Nylon Glass fiber reinforced with Nylon Kevlar fiber reinforced with Nylon	Impact strength of 82.26 kJ m^{-2} Impact strength of 280.95 kJ m^{-2} Impact strength of 184.76 kJ m^{-2}	(Caminero et al., 2018).
e-glass fiber in polypropylene	Flexural modulus of 13.06 GPa	(Low et al., 2017)
Carbon fiber in ABS Carbon fiber in PETG Carbon fiber in PLA	Ultimate tensile strength of 574.44 MPa Young's modulus of 25.86 GPa Ultimate tensile strength of 69 MPa Young's modulus of 8.5 GPa Ultimate tensile strength of 69 MPa Young's modulus of 9 GPa	(Jiang & Raney, 2019)
Glass fiber and Nylon	Ultimate tensile strength of 575 MPa Young's modulus of 25.86 GPa Poisson's ratio of 0.37 Shear strength of 67.77 MPa Compression strength (0°) of 82 MPa Compression strength (90°) of 12.73 MPa	(Goh et al., 2018)
carbon fiber and Nylon	Ultimate tensile strength of 701 MPa Young's modulus of 68.08 GPa Compression strength (0°) of 223.06 MPa Compression strength (90°) of 41.83 MPa Poisson's ratio of 0.35	(Goh & Yeong, 2018)

Bundles carbon fibers with epoxy resin	Ultimate tensile strength of 792 MPa Young's modulus of 161 GPa	(Hao et al., 2018)
Carbon Fiber in polylactic acid Bundled carbon fiber in ABS Bundled carbon fiber in PLA	Ultimate tensile strength of 91 MPa Flexural strength of 156 MPa Enhanced strength Ultimate tensile strength of 90 MPa Young's modulus of 5.8 GPa Tensile modulus of 294 MPa	(N. Li et al., 2016b)
34.5% Carbon fiber and Nylon	Ultimate tensile strength of 475 MPa Young's modulus of 35.7 GPa Enhance tensile modulus	(Der Klift et al., 2016)
0.5 wt5 CNT in PLA 6 wt% CNT in ABS	Ultimate tensile strength of 80 MPa Young's modulus of 1.99 GPa Ultimate tensile strength of 47.1 MPa Young's modulus of 2.625 MPa	(Melenka et al., 2016)
1 wt% CNT in PEEK	Shear strength of 27 MPa Ultimate tensile strength of 70 MPa	(Berretta et al. 2017)
5.6 wt% Graphene in ABS and PLA	Higher mechanical strength was achieved	(Wei et al., 2015)
4 wt% Glass fiber in PLA	Ultimate tensile strength of 30 MPa Young's modulus of 4 GPa Impact strength of 60 Jm^{-1}	(N. Li et al., 2016a)
Carbon fiber in ABS	Ultimate tensile strength of 38 MPa Young's modulus of 5.9 GPa Shear strength of 13 MPa	(Z. Zhang et al., 2018)
10 wt% Carbon fiber in the millimeter scale in PA 12	Ultimate tensile strength of 90 MPa Young's modulus of 3.5 GPa	(Liao et al., 2018)
Carbon fiber in the millimeter scale in ABS	Ultimate tensile strength of 70 MPa Young's modulus of 8.91 GPa	(Zhong et al., 2001a)

2.4.2 Fiber materials

Natural fibers and synthetically manufactured fibers are the two types of fibers available. Natural fibers, the first type, may be further divided into plant fibers and animal fibers. Plant-derived cellulose fibers are a common example (Le Duigou et al., 2016; Matsuzaki et al., 2016). Synthetic fibers may be made in both dry and wet situations. They have been formed into filaments, ropes, or strings after fabrication (Shubhra et al., 2013). Carbon fiber-reinforced plastics are widely utilized in the industry (CFRP)(Serrano et al., 2014). Among other things, they're used in the Airbus A350 airliner, wind turbine blades, endoscopic surgery, and automobile components (Biron, 2012; Dave & Davim, 2021). The use of glass fibers in combination with additive manufacturing technologies has also been studied (Garoushi et al., 2013; Van der Zwaag et al., 2014; Zhong et al., 2001b). This had been covered in the FRP in the FDM Manufacturing section Long glass fibers allow information to pass through the materials and, as a result, communication to pass through the matrix material (Monaghan et al., 2015).

2.4.3 Matrix material

Currently, three processes for producing raw composite material are documented in the literature. melt compounding, in situ polymerization, and Solution casting (Carneiro et al., 2015; Oksman et al., 2006). Polyester, epoxy, and acrylate mix with a high surface value in terms of roughness as well as a good connection to glass fiber material are also often applied as matrix materials. The spectrum of polymers used in additive manufacturing (AM) is typically limited. It involves the use of polycarbonate (PC), polyamide (PA), acrylonitrile butadiene styrene (ABS) tetraethyl orthosilicate (TEOS), and polylactide (PLA)(Dudek, 2013; Ning et al., 2017; Shofner et al., 2003). In AM, high-performance polymers are uncommon as a matrix material, employing polyetherimide (PEI) from the polyetheretherketone (PEEK) family (Chuang et al., 2015). The high melting point temperature of over 200 ℃ is a great benefit. A model was created using polymethyl methacrylate (PMMA) powder, which was then melted around the fibers (Glasschroeder et al., 2015).

Polypropylene (PP) was explored in depth by researchers (Shubhra et al., 2013) as a matrix material, with the primary benefits of PP being a high heat-distribution temperature, dimensional stability, flame resistance, and appropriateness for blending, filling, and reinforcing.

PLA was employed as a matrix material for whiskers made of microcrystalline cellulose (Bondeson & Oksman, 2007; Oksman et al., 2006). Although PLA is frequently utilized in additive manufacturing, particularly infiltrated layer manufacturing (FLM), there are few published applications of this material with significant qualities.

2.5. Filament manufacturing process

The filament is the primary material utilized in the FDM process. In general, the filament is constructed of a low-melting-point pure polymer. In some applications, the pure polymer's strength should be increased. As a result, several industries and researchers have been manufacturing polymer composites as 3D printing filament material by mixing the matrix and improving the components to build systems with structural characteristics and functional benefits that are impossible to obtain with just any component(X. Wang et al., 2017). However, because each reinforcement in a composite polymer will lead to different properties, the process of creating composite filaments must first be given special attention.(Nancharaiah et al., 2010; Shabdin et al., 2019).

2.5.1 Manufacturing filament for 3D printing using hot-melt extrusion

After raw materials are converted into polymers and pellets, continuous filaments are created for Fused Deposition Modeling (FDM). Figure 2.8 a illustrates the overall material manufacturing process for PLA filaments. The initial steps involve corn fermentation (corn to lactic acid), condensation (lactide), and polymerization to produce polylactic acid (PLA). The PLA material is then compressed and extruded into filaments for further use Figure 2.8 b represents the filament production process, which consists of three stages: hot-melt extrusion, cooling, and winding. Researchers described hot-melt extrusion as a technology for producing polymer filaments that have a strong capacity to homogeneously administer two or more solid components. (Tan et al., 2018). Heat and pressure are applied to melt or soften materials, enabling the production of uniform products with consistent shapes and densities using a die. During the extrusion process, the materials are melted by a heater and mixed by a rotating screw, which then transports the softened materials up the barrel to the screw's end. This extrusion stage is crucial, as it allows for

the modification of particle orientation while extruding plastic composite filaments, thereby ensuring optimal material properties and performance (Spinelli et al., 2019).

After extrusion, the filaments are passed through a series of hot and cold baths to achieve the standard diameters of 1.75 mm or 2.85 mm, which are commonly used in FDM filaments. Figure 2.8 c illustrates the process of winding the filaments into bundles using a roller, compensator, and coiler.

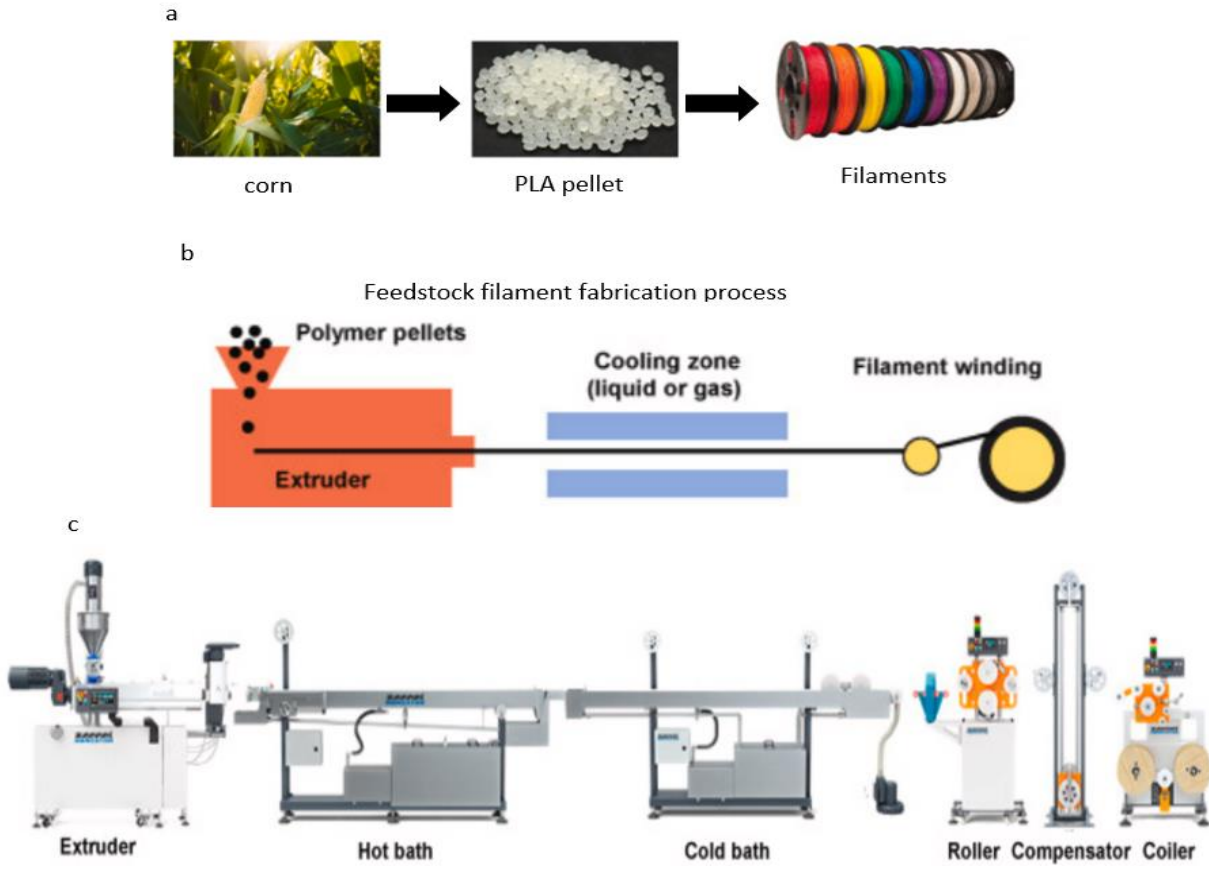

Fig. 2.8. The process for fabricating a filament. (a) The material processing for the polylactic acid (PLA) filaments. The process begins with corn fermentation, condensation, and polymerization, and the material is pelletized and extruded into filaments. (b) An overall process in the fabrication of a filament. (c) A figure of the filament production line for FDM, including extruder, hot bath, cold bath, roller, compensator, and coiler (Park & Fu, 2021).

In the following sections, the existing materials used as filaments are analyzed and summarized. Figure 2.9 provides a breakdown of the various categories of filament materials

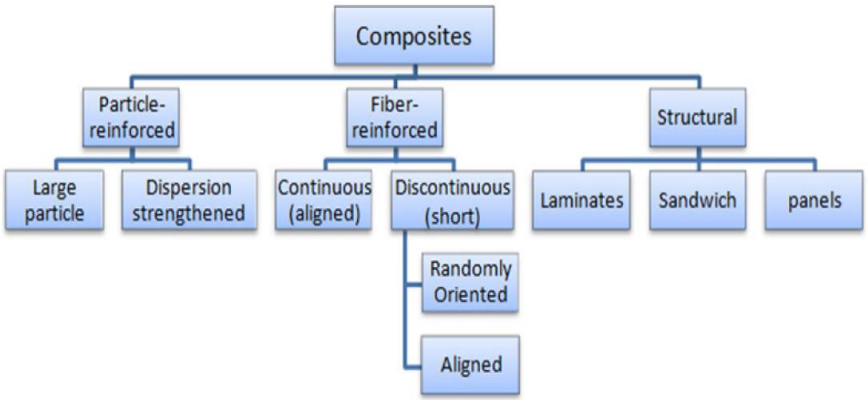

Fig. 2.9 Composite Classification Based on Reinforcing Phase (Nazeer, 2018).

2.5.2 Pure thermoplastic filaments

The process of extruding pellets or raw materials from polymers can be used to create a pure polymer filament for FDM materials. This method involves using extruders to push or exert pressure on the material through openings in the die to obtain the product in the form of an extrudate (Rauwendaal, 2014).

The barrel serves as an enclosure for the rotating screw(s) depicted in Figure 2.10. The barrel is used to heat up the raw materials as well. The barrel consists of three areas: feed zone, transition zone, and metering zone (Chaturvedi et al., 2017). The raw materials became softer in the feed zone, turned into plastic in the transition zone, and fully melted in the metering zone. The temperatures of various regions are determined according to the materials being used. The materials enter the transition zone and proceed to the metering zone via the surface of the rotating screw. The molten ingredients are pushed through a die from the metering area. The die diameter is chosen according to the needed filament sizes. Typically, a brass die with a diameter of 2.5 – 3.5 mm is employed for 1.75 mm filaments according to (Nassar et al., 2019). Once the materials are extruded through the die, they then move through a zone where they are cooled. The speed at which the filament cool has a strong impact on its quality. Various cooling methods like water baths and cold air guns are utilized for filaments. A drawing procedure can additionally decrease the diameter of the filament post cooling. Typically, an electric motor powered by direct current (DC) is utilized for the task of drawing (Nassar et al., 2019).

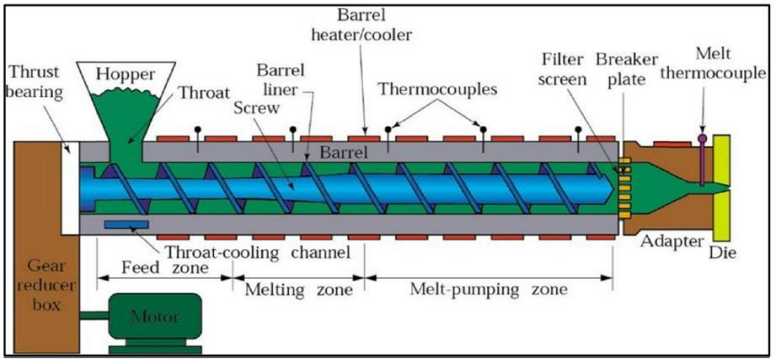

Fig.2.10 Extruder machine parts (Kasala, 2018).

The most widely known and used filament materials are acrylonitrile butadiene styrene (ABS) and polylactic acid (PLA) for the FDM process. Each has its advantages and limitations. ABS is known

to emit harmful gases during melting at high temperatures, shrinks significantly during cooling, and is not environment friendly. However, PLA is seen as biodegradable yet has low heat resistance, high brittleness, and poor mechanical properties. Therefore, these thermoplastic filaments must possess various characteristics, including chemical resistance, biocompatibility, heat resistance, flexibility, and strength, based on the specific application they are used in within a particular FDM process. The pure polymer filament is entirely made from a polymer compound without adding additive solutions (Anandkumar & Babu, 2019; Tuan Rahim et al., 2015). Each type of pure polymer filament has its inherent characteristics and mechanical properties (Van Krevelen & Te Nijenhuis, 2009). One of the steps that can be taken to improve the mechanical properties of a filament is adding additives to the filament composition. This process finally led to the composite filament (Bogoeva-Gaceva et al., 2017; Yetgin, 2020). In the following section, we will address the most popular thermoplastics (PLA, ABS, nylon, and PEEK) for the filaments in 3D printing. In addition, Table 2.5 presents a comparison of their physical and mechanical properties, as well as printing parameters.

Acrylonitrile butadiene styrene (ABS): is an amorphous substance formed by polymerizing styrene, acrylonitrile, and polybutadiene. ABS is not only stronger and harder than PLA, but it also has better resistance to corrosive chemicals, making it a more tempting alternative for FDM applications (Kuo et al., 2016). ABS typically has a melting range of 200–250 ℃. However, ABS has been used by the automotive, healthcare, and aerospace sectors to produce functional components according to (Lee et al., 2017).

Polylactic acid (PLA): PLA is another common thermoplastic known for its biodegradability but also known for its sensitivity to humidity over 60 ℃. PLA has a relatively low melting point around 145–186 ◦C and can be easily formed into filament with a temperature over 185–190 ◦C (Kim et al., 2017). Biocompatibility and good mechanical properties (relatively high strength and modulus). PLA build parts are typically used for practical applications that require a certain degree of aesthetic characteristics (Dey et al., 2020; Mazzanti et al., 2019)

Polyether ether ketone (PEEK): PEEK has an approximate glass transition temperature of 143 ℃. It is known for having high mechanical strength, lightweight, chemical and heat resistance, and biodegradability(P. Wang et al., 2019). The printing temperature of PEEK is comparatively high, around 340 ℃. Moreover, many advantages of PEEK, including excellent mechanical and chemical resistance properties, allow the application of the polymer in extreme conditions such as bone, bearing, piston parts, vehicle, and aircraft (Y. Wang et al., 2020).

Nylon 6: Nylon 6 is known for its flexibility, heat resistance, and impact resistance. It is durable and has good toughness values as well. However, as a hygroscopic material, it absorbs moisture extensively, reducing overall quality (Terekhina et al., 2019). Nylon is prone to warping like ABS. The warping effect can be reduced by maintaining the bed temperature at about 75℃.

Table 2.5. Comparison of the physical and mechanical properties, and printing conditions of PLA, ABS, Nylon, PC, and PEEK for FDM (Z. Liu et al., 2019).

Physical and mechanical properties	PLA	ABS	Nylon 6	PEEK
Glass transition temperature (℃)	53–64	102–115	47–57	137–152
Melting temperature (℃)	145–186	-	220	335–343
Heat deflection temperature (℃)	56	100	190	160
Modulus (GPa)	1.2–3.0	1.8–2.39	2.8–3.1	3.56
Tensile strength (MPa)	28–50	25–65	79	92

Printing temperature (°C)	190–220	220–250	220–270	360–450
Bed temperature (°C)	45–60	95–110	70–90	360–450
Ref.	(Mark, 2009)	(Kauffman, 2010)	(Mark, 2009)	(Mark, 2009)

2.5.3 Composite filaments

Thermoplastics become soft and fail to retain their original shape at high temperatures. In many cases, a product produced from thermoplastic filaments cannot meet specific functional requirements. The properties of FDM build parts are often inadequate when compared to the properties of injection- molded parts (Ahn et al., 2012). Based on the application fields, there is a continuous search for FDM filament materials that are lightweight, have high strength, and have good surface quality(Matthews & Rawlings, 1999). The composite materials are viewed as a viable option to meet these requirements. The need for new and environment-friendly materials are also a reason for using composite materials. Composite materials have been reported to exhibit superior properties compared to pure polymers (Kabir et al., 2020; Penumakala et al., 2020; Rahim et al., 2019).

2.5.4 Composites matrix filaments

Polymers are generally preferred for AM processes due to their adaptability to different procedures and they can be customized to complex geometries with high accuracy (Regassa et al., 2019). However, polymers have inferior mechanical properties, making them unsuitable for many load-bearing applications. Therefore, research has been undertaken to overcome the disadvantages of polymers. This reinforcement aims to increase the mechanical properties of the polymer so that it can be used in load-carrying applications. Researchers analyzed the impact of fiber orientation and layer thickness on glass-reinforced polymer composites produced using FDM. Their study concluded that FDM is suitable for producing small parts and components (Carneiro et al., 2015). One critical requirement for effective reinforcement is the desired interfacial adhesion, which enhances the affinity between fiber and resin matrix, thereby increasing the durability of glass fiber-reinforced polymers. To achieve this property, coupling agents are used to bond the fiber with polymers (Z. Liu et al., 2015).

2.5.6 Composite filaments using fibers

A fiber-reinforced composite (FRC), depicted in Figure 2.11, is composed of three primary elements: reinforcing fibers (which may be either continuous or discontinuous), a continuous matrix phase, and an interphase region, or interface, which serves as the boundary where the different materials in the composite meet and interact.

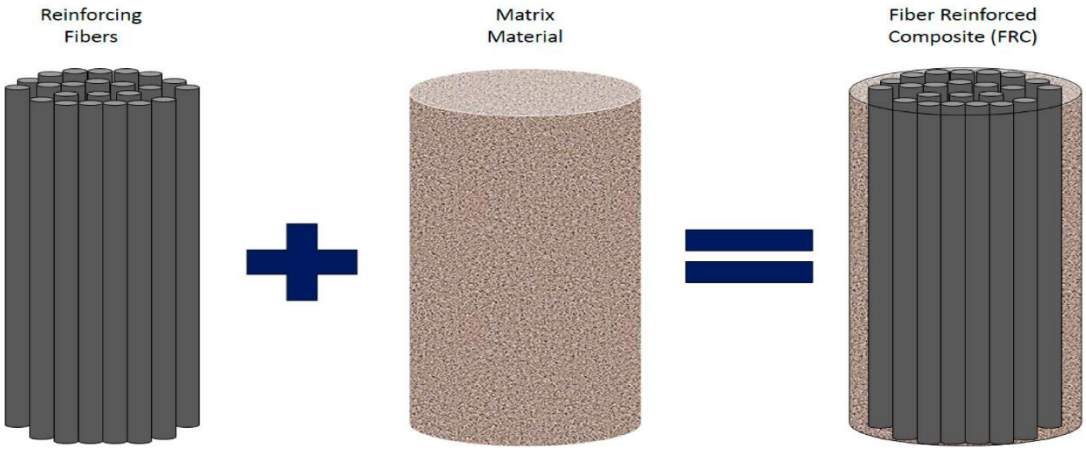

Fig 2.11 Design of a reinforced composite with reinforcing fibers (Kabir et al., 2020).

Natural or synthetic fibers are used as reinforcement materials instead of particles with polymer matrices in fiber composites which have great potential in structural industries, including aerospace, automotive, and energy applications, due to high mechanical properties with lightweight. Different fibers such as glass, rice husk, and carbon with different lengths are mixed with polymers for composite filament preparation Both discontinuous fibers (e.g., chopped glass fibers (Zhong et al., 2001b), chopped carbon fibers (Ferreira et al., 2017), and short basalt fibers (Sang et al., 2019) and continuous fibers (e.g., glass (Justo et al., 2018), carbon (Justo et al., 2018; Sugiyama et al., 2018), and aramid fibers (Dickson et al., 2017), are used as reinforcements for the composite continuous fiber-reinforced composites exhibit high performance compared to the discontinuous fiber-reinforced ones. In short fiber composite, the fibers are blended with a polymer matrix before the preparation of composite filaments. Conversely, separate spools of fibers and polymer filaments are used for printing parts from continuous fiber composites (Penumakala et al., 2020) because continuous fibers have a long aspect ratio and are typically aligned in orientation within composites. The advantages of fiber composites, combined with the flexibility of FDM, can be achieved by using fiber-reinforced composites as filaments. This subsection provides a systematic summary of research on composite filament development for the FFF process, showcasing different types and forms of reinforcement materials used as composite filament materials, as illustrated in Figure 2.12. The composite materials for FDM filaments are categorized based on reinforcement types in this section.

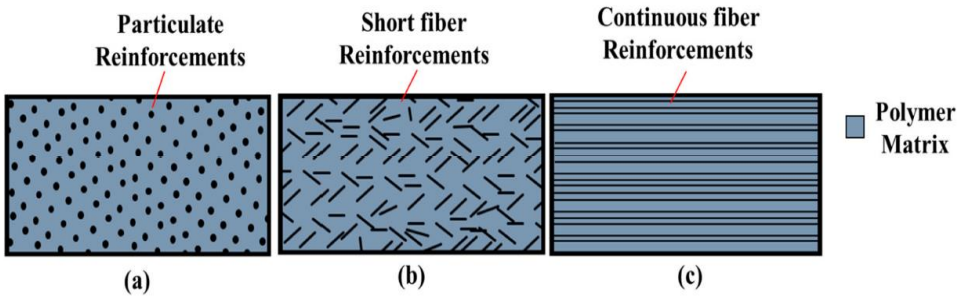

Fig. 2.12 Various reinforcement materials used in composite filaments: (a) Particulate reinforcement, (b) short fiber reinforcement, and (c) continuous fiber reinforcement composites (Bettini et al., 2017).

Discussion on continuous and discontinuous fiber: Carbon and glass fibers are commonly used for FFF process composite filaments. The process involves blending fiber composites, polymer matrix, and short fibers using an extruder to produce composite filaments. The quality of composites depends on factors such as blending temperature, blending time, fiber distribution in the matrix, surface energy, coefficient of thermal expansion, fiber orientation, proportion of fibers, adhesion between fibers and matrix, thermal stability of fiber, presence of voids, moisture absorption of fibers, fiber diameter, and fiber length (Halip et al., 2019). The essential factors affecting part properties and printability are summarized and graphically represented in Figure. 2.13.

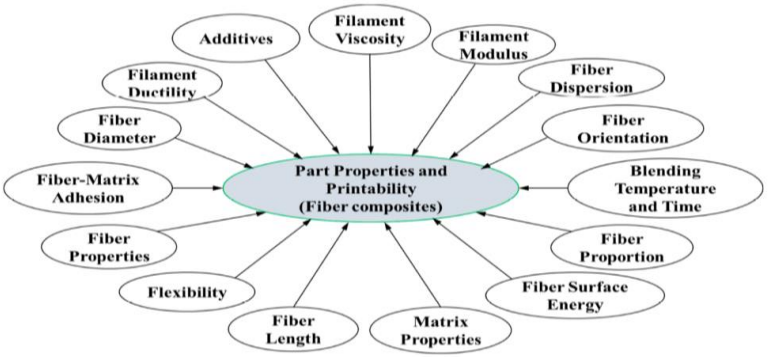

Fig. 2.13 Factors affecting part properties and printability of fiber composite filaments (Pu'ad et al., 2020).

While advanced commercial systems like the Markforged Mark Two and Onyx Pro can embed continuous fibers into the printed part, they are limited to laying those fibers in flat, two-dimensional layers (within the X-Y plane). Current FDM-based technologies are not yet capable of aligning fibers freely in all three dimensions. This means that the reinforcing fibers are deposited layer by layer, which restricts their ability to strengthen the part in all directions. For applications that demand strong performance from multiple angles, this directional limitation is a critical factor to consider when evaluating the mechanical properties of the final printed structure.

2.6 Methods of printing polymer composites using FDM technology

Based on a review of the literature (Der Klift et al., 2016; Dudek, 2013; Ning et al., 2015; Tekinalp et al., 2014). It is proposed that methods for printing composite materials or multifunctional structures be classified according to the type of extruder (printing head), as shown in Figure 2.14.

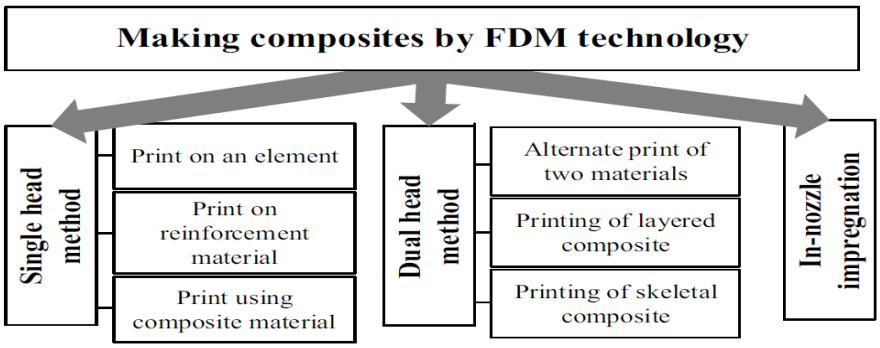

Fig 2.14. Composite manufacturing by FDM technology (Bryll et al., 2018).

2.6.1 Creating multi-material structures by printing on an element

An interesting method of creating multi-material structures involves printing a layer of polymer material on the surface of a ceramic, metal, wood, or another polymer material. The resulting structural elements can be made of multiple materials, with the built-in element occupying most of the entire volume (Bak, 2003; Dudek, 2013). However, a major limitation of this method is the necessity to divide the model into parts separated by parallel planes to identify subsequent printing stages. Additionally, the printing head must be controlled and stopped to place additional elements. A technological challenge in this method is to resume printing without breaking the continuity of the material (Dudek, 2013).

2.6.2. Creating a composite structure by single nozzle

Manufacturing a composite structure using a single head by printing on the reinforcement material is considered a method similar to creating multi-material structures. Composite materials are obtained in a multi-stage process (see figure. 2.15), where the number of stages depends on the number of reinforcement layers in a finished element. Each printing stage is designed by specifying a division plate, which enables stopping the printing and depositing the reinforcement phase on the print. Layered composites made by this method can be reinforced with continuous fiber, cloth, or mat. Disadvantages of this type of printing include restrictions associated with the process and with the thickness of individual layers of the reinforcement material in the composite. The layer of reinforcement commonly found in the literature is approximately 0.5 mm thick (Dudek, 2013; Guo & Leu, 2013; Kumar & Kruth, 2010).

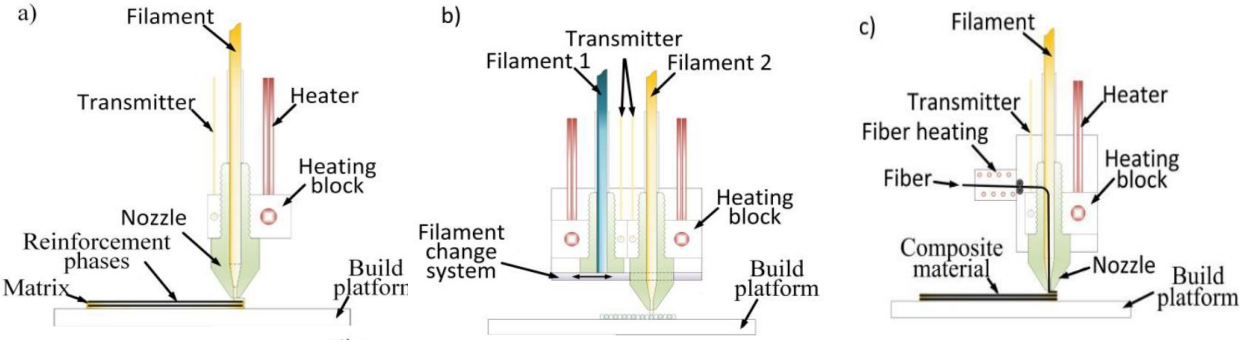

Fig. 2.15. Manufacturing and composite structure by a) single head printing on a reinforcement material. b) dual materials printing. c) in-nozzle impregnation (Goryl et al., 2024).

Producing composite structures using a single nozzle involves utilizing specialized filaments distinct from those used in conventional 3D printing. These filaments are infused with various additives such as rubber microspheres, glass or carbon fibers, or wood flour in addition to the base polymer. Achieving the correct filament diameter (typically 1.75 mm or 3 mm) requires precise control of the extrusion speed, as increasing speed results in a smaller diameter. There are also constraints regarding the size and volume fraction of reinforcement particles within the filament. If the particles are too large or present in excessive quantities, they can obstruct the printer nozzle, leading to compromised print quality and potential blockages (Bak, 2003; Chybowski & Gawdzińska, 2016; Kumar & Kruth, 2010; Tekinalp et al., 2014).

Figure 2.16 depicts the fabrication of a composite structure using an advanced dual-material printing technique. This process, which alternates between two distinct materials, has become increasingly prevalent in modern 3D printing. It can be executed using either a dual-nozzle setup or a single nozzle equipped with a filament-switching mechanism. By using this method, designers can create intricate composite structures tailored to specific requirements (as illustrated in Figure 2.16 a-b). However, dual-material printing poses several challenges. One of the primary issues is contamination during filament transitions, as it is difficult to achieve a seamless switch between materials. To address these limitations, continuous advancements in filament-switching systems and software updates from printer manufacturers are being implemented to improve process reliability and overall print quality (Bryll et al., 2018).

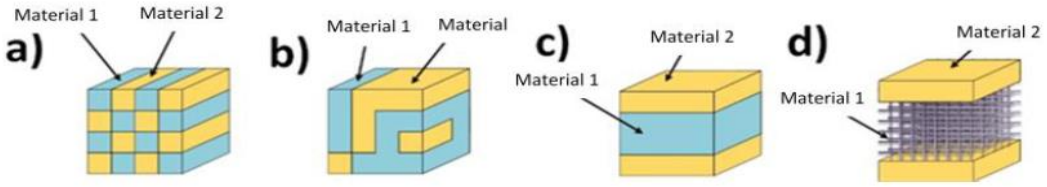

Fig. 2.16. Example print structures of dual materials composite a-b) varied distribution of materials c) sandwich structured composite - layered, d) sandwich structured composite - skeletal.

2.6.4 Creating a layered composite structure using a special nozzle.

In Figure. 2.15c, a schematic representation illustrates the process of creating continuous composites through in-nozzle impregnation. In this method, the filament acts as the matrix material while continuous reinforcing fibers are fed separately into the printer nozzle. The reinforcing phase is preheated before being inserted into the nozzle to enhance the impregnation of fibers with the thermoplastic material. The fibers are automatically supplied to the printer head through filament motion. Inside the printer head, the filament is plasticized and merged with the reinforcing phase. Subsequent stages of the printing process resemble traditional 3D printing (Bryll et al. 2018).

2.7. Summary of literature review

This literature review comprehensively reviews three broad topics: additive manufacturing technologies, classifications of polymer materials, and composite filament. It systematically analyzes seven primary categories of 3D printing methods. These methods are applied to a variety of materials. A significant focus is placed on fiber-reinforced polymers (FRPs) within Fused Deposition Modeling (FDM) technology, highlighting common fiber and matrix materials suitable for this process. In addition, the review thoroughly analyzes manufactured filaments for 3D printing, discussing various filament types including pure thermoplastics, composites, and specialized structures, and their respective properties. Key research areas identified include fiber alignment, material development, and the enhancement of fiber-matrix interfaces, aimed at addressing challenges such as void formation and layer visibility.

Ongoing studies aim to optimize FDM processes to improve the performance of FRPs in additive manufacturing. The review compares different filament types, including pure thermoplastics. It also explores the emergence of composite filaments, which integrate polymers with fibers or other reinforcements to achieve enhanced properties, thereby addressing the shortcomings of pure thermoplastics. Additionally, the use of biomaterials in filament production

is discussed as a means to develop eco-friendly alternatives for applications such as custom implants. Additionally, this review provides a comprehensive overview of filament manufacturing techniques and materials, focusing on the dynamic landscape of additive manufacturing and the pressing need for innovative composite solutions. The methods explored underscore the complexity and potential of FDM technology in creating advanced composite structures, while also addressing the inherent capabilities and limitations of current practices. Finally, recent investigations into the printing of composite polymers using FDM are briefly reviewed, highlighting existing knowledge gaps in the field.

In conclusion, the existing literature provides valuable insights into the mechanical properties of 3D-printed materials and the influence of various factors, such as reinforcement techniques and filament types. However, few studies have focused on comparing different tensile standard geometries printed with various orientations. Additionally, while previous research has often focused on tensile properties, there has been limited attention on comparing compression, bending and tensile properties across different printed materials. Moreover, the study of different sandwich structures such as honeycomb and rhombus cores has primarily examined individual properties like compression, bending, or tensile strength, without comprehensive evaluation of all key mechanical properties like bending. Furthermore, no studies have compared the influence of different skin layers on sandwich structures featuring re-entrant honeycomb cores or explored varying compression test orientations.

Another gap in the literature is the lack of research on recycled filaments reinforced with natural fibers, specifically investigating their tensile filament properties. There is also a notable absence of studies on multi-layer structures with varying thicknesses, particularly involving materials like PLA, PETG, and carbon-fiber-reinforced PETG and PLA.

This study seeks to bridge existing knowledge gaps by providing a comprehensive understanding of the mechanical performance of 3D-printed materials under varying conditions. Such insights are expected to pave the way for expanded applications of plastics. Consequently, exploring the mechanical properties of these materials represents a promising and challenging frontier in the fields of science and technology.

3. MATERIALS AND METHODS

This chapter outlines the materials, equipment, techniques, and processes used in the current study. It also describes the scientific methodologies used in the experimental measurements, as well as the test systems used to achieve the study's aims.

3.1. Design of experiment

In this research, FDM 3D printing technology was utilized to produce samples using thermoplastics in filament form. Two types of materials, neat (pure) polymers and composite polymers, were examined. Each material was employed to fabricate specimens with varying print parameters for different tests. These specimens underwent extensive mechanical testing and simulation, focusing on tensile, compressive, bending, and sandwich structure characteristics. The procedure and sequence of experiments conducted in this study are presented in the flowchart in Fig. 3.1. The experimental work was primarily carried out at the Szent István Campus, MATE University, Hungary, in the additive manufacturing and material science laboratories. The following sections detail the procedures for material preparation, 3D printing of specimens, multi-material printing, and the various tests conducted for each material and method.

Fig. 3.1. Flowchart for the steps of the experiments

3.2. The 3D printing technology

The test specimens were manufactured using fused deposition modeling (FDM) 3D printers, specifically the Geetech A20M, Wanhao Duplicator 6, and Bambu S1 models. Process parameter variations were managed through the slicing software Cura Ultimaker, Wanhao Duplicator 6, and Bambu Studio, as shown in Fig. 3.2 a, b, and c. respectively. Sample designs were created using SolidWorks software, exported as STL files, and subjected to various process parameter modifications via the slicing software.

Fig. 3.2. The 3D printers employed, a) Geetech A20M, b) Wanhao Duplicator 6, C) Bambu S1

3.3. Manufacturing of 3D-printed specimens

As mentioned in section 3.1., two types of polymer materials were examined, neat and composite, for each 3D printing method. The following sections describe the details of producing the 3D-printed specimens for each material and technique used.

3.3.1 Different tensile geometry shapes

The specimens were manufactured using polyethylene terephthalate glycol (PETG) filament, The filament is black and has a diameter of 1.75 mm. The CAD design, created by the CAD program "Solidworks 2021" and exported as an STL file, underwent changes in process parameters. Table 3.1 contains the standards utilized for manufacturing the targeted specimens, along with the dimensions and other specifications of each specimen's type. The modifications were applied using the slicing software Ultimaker Cura 5.2.1. A printer nozzle diameter of 0.4 mm was used. The printing temperature and build platform temperature during the process were maintained at 230 °C and 70 °C, respectively. The print speed, fill percentage, and number of perimeters were set as 60 mm/s, 100%, and 2 outlines, consecutively. In this research, the focus was on investigating the impact of build orientation as the primary manufacturing process parameter, while other parameters were kept constant to isolate its influence on mechanical performance. Table 3.1 contains the standards utilized for manufacturing the targeted specimens, along with the dimensions and other specifications of each specimen's type. The tab level angles mentioned in the table refer to the tapered termination angles of the end tabs used for the specimens. End tabbing is a technique commonly employed in composite testing to alleviate stress concentrations at the grip edges and promote failures within the gauge section. It involves attaching end tabs to the specimens to distribute the clamping force and protect the specimen surface (Czél

et al., 2016). In addition, Figure 3.3 illustrates all specimen designs created by using SolidWorks software.

Table 3.1. Standard and specifications of each specimen type manufactured.

Standard	Width of narrow section [mm]	Width overall [mm]	Length overall [mm]	Thickness of narrow section [mm]	Thickness overall [mm]	Radius of curvature [mm]	Tab bevel angle [°]
ASTM D638	13	19	165	3	3	R76	-
ISO 527-2	10	20	150	3	3	R60	-
ASTM 3039/3039M	20	20	165	3	3	-	0°
ASTM 3039 angle	20	20	175	2	5	-	15°
ASTM 3039 angle	20	20	175	2	5	-	90°

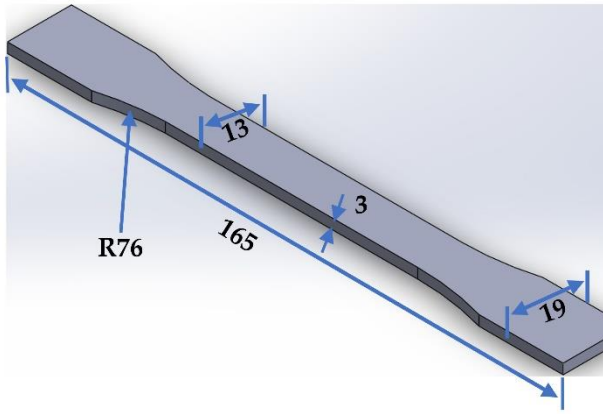

(a)

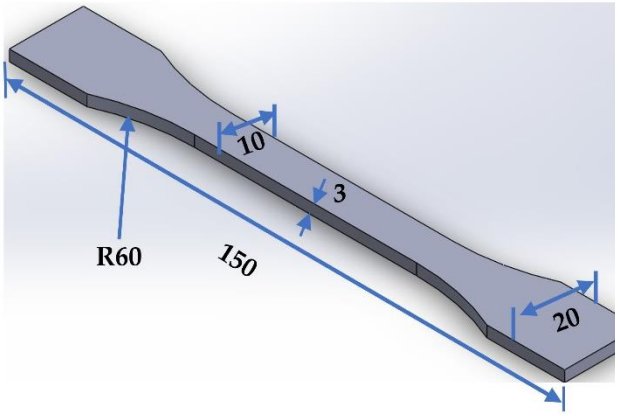

(b)

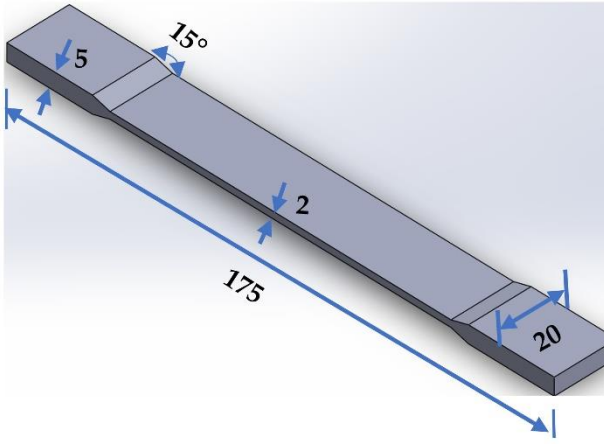

(c)

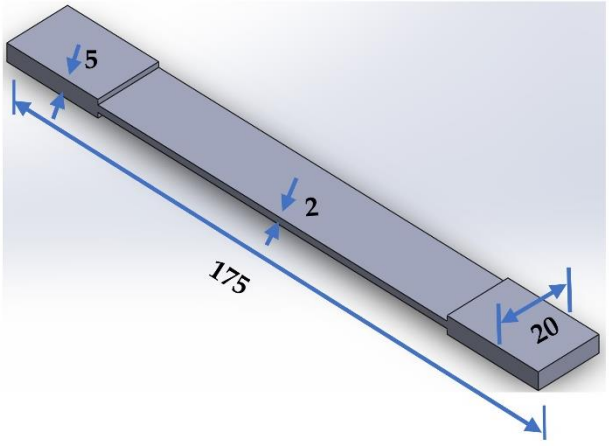

(d)

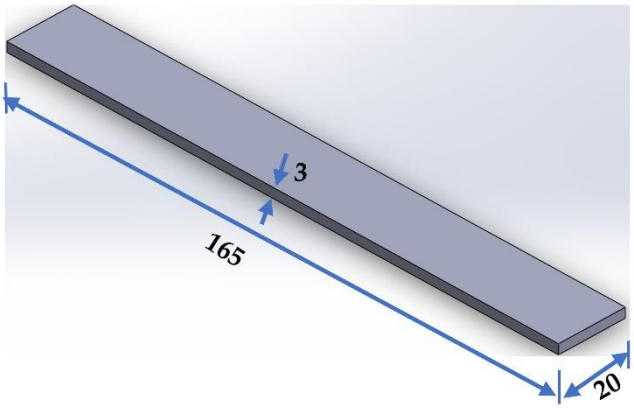

(e)

Fig 3.3. Different geometry shapes of tensile test specimens drawn by SolidWorks software according to the standard (a) ASTM D638, (b) ISO 527-2, (c) ASTM D3039-15°, (d) ASTM D3039-90°, and (e) ASTM D3039-0°.

All these tensile standard-shapes specimens created were printed in two build orientations (flat and on edge) to determine the effect of print orientation on the mechanical properties as well. Figure 3.4 illustrates the specimen design orientations used for the production of the tensile testing samples.

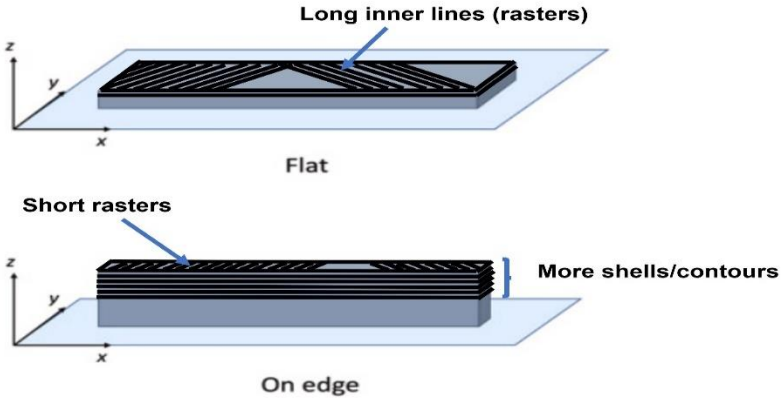

Fig 3.4. Build orientations examined (flat and on-edge).

- **The finite element method for different geometries**

A series of numerical simulations were performed using the finite element method (FEM) to have a more detailed vision of the effect of specimens' geometries on the mechanical properties. The commercial software ANSYS 17.2 was used in these simulations with a research licence.

- Modeling

Numerical simulation is an approximation method, where the governing equations are being integrated on every element forming the so-called numerical model. For structural analysis, the so-called weak form was being recovered and applied according to equation 1.

$$\int_{\Omega} \sigma_{ij} \delta u_{ij} dV = \int_{\partial\Omega} \hat{t}_j \delta u_i dA \tag{3.1}$$

This equation is applied to every finite element (Ω) with its closure (∂) as the boundary, and the underlying continuum body's shape. The material parameters, such as Young's modulus, Poisson's

ratio, and density, were determined based on the physical and mechanical properties of the materials used in this research. These values were obtained from a combination of manufacturer datasheets and experimental tensile tests conducted during the study. Both linear and nonlinear elastic models were employed in the simulations to better approximate the behavior of the printed materials under different loading conditions. The material was treated as an isotropic material with constant properties in all directions. The isoperimetric Galerkin method (Zienkiewicz & Taylor, 2005) selects the test function (δu_i) from the same Hilbertian Sobolev space as the displacement field (u_i). The system was simplified, and the linear strain measure was utilized because the deformation on a tensile test is minimal. The strain and stress could be calculated using equations (3.2) and (3.3), respectively.

$$\varepsilon_{ij} = \frac{1}{2}\left(u_{ij} + u_{ji}\right) \tag{3.2}$$

Hooke's law can be applied because of the observed elasticity without rate effects,

$$\sigma_{ij} = C_{ijkl}\varepsilon_{kl} \tag{3.3}$$

where the stiffness tensor of rank four (C_{ijkl}), the stress tensor (σ_{ij}), and the strain tensor (ε_{ij}), are linearly connected.

Geometry model, meshing, and boundary condition in numerical simulations, the quality of the mesh is essential for achieving accurate and meaningful results. These simulations allowed us to study the tensile response of the specimen structures and identify areas prone to stress concentration. The software incorporated detailed specimen dimensions and material properties, including the tensile characteristics of the solid samples. Key parameters like Young's modulus and yield strength were integrated, with both linear and nonlinear elastic material models employed. Material constants used in the simulations included an elastic modulus of 5220 MPa, a Poisson's ratio of 0.33, and a density of 1270 kg/m^3. In order to benefit the geometrical symmetry and reduce the computational cost, every specimen's geometrical model was clipped using its symmetry planes, resulting in only one eighth of the original geometry and half of the gripping mechanism from the experimental apparatus. Furthermore, A uniform element size was applied throughout, except in regions with significant changes in cross-sectional areas.

It is important to note that the material behavior of FDM-printed components presents unique challenges in FEM modeling. Due to the anisotropic and heterogeneous nature of FDM structures, particularly the planar, closed-loop inhomogeneities caused by the path of the print head, conventional isotropic or even basic anisotropic elastic models may not fully capture the complexity of the printed material's internal architecture. While an anisotropic elastic material model was used in this study to approximate these effects, it is recognized that such models provide only a limited representation of the true mechanical behavior. These limitations should be considered when interpreting simulation results, and further research is needed to develop more accurate material models for 3D-printed polymers.

The machine zone was divided into three sections, each 1 mm in width. Similarly, the specimens were segmented into three zones, with the critical zone at 0.2 mm and the remaining zones at 0.5 mm, as shown in Figure 3.5.

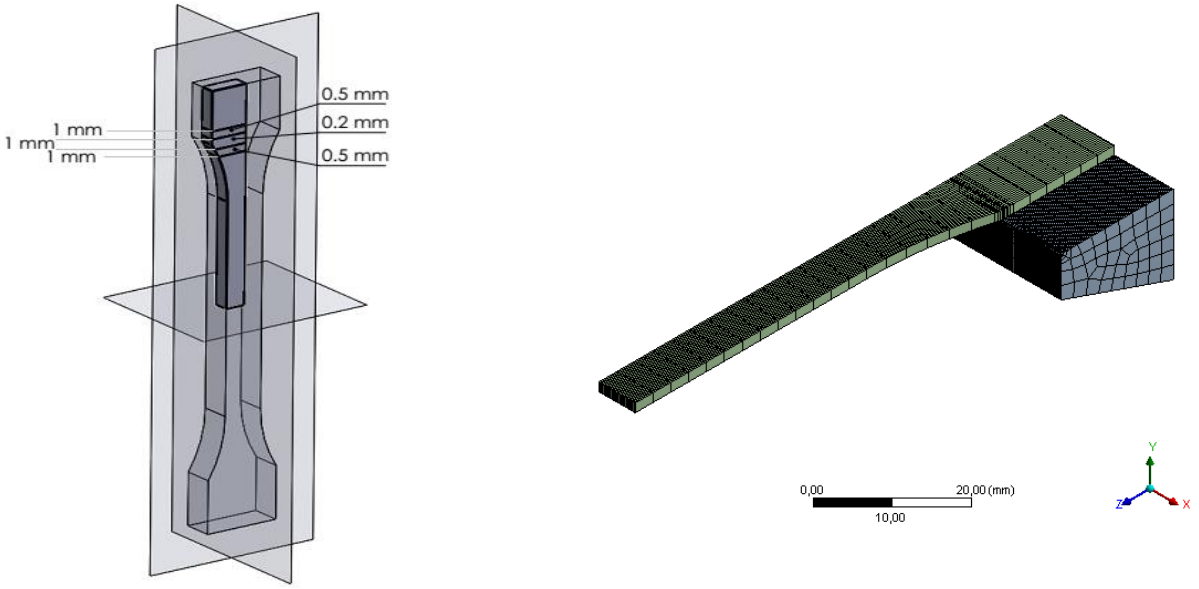

(**a**) (**b**)

Fig 3.5. Symmetry planes and mesh sizing.

As for the boundary conditions, to emphasize the true geometrical effect and to exclude the effect of different (Force vs. Elongation) curves, a uniform stress of 70 MPa was applied to every numerical study with a frictional contact between the specimen and the gripping jaw alongside with a zero displacement of the gripping jaw as shown in Figure 3.6.

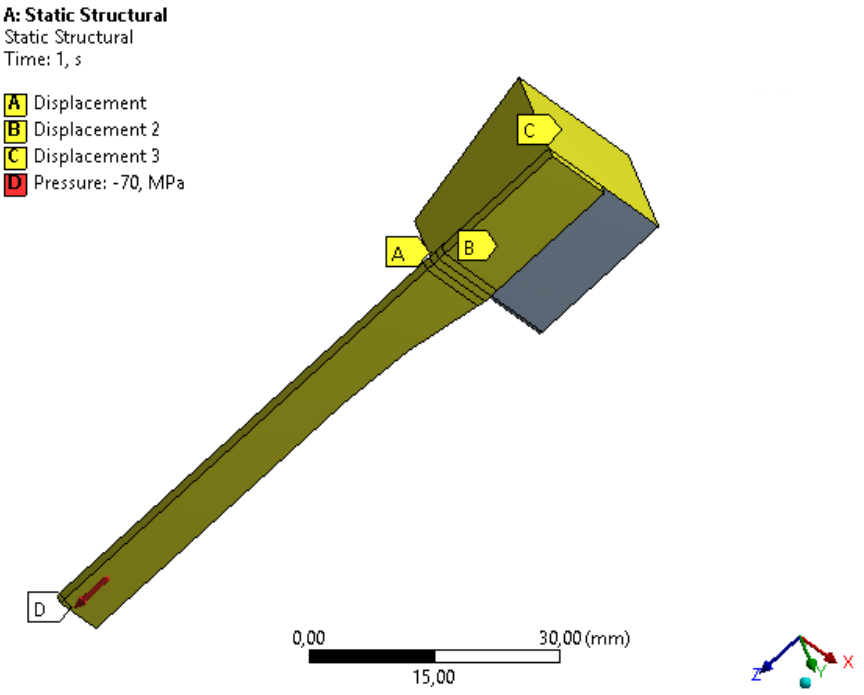

Fig 3.6. Boundary conditions employed in the simulation.

3.3.2 3D-printed carbon fiber-reinforced polymer composites and pure polymers

The experimental materials encompassed CFPLA, CFPETG, PETG, and recycled PLA (rPLA) filaments with a diameter of 1.75 mm, sourced from reputable suppliers. The PETG and rPLA filaments were acquired from 3Djak (*Extrudr PETG Black - 3DJake Belgium*, n.d.; *ReForm - rPLA Black 1,75 mm*, n.d.), while CFPLA and CFPETG filaments were obtained from Spectrum(*Carbon PLA 1,75 Mm / 1000 g*, n.d.; *Carbon PLA 1,75 Mm / 1000 g*, n.d.). These filaments were reinforced with 10 wt.% carbon fibers, each having a fiber length of 100 μm. The inclusion of carbon fibers significantly augmented stiffness, hardness, and tensile strength, all while maintaining low shrinkage and excellent adhesion. Furthermore, the 10%carbon fiber addition provided the models with a matte finish. Printing of the test pieces took place using a 0.4 mm nozzle diameter on the Geetech A20M printer situated in the additive manufacturing laboratory at Szent Istvan Campus, MATE University, Hungary. Tabulated in Table 3.2 presents the specific printing parameters for each material.

Table 3.2 Printing parameters employed for each material

Printing parameters	Material			
	PETG	CFPETG	rPLA	CFPLA
Layer thickness	0.2 mm	0.2 mm	0.2 mm	0.2 mm
Initial layer height	0.24 mm	0.24 mm	0.24 mm	0.24 mm
Print speed	60 mm/s	60 mm/s	60 mm/s	60 mm/s
Infill density	100%	100%	100%	100%
Platform temperature	70 ℃	75℃	60 ℃	45 ℃
Printing temperature	230 ℃	240 ℃	210 ℃	200 ℃
Nozzle diameter	0.4 mm	0.4 mm	0.4 mm	0.4 mm

Tensile test specimens, conforming to the ASTM D3039 rectangular shape (165 mm × 20 mm × 3 mm), were 3D-printed. For each material, samples were produced in two orientations: flat and on-edge. A total of 24 tensile test samples were printed (three from each orientation, utilizing identical print settings). Compressive test samples, adhering to ASTM D695, were created with a diameter of 13 mm and a length of 20 mm. The total count of compressive test samples reached 12. The design of these specimens was executed using SolidWorks software. Figure 3.7 depicts the designed compressive and tensile specimens with distinct building orientations.

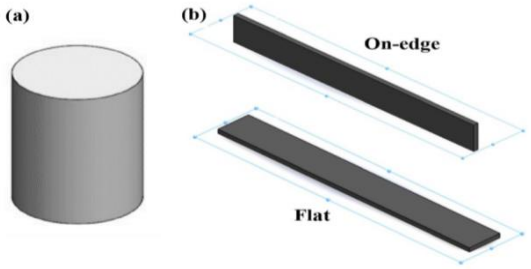

Fig. 3.7 Samples design by SolidWorks software (a) the compressive sample, (b) tensile specimens built with two different orientations; on-edge and flat.

Figure 3.8. shows the group of samples before the tensile and compressive tests.

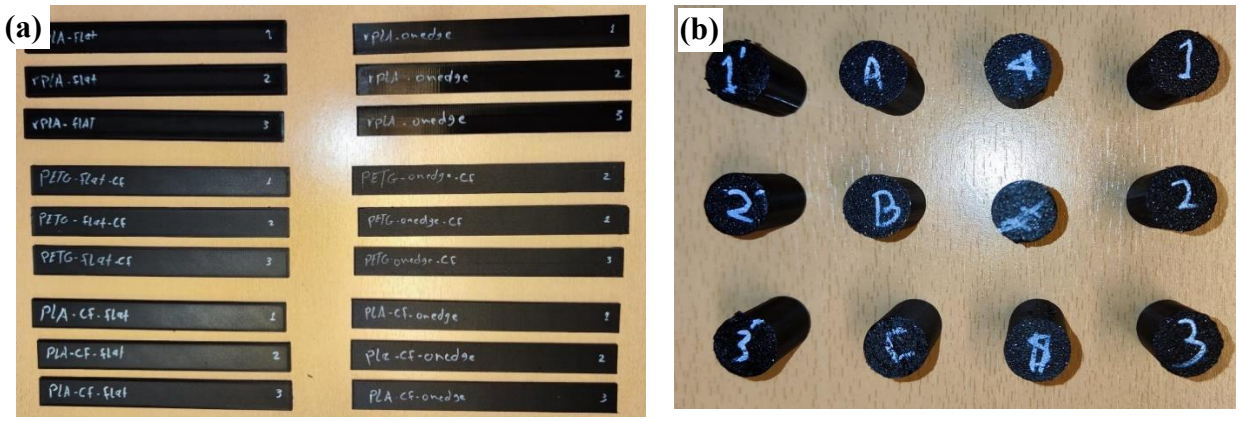

Fig. 3.8. Samples before testing: (a) tensile specimens, (b) compressive specimens

The fracture interfaces of the specimens were examined post-mechanical testing utilizing the Axio Lab A1 Microscope, situated in the additive manufacturing laboratory at Szent Istvan Campus, MATE University, Hungary. The imaging software, operating at 50x magnification, was employed to capture and process data, facilitating the analysis of interfaces between deposited lines and the isolation of fractured fibers within the matrix subsequent to the tensile test. A single specimen, selected from the three tested samples, was scrutinized to study the fracture interface in detail.

3.3.4 Re-manufactured filaments

- Material Specifications

` Recycled polylactic acid (rPLA) (*ReForm - rPLA Black 1,75 mm*, n.d.)and polyethylene terephthalate glycol-modified (PETG) filaments, along with carbon fiber-reinforced PETG (CF-PETG) and carbon fiber-reinforced PLA (CF-PLA), were utilized for filament tensile testing.

This study also incorporated re-manufactured filaments of PLA, rPLA, and PETG. To enhance the mechanical properties of the re-manufactured PLA and rPLA filaments, hemp fiber was used as reinforcement. Similarly, jute fiber was employed for the re-manufactured PETG filaments (see Figure 3.9 a, and 3.9 b). Comprehensive tensile property testing was subsequently conducted on these filaments. Table 3.3 presents detailed information about filament manufacturers and the mechanical properties of the original filaments used in the printed specimens, as reported by the manufacturers. Additionally, the properties of the reinforcement fibers, as extracted from the material data sheets, are listed in Table 3.4.

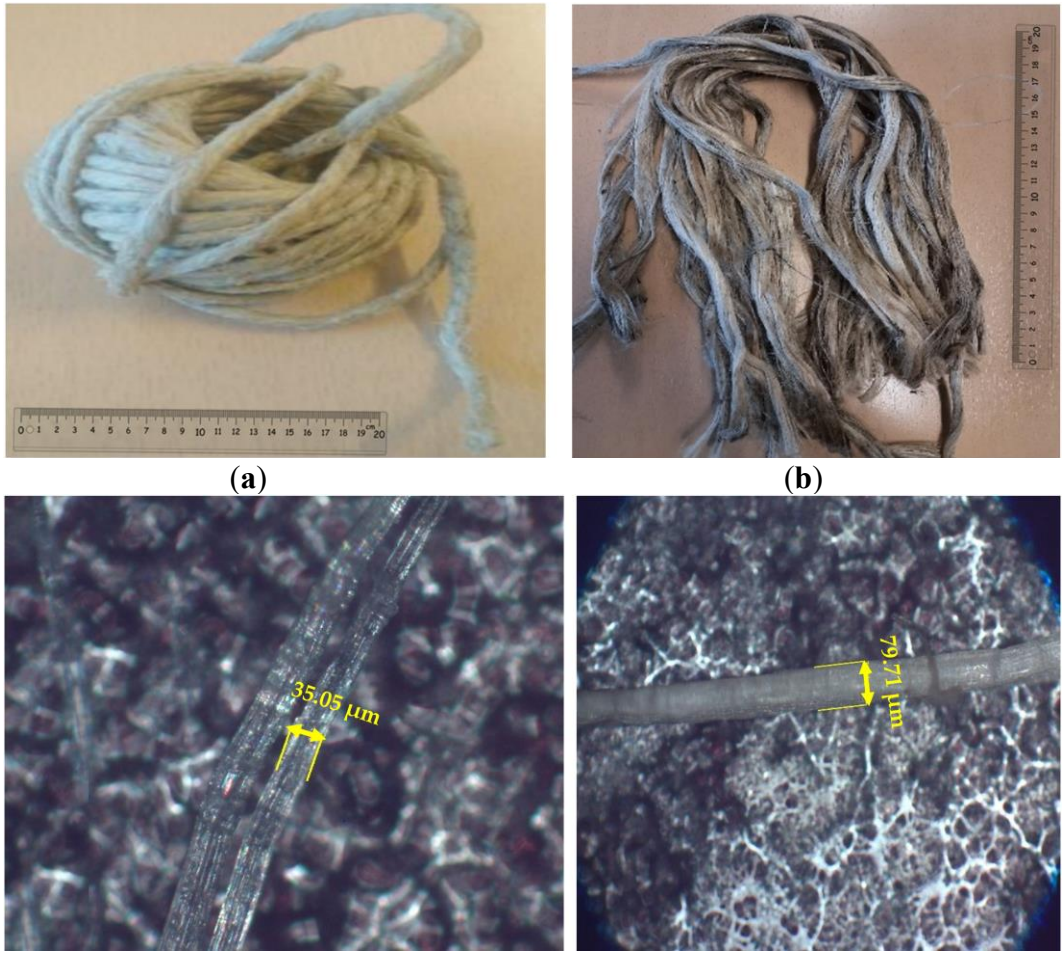

Fig 3.9. Fibers used in the study along with their microstructure: Hemp fibers shown in (a) and (c), and Jute fibers in (b) and (d).

Table 3.3. Mechanical characteristics and manufacturers of the materials utilized.

Properties	**Materials**				
	PLA	**rPLA**	**PETG**	**CF-PLA**	**CF-PETG**
Density [g/cm^3]	1.25	1.24	1.29	1.3	1.32
Tensile strength [MPa]	51	63	61	65	45
Elastic Modulus [MPa]	2400	3251	3100	12500	4250
Elongation at break [%]	3.5	4	4	0.5	4.9
Manufacturer	Creality	3D JAKE	Extruder	Spectrum	Spectrum

Table 3.4. Mechanical and physical properties of jute and hemp fiber [35].

Fibers	**Length [mm]**	**Density [g/cm^3]**	**Tensile strength [MPa]**	**Young's Modulus [GPa]**
Jute	2-120	1.5	393-773	10-30
Hemp	5-55	1.4	550-1110	30-70

To ensure the resulting filament meets specific quality, performance, and application-related criteria, it is essential to determine the dimensions of small hemp pieces and the diameter of jute fibers before transforming them into filament form. Under 10×10 magnification, the microscope provided detailed measurements: the hemp fiber diameter was 35.05 µm, the width was 23.78 µm, and the jute fiber diameter measured 79.71 µm (see Figure 3.10 c and 3.10 d). Figure 3.10. presents a schematic roadmap that clarifies the distinction between the materials used, specifying which were purchased, which were employed in multi-material designs, and which were recycled, along with the tests performed on each group.

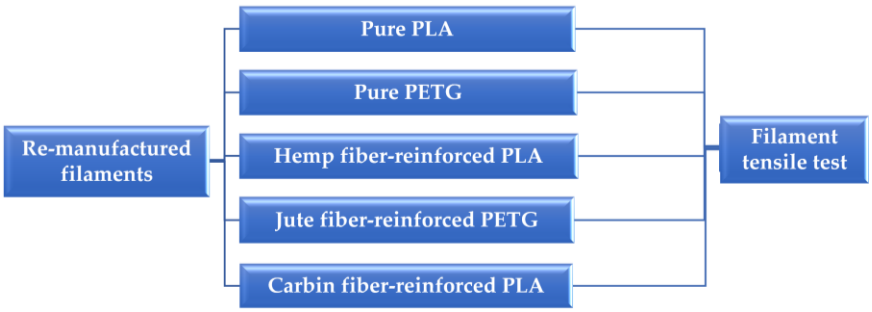

Fig.3.10. Schematic roadmap illustrating the categorization of materials used in the study: re-manufactured materials.

- Filament fabrication

The objective was to create new filaments by re-manufacturing the original commercially-produced filaments to evaluate their ultimate tensile strength (UTS) and compare these results with those of the initial filaments. The preparation process began with chopping the original filament into small particles utilizing a filament cutting machine. These particles were then fed into a single-screw extruder to produce new filaments.

In the Materials Science laboratory, a filament-cutting machine was utilized. A segment of the commercially-produced filament was sliced into pieces and placed into the machine's chamber. After securing the chamber to the apparatus, it was operated for seven seconds to generate the final particles (see Figure 3.11). The cutting process generally produced particles in the 3–5 mm range, Fiber content was calculated using weight percent (wt.%), based on the formula:

$$Fiber\ wt.\% = \left(\frac{Weight\ of\ Fiber}{Weight\ of\ Fiber + Weight\ of\ PLA}\right) \times 100$$

This approach ensured that natural fiber reinforcement remained consistent at 7 wt.% across the samples.

Five materials PLA, rPLA, CF-PLA, PETG, and CF-PETG, were cut separately and prepared for manufacturing new filaments. The filament was created using a filament maker machine after being ground with the WŻ-1 grinder machine. PLA and PETG particles were fed into the machine's barrel and heated to specific temperatures. The extrusion temperatures were set to 185 °C and 200 °C for PLA and PETG polymers, respectively. The extrusion speed was set to the maximum level on the machine to ensure material melting. Inside the barrel, the rotating screw advanced the molten material, simultaneously mixing and blending it to maintain uniform quality. After the material was fully melted and homogenized, it was extruded through a die to produce

filaments with a specified diameter of 1.75 mm. The filament was then cooled with a fan and readied for subsequent testing.

The same process was repeated while mixing hemp fiber with PLA and rPLA filaments and jute fiber with PETG filaments. The selection of hemp with PLA and jute with PETG was based on preliminary trials that demonstrated better interfacial bonding and mechanical performance with these specific material combinations. Additionally, extruding hemp and jute composites with 7 wt% was achieved without difficulty. The percentages of fibers were chosen based on prior research (Gupta et al., 2019) and practical considerations of printability and mechanical properties. However, attempts to re-manufacture CF-PETG were unsuccessful. According to previous research (J. Zhang et al., 2020), recycling carbon fiber-reinforced thermoset composites has been particularly challenging, and similar difficulties may apply to carbon fiber-reinforced PETG

Due to circumstances that were difficult to control, varying filament diameters were obtained, which differed from commercially manufactured filament. These conditions included the inability of the mixing chamber in the extrusion machine to provide a homogeneous blend of the molten material, leading to inconsistent filament uniformity. Additionally, difficulties in calibrating the melting temperature and extrusion speed resulted in diameter variations and noticeable disturbances in the amount of extruded filament. Moreover, the lack of control over cooling, represented by the presence of a single-speed fan, exacerbated issues during the manufacturing process. Despite these challenges and difficulties, the required and sufficient samples were obtained for testing. Experimental adjustments were made to the temperature settings to align with the extrusion speed, and the available cooling system was adjusted to produce testable samples. The total number of the re-manufactured filament tensile test is 35.

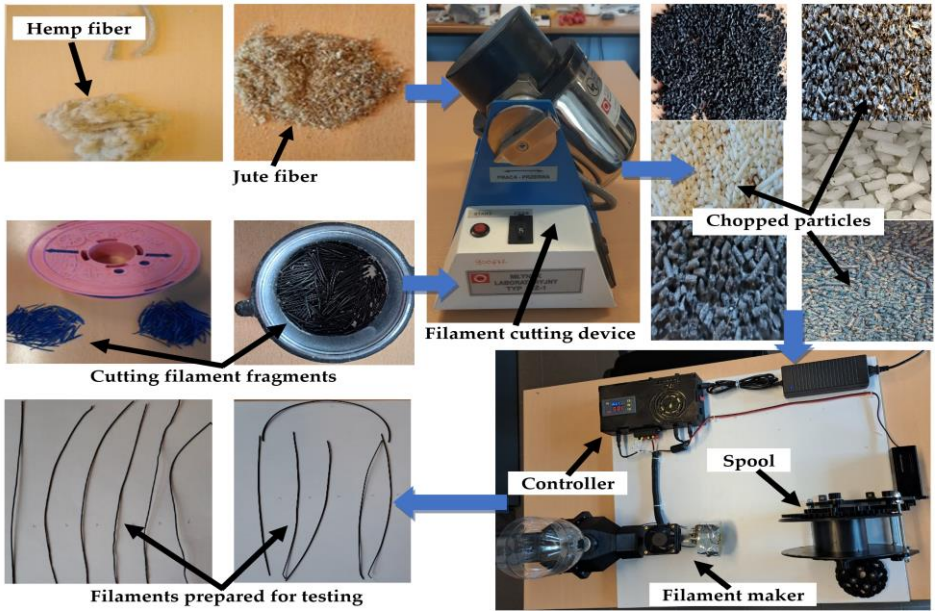

Fig. 3.11. Filament cutting procedure.

The filament diameter varied for each material. Table 3.5 shows the different diameters of the materials after they were re-manufactured and reinforced with natural fibers.

The reduced filament diameter observed was likely due to challenges in controlling the fan speed and the rapid transition from the molten to solid state during extrusion. Additionally, the speed of the extruder played a role in this deviation, impacting the cooling rate and resulting in thinner filaments than expected.

Table 3.5. Diameters of the materials after re-manufacturing and reinforcing with natural fibers.

Specimens	Re-manufactured filament Diameters [mm]						
	PLA	rPLA	PETG	CF-PLA	PLA +Hemp	rPLA +hemp	PETG +Jute
1	1.1	1.2	1.4	1.2	1	1.3	1.3
2	1.2	1.2	1.5	1.2	0.9	1.3	1.3
3	1.2	1.2	1.5	1.2	0.7	1.2	1.3
4	1.1	1.1	1.5	1.1	0.7	0.9	1.2
5	1.1	1.1	1.4	1.2	0.9	1.2	1.2

3.3.3 Sandwich structures

3.3.3.1 PLA with honeycomb/rhombus core structures

The FDM technique was used to manufacture the test specimens with the commercial 3D printer WANHAO Duplicator 6 and PLA (polylactic acid) material. PLA was chosen as the preferred material because of its growing popularity in FDM printing and its sustainable environmental characteristics. The filament used was 1.75 mm in diameter and black. As stated by the manufacturer, the filament's claimed qualities are tensile Young's modulus, ultimate tensile strength, strain at yield, and impact strength of 3.120 GPa, 70MPa, 5%, and 3.4 KJ/m2, respectively, when tested according to ISO 527. WANHAO 3D printer has a 0.4 mm nozzle diameter and exists in the additive-manufacturing laboratory at MATE (Szent Istvan University formerly), Gödöllő, Hungary. The test samples were printed with an infill density of 100% and a layer thickness of 200 μm at a print speed of 60 mm/s. The printing and building plate temperatures were set as 210 °C and 60 °C, respectively. Sandwiches typically consist of two skins (outer surfaces) and a core (inner structure). The core's material may be the same or unlike the skins. In the current study, the material utilized for both outer surfaces and inner structure was the same (PLA), and the manufacturing, by 3D printing, was done in solely a single stage. Two sandwich structures, a honeycomb and a rhombus (see Figure 3.12) have been used. These structures were designed by the standards ASTM C393 and MIL-STD-401B. A three-dimensional designing software SOLIDWORKS 2016 was used to generate the 3D structure model of the samples and convert it into an "STL" file format. To slice the STL file (3D model), Ultimaker Cura 4.7 software was employed to the manufacturing parameters are established. The designed specimens, with the honeycomb and rhombus sandwich structures, were prepared for the tensile, bending, and compression testing, as shown in Figure 3.12 a, b, and c, consecutively. Magnification for the sandwich structures' core shape is demonstrated in Figure 3.12: honeycomb core (left) and rhombus core(right).

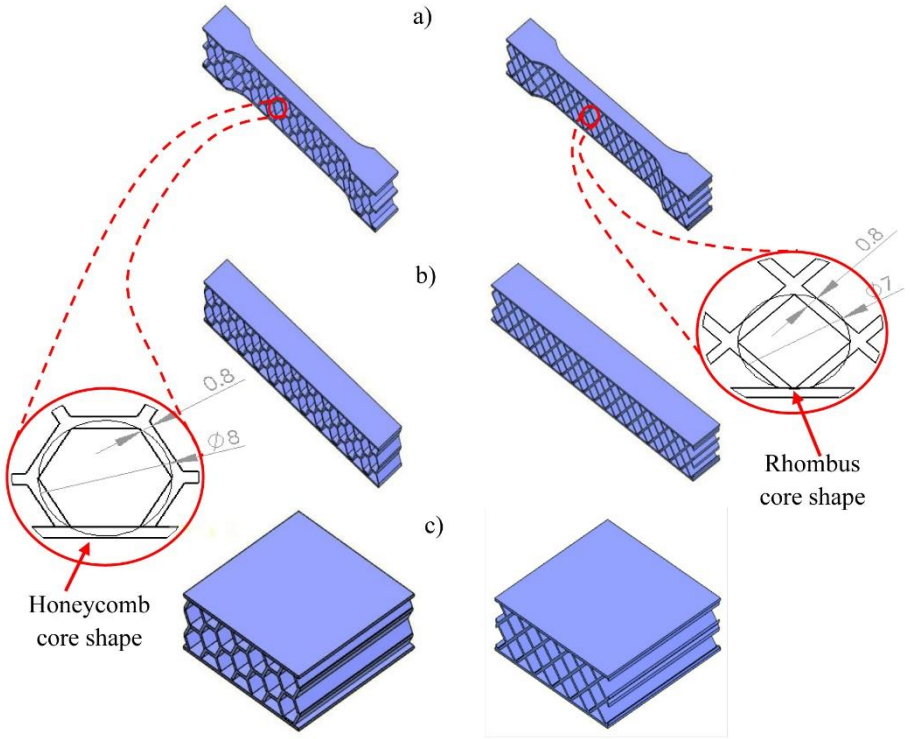

Fig.3.12. 3D models of the sandwich structure specimens of the honeycomb (left) and rhombus (right) patterns for a) tensile test, b) three-point bending test, and c) compression test

According to the appointed standards, the tensile and three-point bending tests specimens have the dimensions of 150 mm, 20 mm, and 15 mm for length, width, and height, respectively, with 0.75 mm as the thickness of the skin (see Figure 3.13 a-b). Also, the compression test samples were designed with a length of 50 mm, a width of 50 mm, and a height of 15 mm, at a skin thickness of 0.75 mm (see Figure 3.13 c). The specimens were built at an on-edge orientation, as illustrated in Figure 3.13 d.

Three identical specimens were 3D-printed for each test condition. The cell wall thickness should be sufficient so that it can be easily printable by the machine since too thin a cell wall thickness might make printing difficult and can deform the object. Therefore, the proper cell size was chosen to make the cell wall thickness thick enough to be easily printed. The chosen cell sizes were 8mm and 7 mm for the honeycomb and rhombus, respectively. In addition, the cell wall size for the honeycomb and rhombus was 0.8 mm (see core shape aside in Figure 3.12). However, it is worth noting that it is not easy to specify the accurate or optimal 3D printing parameters due to the anisotropic nature caused by the technology owing to the variety of its printers and materials (Ficzere et al., 2021). Figure 2d shows the actual appearance of some of the manufactured samples. The tensile specimens were produced with structure support owing to their geometry as there is a wide space under their gauge section. However, there was no need for structural support while creating the bending and compression test pieces.

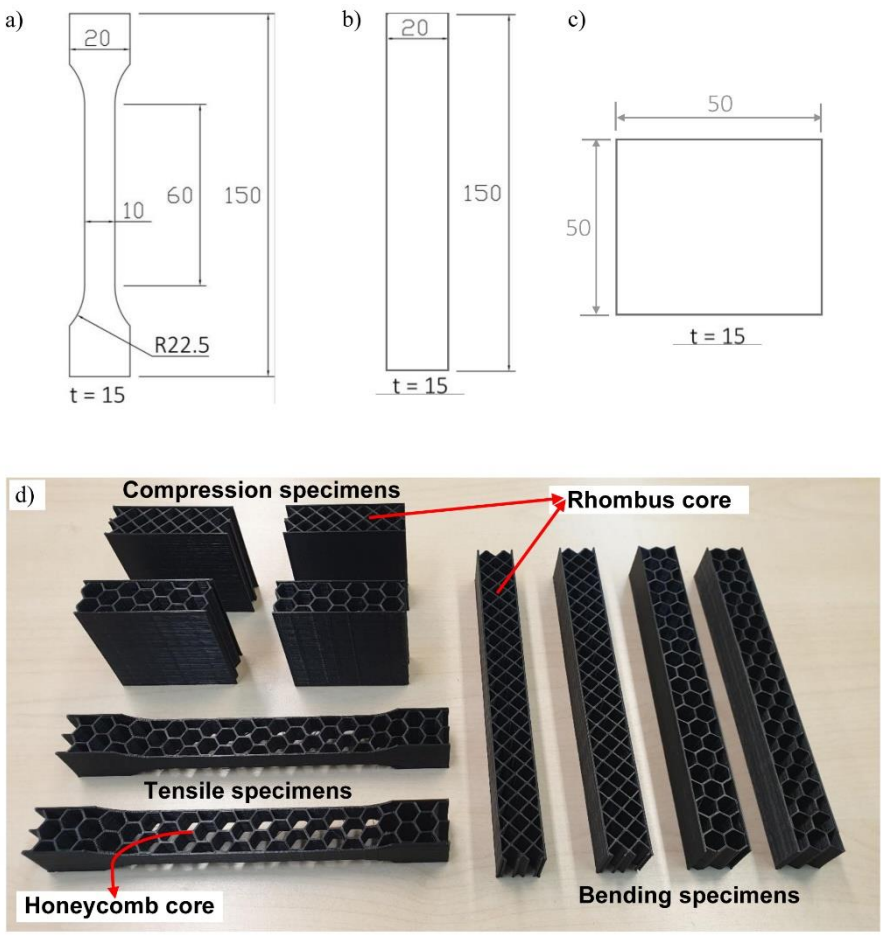

Fig. 3.13. Specimens' dimensions of a) tensile test, b) bending test, c) compression test; and d) physical appearance of some of the test specimens after 3D printing

Table 3.6. Average values of mass and density (with its standard deviation (SD)) of specimens tested

Structure	Mass (g)	$Volume_{solid}$ (mm^3)	$Density_{samples}$ (g/mm^3)	SD(±)(g/mm^3)
Tensile honeycomb	10.408	31500	$0.33*10^{-3}$	$6.73*10^{-6}$
Tensile rhombus	11.639	31500	$0.369*10^{-3}$	$4.93*10^{-7}$
Bend. honeycomb	14.955	45000	$0.332*10^{-3}$	$1.47*10^{-6}$
Bend. rhombus	17.228	45000	$0.382*10^{-3}$	$2.56*10^{-6}$
Com. honeycomb	12.063	37500	$0.321*10^{-3}$	$1.22*10^{-6}$
Com. rhombus	14.533	37500	$0.387*10^{-3}$	$1.15*10^{-6}$

3.3.3.2 Wood/PLA composites with re-entrant honeycomb core

The printing material used for both the face and core of the sandwich structure specimen was a wood filament (PLA-based with natural wood particles filament). The wood/PLA filament was a wooden color branded Spectrum with a diameter of 1.75 mm. According to the manufacturer, the filament has a density of 1150 kg/m³, a tensile strength of 47 MPa, and a modulus of elasticity of 2900 MPa. The CAD model of the sandwich structure was prepared using SolidWorks 2023 software and exported as an STL file. Printing was done on a Geeetech A20M 3D printer using Ultimaker Cura 5.2.1 software. The process was carried out at a temperature of 45 °C and 210 °C for the platform and printing head, respectively. The specimens were manufactured at a print speed

of 60 mm/s, with a layer thickness of 0.2 mm, an infill density of 100%, and a line printing pattern, using a nozzle diameter of 0.4 mm.

The compression and 3-point bending test samples were manufactured according to ASTM C365-00, “standard test method for flatwise compressive properties of sandwich cores,” and ASTM C393, “standard test method for flexural properties of sandwich constructions.” The designed specimens with the re-entrant honeycomb sandwich structure (see Figure 3.14) were prepared for the bending and compression testing. The re-entrant honeycomb structure is derived from the traditional hexagonal honeycomb but differs significantly due to its inward-sloping cell walls, which give it auxetic properties, allowing the structure to expand laterally when stretched (Tatlıer, 2022). This distinctive feature differentiates it from both typical honeycomb and trapezoidal designs. The use of re-entrant honeycomb in the sandwich composites was chosen for its enhanced mechanical behavior, including improved energy absorption and flexural response, as discussed in previous studies (Assidi & Ganghoffer, 2012; S. Yang et al., 2013; X. Zhang et al., 2015; Zied et al., 2015), Figure 3.14 is a magnification of the suggested and tested cell.

According to the specified standards, the bending test specimen had dimensions of 140 mm in length, 20 mm in width, and 10 mm in height (see Figure 3.15 a). In addition, the compression test specimen was designed and manufactured with a length of 50 mm, a width of 50 mm, and a height of 10 mm (see Figure 3.15 b). Bending and compression specimens were printed with different face layer (wall) thicknesses (0 mm, 0.8 mm, and 1.6 mm) in compression test specimens and (0.8 mm, 1.6 mm) in bending test specimens. The tensile specimen had dimensions of 150 mm in length, 20 mm in width, and 3 mm in thickness, with a gauge section length of 60 mm (see Figure 3.15c). For each test, the specimen was printed and tested three times, and the results in the paper are the average of three repeated test results. Figure 3.15 illustrates examples of specimen drawings generated using SolidWorks software. It is worth noting that this figure includes only a selection of representative drawings of the designed specimens; remaining drawings are detailed in the preceding text. Table 3.7 lists the average densities for the specimens analyzed.

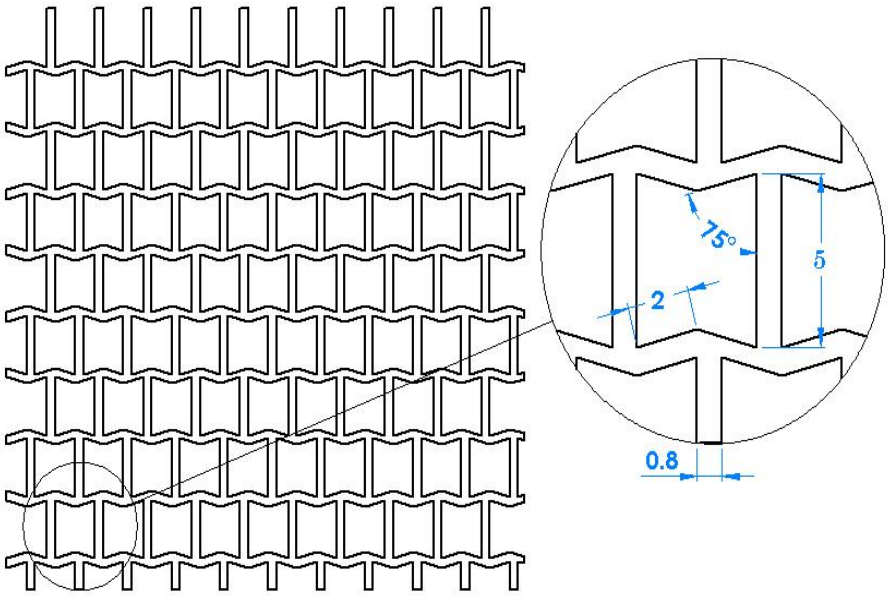

Fig.3.14. Design of re-entrant core unit cell.

Table 3.7. Average mass and density (with standard deviation) of the tested specimens.

Structure	Mass (g)	Volume $_{solid}$ (mm^3)	Density$_{struture}$ (kg/m^3)	SD (±) (g/mm^3)
Comp. – without face	8.584	7183.78	$1.2*10^{-6}$	$1.1*10^{-5}$
Comp. – with a face layer of 0.8 mm	12.51	11183.78	$1.12*10^{-6}$	$7.5*10^{-6}$
Comp. – with a face layer of 1.6 mm	16.82	15183.78	$1.1*10^{-6}$	$6.7*10^{-6}$
Bend. – with face layer of 0.8 mm, in-plane	12.94	11312.86	$1.14*10^{-6}$	$0.6*10^{-5}$
Bend. – with face layer of 1.6 mm, in-plane	17.33	15559.57	$1.113*10^{-6}$	$6.02*10^{-6}$
Bend. – with face layer of 0.8 mm, out-of-plane	13.11	10482.35	$1.25*10^{-6}$	$6.8*10^{-5}$
Bend. – with face layer of 1.6 mm, out-of-plane	17.35	14722.84	$1.18*10^{-6}$	$6.6*10^{-6}$

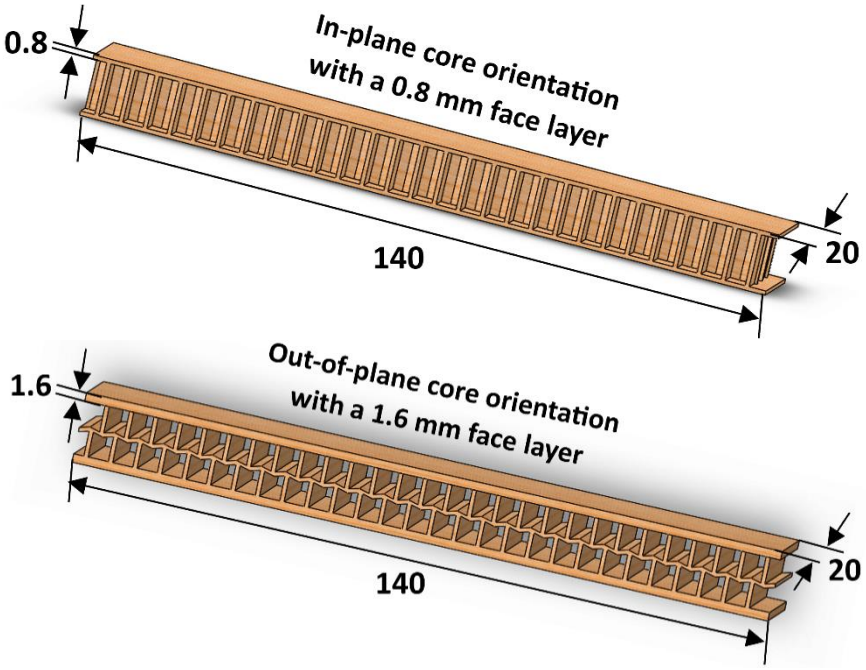

(a)

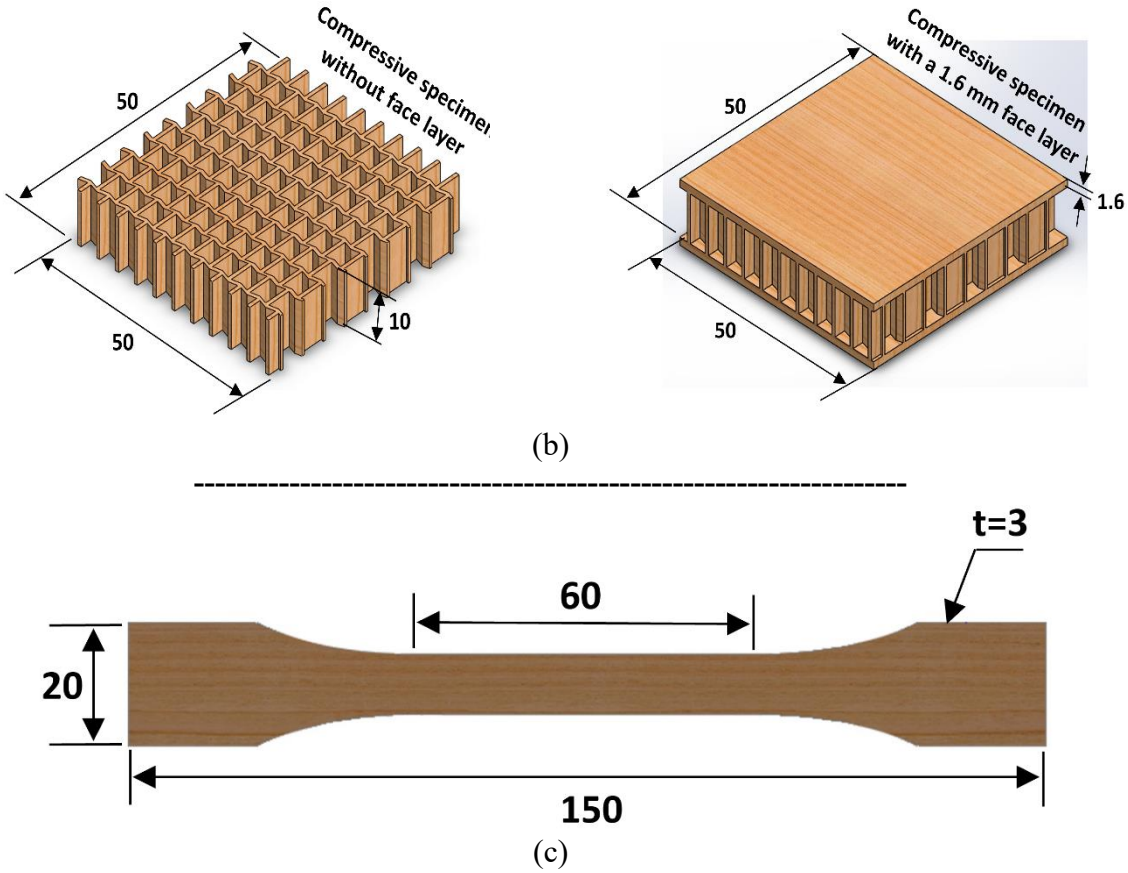

Fig.3.15. Shapes from SolidWorks for: (a) bending specimens with in-plane and out-of-plane core orientations and face layers of 0.8 mm and 1.6 mm thickness, (b) compressive specimens with face layers of 0 mm and 1.6 mm thickness, and (c) tensile specimen

3.3.4. Neat, single, and multi-gradient composites

In this investigation, four distinct types of polymeric filaments tailored for additive manufacturing were extruded. These categories included pure PLA and PETG polymers, as well as PLA and PETG polymeric composite filaments reinforced with 10 wt% carbon fiber. According to the material provider, the average length of the carbon fibers was 100 µm. The samples were created using a Bambu s1 MEX-type 3D printer, which is capable of additive manufacturing with up to four different materials in a layer-by-layer manner. In our experimentation, all four feedstock materials were used, with each material corresponding to a dedicated feeding system. The STL files of the samples were sliced into standard G-code for printing.

Tensile specimens of single-gradient composites, denoted as PLA/CF-PLA and PETG/CF-PETG, consisted of 50% PLA and 50% CF-PLA, and 50% PETG and 50% CF-PETG, as well as 50% PLA and 50% PETG. Additionally, multi-gradient composites were created using two specific combinations: PLA/CF-PLA (PCFP) and PETG/CF-PETG (GCFG). The PLA/CF-PLA setup featured 25% PLA on the outer layers and 50% CF-PLA in the central core (PCFPP). For the PETG/CF-PETG combination, 25% PETG was used for the outer layers with 50% CF-PETG as the core (GCFGG). Another variant, the PETG/PLA composite, included 25% PETG on the outer layers and 50% PLA in the inner core (GPG), Table 3.8 provides details on the previous specimens and their corresponding notations.

Table 3.8 shows a List of Acronyms:

MEX - Material Extrusion	Material Extrusion
P	100% PLA
G	100% PETG
PCFP	50% PLA + 50% CF-PLA
GCFG	50% PETG + 50 % CF-PETG
PCFPP	25% PLA + 50% CF-PLA + 25% PLA
PCFGG	25% PETG + 50% CF-PETG + 25% PETG
CFP	100% CF-PLA
CFG	100% CF-PETG
PG	50% PLA+ 50 % PETG
GPG	25 % PETG + 50% PLA+ 25% PETG

For comparison, additively manufactured samples of pure neat PLA, PETG, CF-PLA, and CF-PETG were also prepared, and their properties were assessed alongside various gradient composites. The selection of the multi-material design samples was based on optimizing material properties for specific structural applications. The choice was influenced by prior studies that demonstrated the benefits of combining materials with different mechanical characteristics to enhance overall performance (Palaniyappan et al., 2023; Yermurat et al., 2023). Figure 3.16 displays the schematic of the functional grading sequences for various PLA, PETG, and CF-PLA-CF-PETG composite layers. The samples were created with different gradient stacking arrangements, including both single and multi-gradient setups with varying percentages of stacking layers.

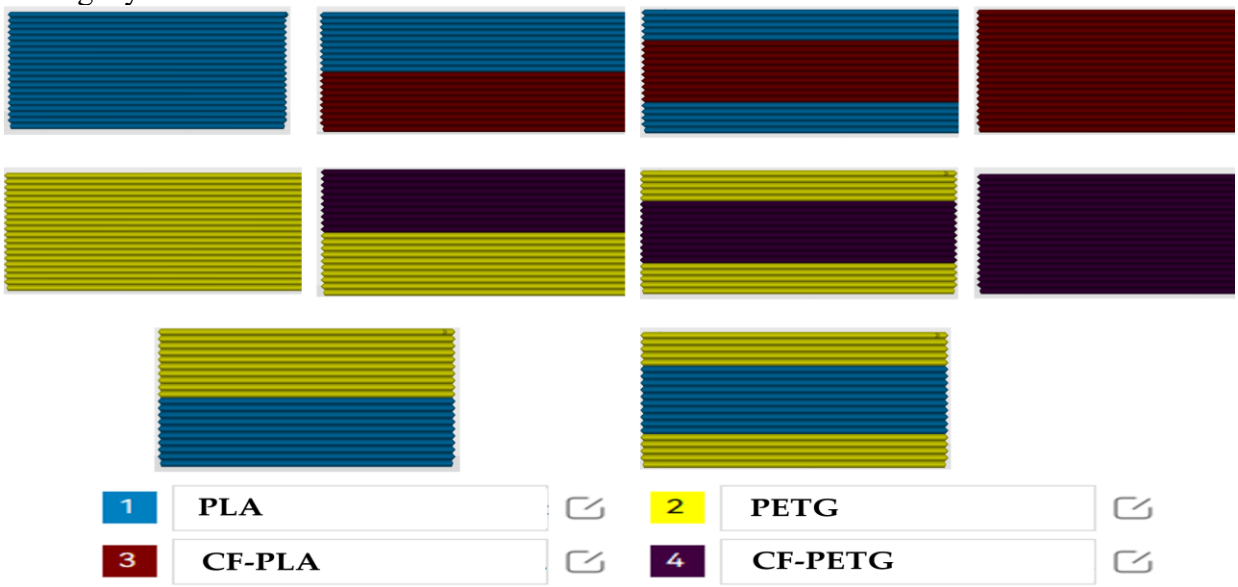

Fig. 3.16. Schematic of functional grading sequences for various multi-material tensile specimens, produced using Bambu Studio software.

The material properties of PLA and PETG produced under the specified printing parameters are outlined in Table 3.8. This study delved into the tensile strengths of the specimens,

determined by evaluating functionally specific volume ratios. For printing with PLA and CF-PLA, an optimal printing temperature of 210 °C was employed, while printing with PETG and CF-PETG required nozzle temperatures of 220 °C and 240 °C, respectively. Although Table 3.9 suggests an ideal bed temperature of 45 °C for PLA, a bed temperature of 70 °C was used for all prints involving PETG.

Table 3.9. Printing settings employed while manufacturing multi-materials using Bambu 3D printer.

Printing settings	**PLA**	**PETG**	**CF-PLA**	**CF-PETG**
Layer height [mm]	0.12	0.12	0.12	0.12
Initial layer height [mm]	0.2	0.2	0.2	0.2
Wall loops	2	2	2	2
Top/bottom layers	2	2	2	2
Infill density [%]	100	100	100	100
Infill pattern	Rectilinear	Rectilinear	Rectilinear	Rectilinear
Printing temperature [°C]	210	220	220	240
Platform temperature [°C]	45	70	45	70
Printing speed [mm/s]	50	50	50	50

3.4 Experimental testing of the 3d-printed specimens

3.4.1 Different tensile geometry shapes

The experiments in this study aimed to investigate the influence of tensile test specimens' geometry on the mechanical characteristics and mode of failure. The Zwick/RoellZ100, a universal testing device, was employed to evaluate the tensile strength of the specimens. There have been ten different sets of specimens were prepared (coming from five cases of standards with two build orientations), as shown in Figure 3.17 a , showcasing the diverse geometry shapes investigated. These specimen dimensions adhered to the standards outlined in ASTM D638, ASTM D3039 (0◦, 15◦, and 90◦), and ISO 527-2 for PETG polymer tensile testing. Three identical specimens printed with the same settings were tested from each set under similar conditions to ensure robustness and reliability. The tests were repeated three times to account for any potential variations. The obtained results were then averaged to obtain representative values. The evaluation of tensile behavior encompassed the determination of tensile strength, tensile Young's modulus, and the failure mode under the specified conditions. Figure 3.17 b highlights the technical importance of the extensometer used in the experimental setup. The extensometer, attached to the tensile test specimens during testing, enables precise measurement of elongation by providing high accuracy in differential movement measurement between two points. With a maximum error of only ±1 μm within the range of 20 to 200 μm, the extensometer significantly contributes to accurate elongation data and facilitates the calculation of Young's modulus. Moreover, the extensometer measurements allow for the determination of additional mechanical properties, such as nominal strain at tensile strength (εtm), stress at break (σB), strain at break (εB), and nominal strain at break (εtB).To conduct the tests, each specimen was securely fixed by the grips, as depicted in Figure 3.17. and stretched at a constant speed of 3 mm/min along its longitudinal axis until failure.

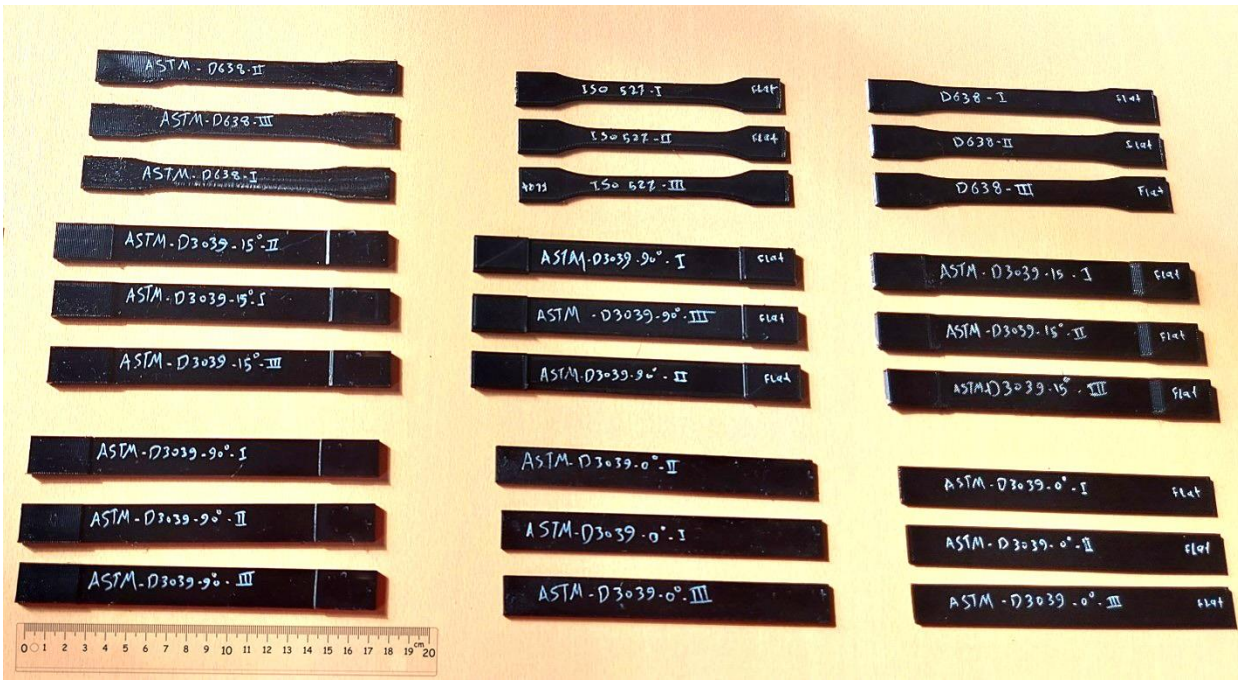

(a)

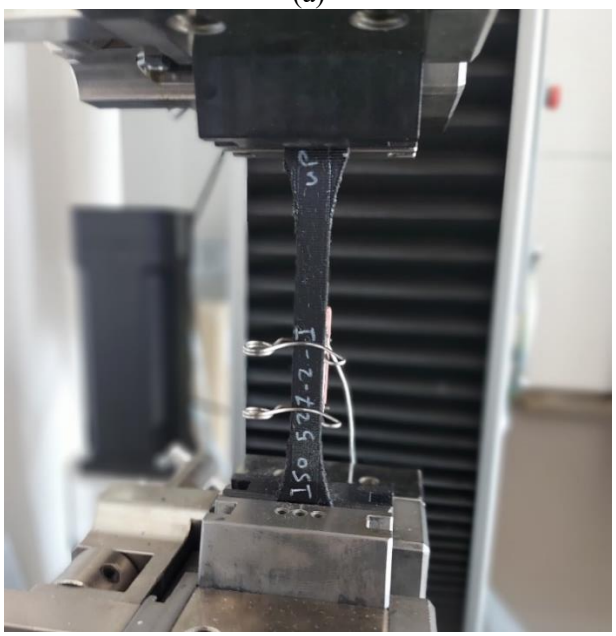

(b)

Fig. 3.17 Tensile testing (a) sets of tensile specimens of different geometries, and (b) extensometer attached to the specimen during tensile testing.

3.4.2 3D-Printed carbon fiber-reinforced polymer composites and pure polymers

Tensile tests were carried out according to the ASTM D3039 standard, while compressive tests adhered to ASTM D695, utilizing a Zwick/Roell Z100 test machine equipped with a 10 kN force transducer. The tests were conducted at a 5 mm/min displacement rate, and the grip-to-grip

distance was maintained at 99.8 mm. The force-displacement data were collected via computer using data acquisition software. Tensile properties assessed included tensile strength, tensile Young's modulus, and failure modes under prescribed conditions. The modulus of elasticity was experimentally determined within the elastic range, employing an extensometer to evaluate strain rate sensitivity (viscoelasticity). For each material, three specimens underwent tensile strength testing.

Compressive strength was computed by dividing the compressive load by the specimen's cross-sectional area. Compressive strain was determined using equation (3.4), and compressive modulus was calculated using equation (3.5).

$$\varepsilon = \frac{\Delta l}{l0}, \tag{3.4}$$

where Δl is the elongation and L_0 is the length of the sample.

$$E = \frac{\sigma}{\varepsilon}. \tag{3.5}$$

3.4.3 Re-manufactured filaments

- Filament fixation

In this study, the tensile properties of the original filaments (not printed specimens and 3D specimens) and the re-manufactured filaments (not printed into a specimen), such as ultimate tensile strength and fracture strength, were determined at a crosshead speed of 5 mm/min, with a minimum of five repetitions for each test. Filaments 300 mm in length were clamped using Bollard-style grips (see Figure 3.18). The bollard part of the fixture had a diameter of 120 mm, consisting of two cylindrical grips mounted on a Zwick Roell Z100 tensile testing machine. Testing was performed at a displacement rate of 5 mm/min, with a distance of 150 mm between the grips. One grip was secured in place, while the other was adjustable. The adjustable grip was attached to the load cell of the testing machine, which recorded the force exerted on the specimen.

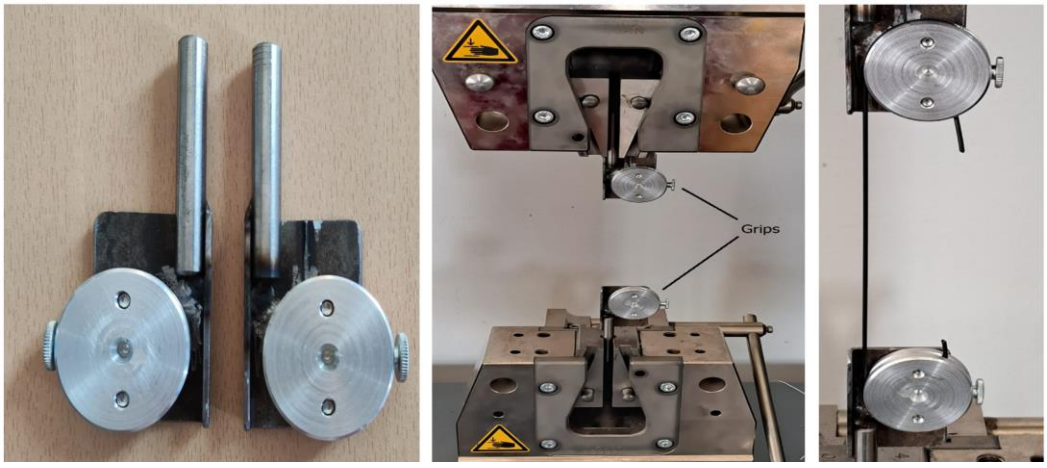

(**a**) (**b**) (**c**)

Fig. 3.18. Tensile testing of filaments: (a) bollard grips used, (b) grip positioning within the test machine, and (c) close-up view of the grips.

3.4.4 Sandwich Structures

3.4.4.1 Mechanical characteristics of honeycomb/rhombus core structures

Three repeated tests have been accomplished on the samples that were constructed for each configuration of the sandwich structure's core (honeycomb and rhombus). The following sections clarify the conditions and details of the tests performed.

- **Tensile testing**

The ISO standard 527 for tensile testing of polymers (B. ISO, 2009) was used to assess the tensile properties of the built structures. The tensile behavior determination included the tensile strength, tensile Young's modulus, and the failure form under the specified conditions. According to the ISO 527-2:2012 standard (Iso, 2012b), the specimens were stretched at a steady speed of 1 mm/min along their main axis until they broke.

Equation (3.6) was used to calculate the tensile strength (σ_t) of sandwich specimens

$$\sigma_t = P_t/A_t, \tag{3.6}$$

where P_t stands for the ultimate load (N), while the sandwich specimen's cross-sectional area is represented by A_t (mm^2) in our study we chose the broken cross-section area where it was in the middle of the specimens. The cross-section area was calculated using SolidWorks software and was: 30 mm^2, and 32mm^2 for the honeycomb and rhombus, respectively. For this, the Solidworks software was used to find and calculate the smallest cross-sectional area, as illustrated in Figure 3.19, where it was 30 mm^2 and 32 mm^2. for honeycomb and rhombus, respectively.
Tensile modulus (E_t) was calculated by Hooke's law

$$E_t = \sigma_t/\varepsilon, \tag{3.7}$$

as ε is the strain,

To get a more accurate value of Young's modulus (Et), two points were fitted on the stress-strain curves of the sandwich specimens to draw the slope and determine the tensile modulus. These two points were specifically at 10% and60% from each axis on the stress-strain curve (i.e., the values of σt and ε were picked at 10% and 60% and then substituted into the slop equation (3.8);

$$\sigma\ t(\text{at } 60\%) - \sigma t\ (\text{at}10\%) \ /\ \varepsilon(\text{at } 60\%) - \varepsilon(\text{at } 10\%) \tag{3.8}$$

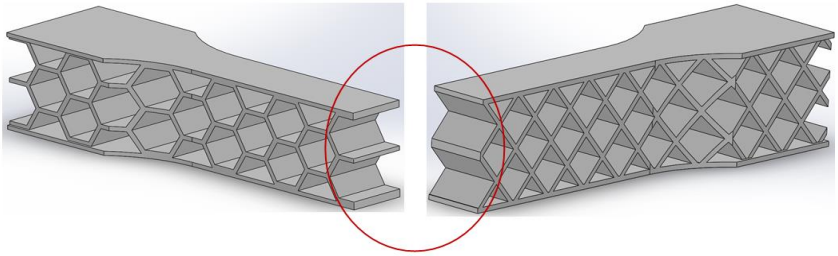

Fig.3.19 The cross-sectional area of tensile specimens determined by the Solidworks software

- **Bending Testing**

The bending tests (three-points) were carried out following ASTM C 393 The crosshead speed of the tests was 1 mm/min until the specimen broke. In the three-point bending, the radius of supports and punch was 15 mm, and the span length was 100 mm. Figure 3-20 presents the experimental procedure used for the three-point bending tests on the sandwich specimen with a re-entrant honeycomb structure. The left side of the figure shows a cross-sectional view of the tested sample, while the right side illustrates the experimental setup together with the key test parameters. Equations (3.9-11) were used to calculate the values of bending strength (σ_b) as well as the bending modulus (E_b) of sandwich samples (Zaharia et al., 2020).

$$M = \frac{P_{max} * L}{4} \tag{3.9}$$

$$\sigma_b = \frac{M.y}{I} \ , \ y = \frac{h}{2} \tag{3.10}$$

$$E_{bend} = \frac{L^3.F_{max}}{4.w.d^3.\Delta L} \tag{3.11}$$

Where: I: the moment of inertia (mm^4) calculated using solidwork software, M: Maximum Bending Moment (N.mm), P_{max}: the maximum applied load (N) (maximum applied load at the loading point of the beam, used to calculate the maximum bending moment and bending stress), *h:* the total thickness of the structure (mm), *L:* Length of the specimen between the supports (span length) (m), *d:* Thickness of the specimen (m), F_{max}: Maximum load applied (N) (is the force corresponding to the measured displacement used to calculate the bending modulus), ΔL: Deflection at the center (m), *w* is the specimen width (mm), Figure 3.20c presents the three-point bending test setup used for the determination of the moment of inertia

For the honeycomb and rhombus cores, homogenization was applied by considering them as effective solids with average density values, as reported in Table 3.6. This ensured consistency between the design geometry, the measured mass, and the effective cross-sectional properties used in the calculations.

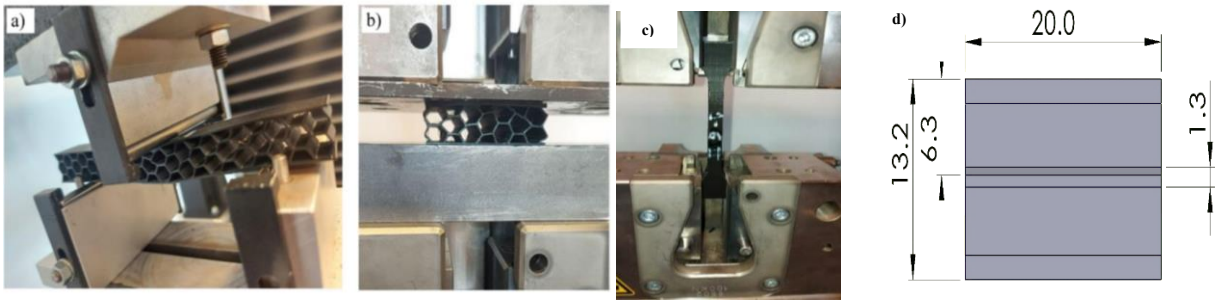

Fig.3.20: Experimental setup of testing one of the sandwich structures (honeycomb) for the tests of a) three-point bending, b) compression, c) Tensile, d) key geometrical parameters used in Equation (3.10).

.

- **Compression testing**

The sandwich structure specimens were compressed on a mechanical test machine (Figure 3.20 b). The tests were performed at a 1 mm/min crosshead speed. For reliable results, each lightweight sandwich construction investigated (honeycomb and rhombus) was subjected to three tests. The average cross-sectional area (A_{av}) was determined based on the relationship between mass, density, and geometry. This method enables accurate estimation of the effective load-bearing area, taking into account the internal core geometry and material usage.

For a solid PLA reference specimen of the same nominal dimensions (thickness t and length), the cross-sectional area is given by:

$$A_{PLA} = \frac{M_{PLA}}{\rho_{PLA} * t} \tag{3.12}$$

where: (A_{PLA}) cross-sectional area of a solid PLA specimen (mm²), (M_{PLA})measured mass of the solid PLA specimen (g), (ρ_{PLA})density of solid PLA (g/mm³), (t) specimen thickness (mm).

Similarly, the average cross-sectional area of a sandwich structure specimen (A_{av}) can be expressed as:

$$A_{av} = \frac{M_{str}}{\rho_{PLA}.t} \tag{3.13}$$

where M*str* is the measured mass of the printed sandwich specimen.

However, rather than directly measuring M*str* , it is often more convenient to relate it to the solid reference specimen using the density ratio:

$$\frac{\rho_{av}}{\rho_{PLA}} = \frac{M_{str}/_V}{M_{PLA}/_V} = \frac{M_{str}}{M_{PLA}} \tag{3.14}$$

Rearranging:

$$M_{str} = M_{PLA} * \frac{\rho_{av}}{\rho_{PLA}} \tag{3.15}$$

Substituting into the expression for A_{av}:

$$A_{av} = \frac{M_{PLA}}{\rho_{PLA}.t} * \frac{\rho_{av}}{\rho_{PLA}} \tag{3.16}$$

Since: $\frac{M_{PLA}}{\rho_{PLA}.t} = A_{PLA}$

The Final Simplified Formula:

$$A_{av} = A_{PLA} * \frac{\rho_{av}}{\rho_{PLA}} \tag{3.17}$$

The density (ρ_{av}) of the sandwich structure compression specimens is 0.32×10^{-3}(g/mm^3) for honeycomb and 0.39×10^{-3} (g/mm^3) for rhombus, as listed in Table 3.6.

Additionally, the density of the PLA material (ρ_{pla}), in the case of a solid bulk, is1.252×10^{-3} (g/mm^3).

To verify these analytical estimates, the specimen geometries were also modeled in SolidWorks, and the theoretical cross-sectional properties were extracted directly from the CAD models. This dual approach (analytical and CAD-based) ensured consistency between the design intent and the printed geometry.

3.4.4.2 Wood/PLA Composites with Re-Entrant Honeycomb Core

For simulation studies, Young's modulus and yield strength were derived from the uniaxial tensile test. The Zwick/Roell Z100, a universal testing machine, was utilized to conduct three-point bending and compressive strength tests on the sandwich structure specimens. Accurate characterization of properties requires measuring the base material properties. Following the ISO 527, flat tensile test specimens were 3D printed using wood/PLA material (Figure 3.20), and three tensile specimens were manufactured using the printing parameters mentioned in Section 3.3.3.2.

(a) (b)

Fig 3.20. Tensile tests: (a) specimens with ISO 527 geometry, (b) uniaxial tensile testing experimental setup.

The average bending strength and bending modulus were determined by testing three specimens in each case with a 3 mm/min crosshead speed. Tests were carried out until the samples' fracture points. The load was applied by a 7.5 mm diameter cylindrical central roller, with two exterior 5 mm diameter cylindrical rollers as supports, and the span length was 80 mm. Force–displacement measurements were recorded as the output of the testing machine. The three-point bending strength (see Figure 3.21) was tested with different thicknesses of top and bottom layers (0.8 and 1.6 mm) and different directions of the core structure (both in-plane and out-of-plane).

(a) (b)

Fig 3.21. Bending test of two sandwich structure specimens: (a) in-plane direction of the re-entrant core with a thickness of 0.8 mm, (b) out-of-plane direction of the re-entrant core with a thickness of 1.6 mm.

It is argued that various factors, including the type of core material, fabrication method, testing speed, core geometry (specifically cell size), and the testing environment, significantly affect the samples' compressive strength. The compressive strength (both parallel (edgewise) and vertical (flatwise) to the surface) for different thicknesses of the top and bottom layers (0.8 and 1.6 mm) was examined on three specimens according to the ASTM C364/C364M standard. According to the standard, the crosshead speed for the compression test was set to 5 mm/min (see Figure 3.22).

(a) (b)

Fig 3.22 Compressive test of two different specimens: (a) parallel to the surface (edgewise), (b) perpendicular to the surface (flatwise).

- **The finite element method**

To provide in-depth insights into the mechanical behavior of re-entrant honeycomb sandwich structures, facilitate accurate stress analysis, and performance prediction, numerical simulations were conducted using ANSYS Workbench 16.0. The FEA validation was performed for bending and compression tests only, while tensile data were used exclusively to define the elastic material property for the simulations. These simulations allowed us to analyze the sandwich structures' responses to three-point bending and compression, as well as identify where stress concentrations might occur. The software incorporated specimen dimensions and material properties, including the solid samples' compressive, bending, and tensile properties. Young's modulus and yield strength were obtained from uniaxial tensile tests, while ultimate compressive strength and bending strength were obtained from compression and bending tests. The flexural strength was calculated using Equation (3-18):

$$\sigma_f = \frac{3FL}{2bh^2} \tag{3-18}$$

where: F is the applied load (N), L is the span length between supports (mm), b is the width of the specimens (mm), and h is the thickness of the specimen (mm)

The compressive strength of a sandwich composite was calculated using Equation (3-19), Additionally, the effective compressive strength was calculated using Equation (3.20)

$$\sigma_c = \frac{F}{A} \tag{3-19}$$

where: F is the applied compressive load (N) and A is the cross-sectional area of the specimen (mm^2).

$$\sigma_c^{eff} = \frac{\sigma\ face * t\ face}{t\ core + t\ face} \tag{3.20}$$

where: σ_{face} is the compressive strength of the face sheets (MPa), t_{face} is the thickness of the face sheets (mm), and t_{core} is the thickness of the core material (mm).

However, since the specimens in this study are sandwich structures with re-entrant honeycomb core, the classical beam theory cannot be directly applied due to their non-uniform geometry. Therefore, the actual geometric properties (e.g., second moment of area, I) were extracted from SolidWorks models of each specimen, which provided accurate values based on the real printed structure. These CAD-based properties were then used in the flexural stress and modulus calculations, ensuring consistency with the structural configuration.

This approach is consistent with previous studies, where the standard equation is presented for clarity, but detailed geometry is obtained from CAD or numerical methods for sandwich structures (Kladovasilakis et al., 2021; Zaharia et al., 2020; Zoumaki et al., 2022).

The re-entrant core structure is inherently anisotropic due to its unique geometry and the re-entrant design of the honeycomb cells. This anisotropy arises because the mechanical properties of the structure vary with direction. The core is also heterogeneous in composition and design, featuring varying geometrical features and sometimes differing materials within the honeycomb pattern. The simulations employed a linear elastic material model with the material defined as wood/PLA composite (as tested), with constants including a modulus of elasticity of 2085 MPa, a Poisson's ratio of 0.33, and a density of 1150 kg/m^3 (Dharmalingam et al., 2022; Vakharia et al., 2021; X. Wang et al., 2019).

During the finite element meshing process, careful consideration was given to the mesh sizes of the specimens. Consequently, the most appropriate mesh size and mesh combination were used in the model. Figure 3.23a and 3.23b show the meshing of CAD models of bending and compression specimens. Defining the structure, material properties, contacts, applying loads, and boundary conditions were all part of finite element modeling. The material chosen for the fixed supporting rollers and the loading central roller in the three-point bending analysis was stainless steel 316L. Loading was performed by applying a gradual displacement consisstent with the strain rate of the experimental study to the upper cylinder (roller), while the two other cylinders (rollers) served as fixed supports. A single surface and friction contact (COF = 0.1) was established between core elements to prevent interpenetration during bending, and all contacts were assumed to be friction. A fixed support boundary condition was set at one end of the CAD-modeled samples to simulate the compression test, and a gradual displacement consistent with the experimental study's strain rate (5 mm/min, and 3mm/min) was set at the other end. Figure 3.23c and 3.23d show the boundary conditions of the bending and compression simulation tests. Model calibration used tensile-test data to set the elastic modulus of the printed material; validation relied on comparing bending/compression responses (load–deflection curves and peak load) between simulation and

experiment. Because the analysis is linear elastic, stress comparisons at a given applied load are independent of the selected modulus, whereas deflection/stiffness are modulus-dependent. Accordingly, agreement is reported for both stress at load and stiffness.

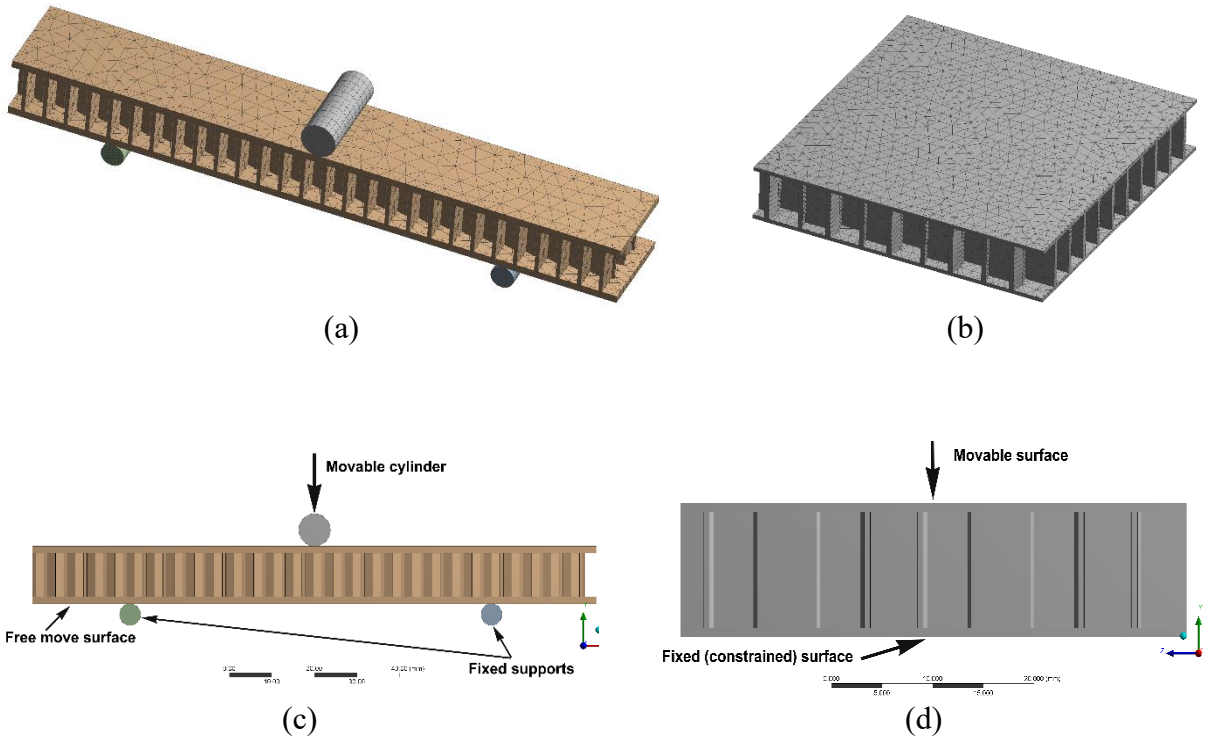

Fig 3.23. Meshing of the CAD model for the 0.8 mm face of (a) bending (in-plane), (b) compression (flatwise); and boundary conditions for (c) bending (in-plane), (d) compression (flatwise).

While these materials exhibit direction-dependent behavior due to their fiber structure and the additive manufacturing process, using a linear elastic approximation is a common and practical starting point in FEM, particularly for capturing global behavior and identifying stress concentrations in complex geometries like re-entrant honeycomb cores. Prior studies (Nukala et al., 2023) have shown that linear elastic models can yield results that align closely with experimental outcomes for 3D-printed fiber-reinforced composites. Although they do not fully account for anisotropy or nonlinearities, such models offer computational efficiency and are suitable for preliminary structural analysis.

3.4.5 Neat, Single, and Multi-Gradient Composites

Tensile specimens of the various multi-material configurations, including those with gradient additives, were fabricated according to ISO 527-2-1B standards. These specimens were designed with dimensions of 150 mm in length, 20 mm in width, and 4 mm in thickness. The tensile strength and modulus of the prepared samples were assessed using the Universal Testing Machine Zwick/Roell Z100, applying a tensile loading rate of 1 mm/min. Each set of 3D-printed multi-material samples underwent three repetitions of testing. A representation of the tensile test samples is illustrated in Figure 3.24.

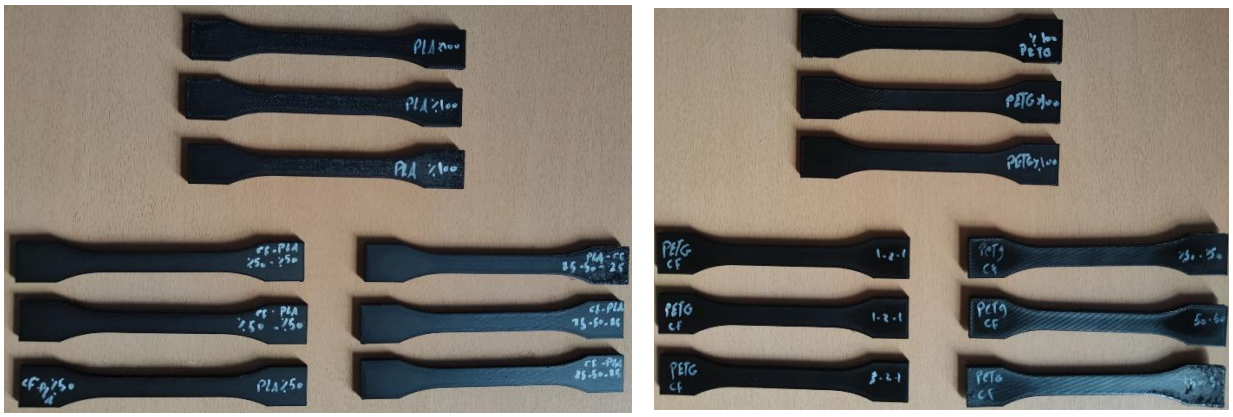

(a) (b)

Fig 3.24. The physical appearance of some of the tensile specimens: (a) PLA, CFPLE, (b) PETG, CFPETG

4. RESULTS AND DISCUSSION

The experiments' results are presented in this chapter, as well as discussions suggesting the new findings. These include mechanical characteristics for different 3D printing FDM and materials (neat and composite for each technique) by assessing the results of sandwich structures, multi-materials, and testing (such as tensile, compressive, bending, and microstructure.

4.1 Different tensile geometry shapes

4.1.1 Experimental results

Various variables, as discussed in the literature, can effectively increase stiffness and strength. The major variables that influence deformations and deflections include material properties, layer binding, and FDM 3D printing parameters (mainly, infill pattern and build orientation). To delve deeper into the characteristics of build orientations, it is helpful to look at the structure of printed tensile test specimens in Figure 3.4. Every layer has inner lines and a shell (contour). The direction of the layer contour for the flat sample is parallel to the applied tensile test force. These specimens exhibited a higher likelihood of elongation due to the presence of long internal lines constructed at a 45° angle and a sufficient number of layers, resulting in increased strain. The on-edge workpiece possesses a complex structure characterized by a cross-section with numerous layers, a narrow contour, and short internal lines. This explains how these samples were pulled with a great degree of strength during the test.

The theoretical masses of the printed specimens were derived from the slicing software, whereas the actual masses were determined using a precision scale with an accuracy of ±0.01 g. In addition, the cross-sectional areas of the specimens were calculated to enable a more comprehensive comparison. The results, summarized in Table 4-1, reveal that the experimentally measured masses are consistently lower than their theoretical counterparts. This deviation, though minor, reflects the inherent variability of the printing process and highlights the subtle gap between digital design and physical realization.

Table 4-1 Comparison between theoretical masses, measured masses, and cross-section area.

Specimens	Flat		On-edge		Cross-section area (mm^2)
	real mass (g)	slicer- mass (g)	real mass (g)	slicer- mass (g)	
ASTM-D638	8.49	9.13	8.63	9.28	39
ASTM-D3039-0°	11.04	11.88	11.24	12.09	60
ASTM-D3039-15°	11.83	12.72	11.76	12.65	40
ASTM-D3039-90°	8.17	8.79	8.83	9.49	40
ISO 527	4.89	5.26	5.19	5.58	30

The load-displacement curves that were obtained from the tensile test for all examined shape geometry and orientations are shown in Figure 4.1. It is clear that the building orientation of the 3D printing parameter and the shape geometry has a significant impact on the values of force versus elongation. The results were divided into two diagrams according to the building orientations and the shapes of tensile standards examined. The highest applied loads required to reach the fracture, for the different shape geometry, were reported to the ASTM D3039-0° (for

both flat and on edge), as shown in Figure 4.1. The average values (out of three testing results for each orientation) of these highest loads obtained were 1693 N and 2632 N for flat and on edge orientation, respectively. Comparably, ASTM D638 standard specimens also showed a relatively high load ranging between 1562 N and 1890 N for flat and on-edge orientation, respectively. In contrast, the lowest loads were reported in specimens of the ASTM D3039-15° (at the flat build orientation) and ISO 527 (at the on-edge build orientation) with the values 1026 N and 1475 N, consecutively.

In terms of the Young's modulus, the flat build orientation values were ranged between 1188 MPa and 1622 MPa, where the best values were from ASTM 3039-0°. On the other hand, the tensile modulus of the on-edge build orientation ranged between 1660 MPa and 2773 MPa, and the better values were from ASTM D3039-90° (see Figure 4.2b). In addition, the Young's modulus of ASTM D3039-0° was 26.74% and 40.15% higher than the ISO 527 geometry shape (the lowest modulus) for the flat and on-edge orientations, respectively. In comparison between ASTM D638 and ISO 527, the average of ASTM D638 specimens was 14% and 21% higher than the ISO 527 geometry shape for flat and on-edge orientations, consecutively. Concerning the tensile strain (see Figure 4.2 c), which was determined at the yield strength, its values ranged between 2.73% and 4.21% (for both orientations). The ASTM D3039-0° and ASTM D638 specimens exhibited the highest values, while the ISO 527 specimen showed the lowest value. The tensile strain average value of the ASTM 3039-0° at on-edge orientation was 9.5% higher than the flat orientation of the same shape.

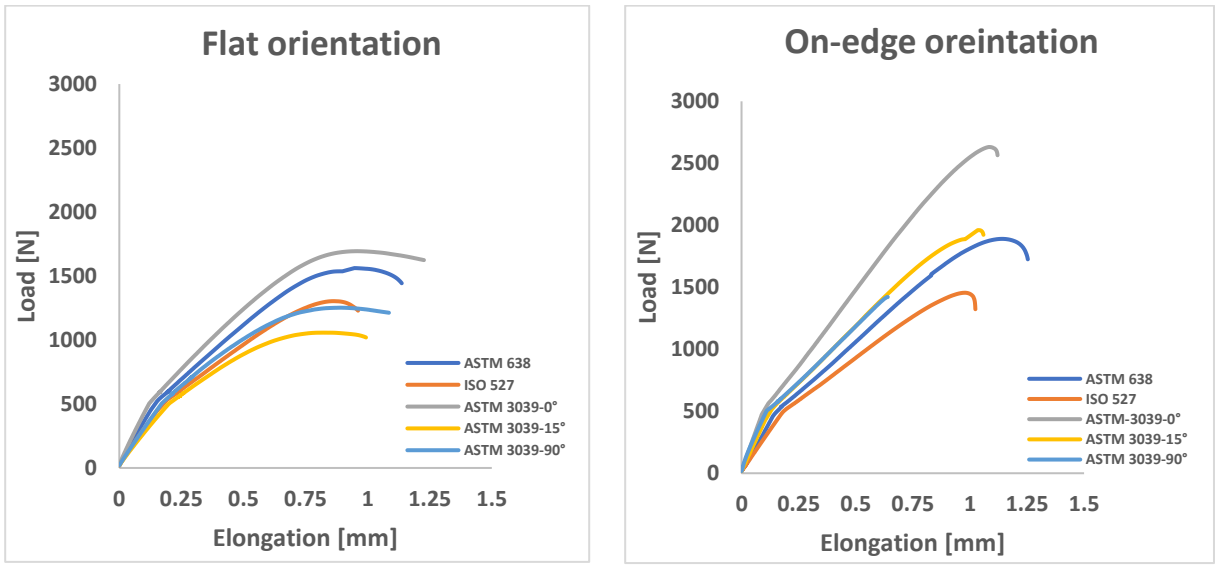

(**a**) (**b**)

Fig.4.1. Load-displacement curves for (a) flat building orientation and (b) on-edge orientation.

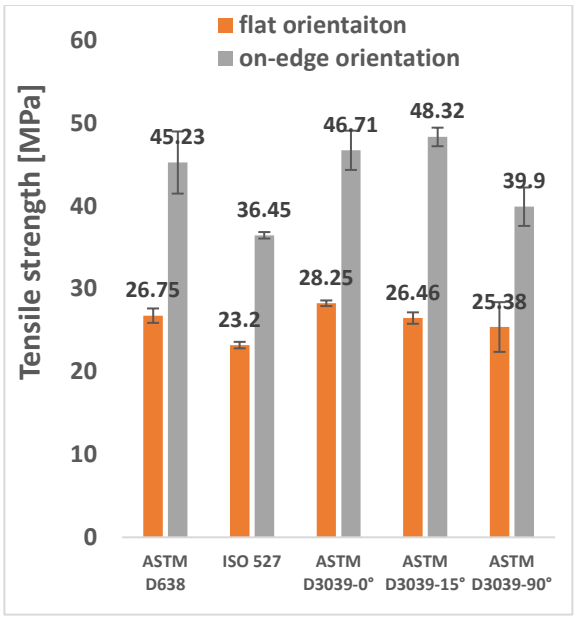

(a)

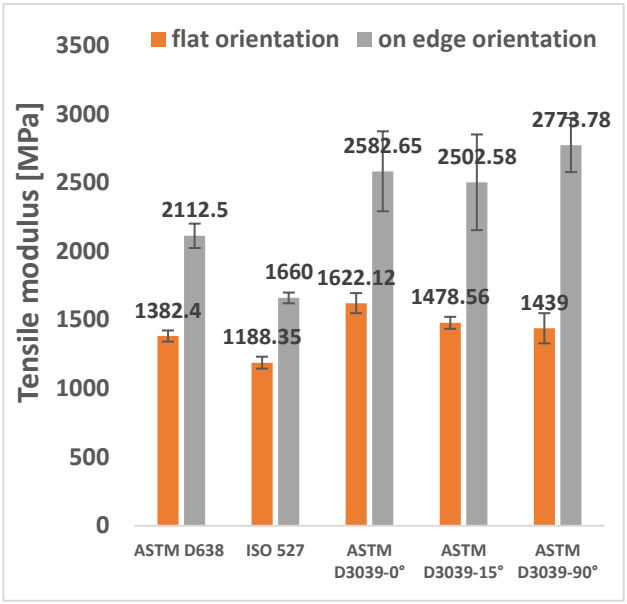

(b)

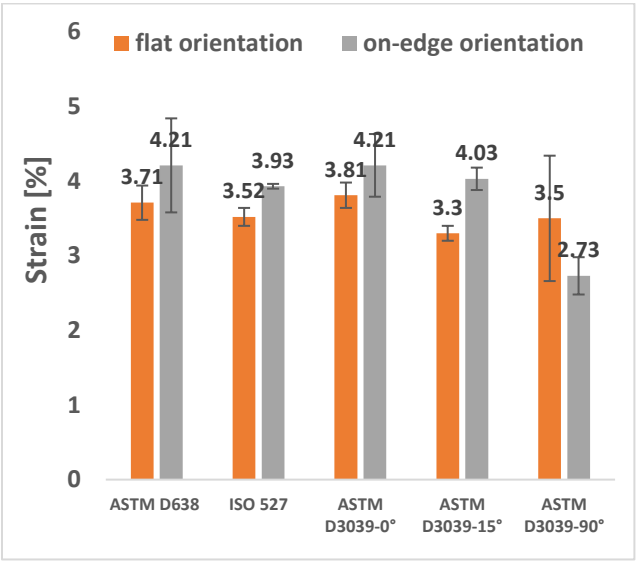

(c)

Fig 4.2. Results of different geometry shape specimens during tensile test for flat and on-edge build orientations (a) tensile strength, (b) tensile Modulus, and (c) tensile strain.

Table 4.2 presents the average values of various tensile test mechanical properties for each geometry shape. The results demonstrate notable variations in the mechanical behavior of the specimens. While: Ɛtm (nominal strain at tensile strength), Ɛb (strain at break), σb (stress at break), and Ɛtb (nominal strain at break)

Table 4.2. The average value of Ɛtm, σb, Ɛb, and Ɛtb for each geometry shape examined.

Specimen's standard	Ɛtm (%)	Σb (MPa)	Ɛb (%)	Ɛtb (%)
ASTM-D638-Flat	4.7	19.5	4.7	5.7
ASTM-D638-On-edge	5.9	19.9	9.5	11.2
ISO 527-Flat	4.6	13.4	4.4	5.6
ISO 527-On-edge	5.6	17.1	7.5	9.2
ASTM-D3039-0°-Flat	4.2	22.79	7	7.5
ASTM-D3039-0°-On-edge	5.23	44.3	4.5	5.2
ASTM-D3039-15°-Flat	3.9	23.3	5.2	5.8
ASTM-D3039-15°-On-edge	5.4	48.3	4	5.4
ASTM-D3039-90°-Flat	3.7	16.8	3.8	4.2
ASTM-D3039-90°-On-edge	4.4	37.9	2.7	4.4

By testing FDM dog bone shape specimens, (Kay, 2014) credited the lower tensile strengths and a higher degree of disassembling to the use of ASTM D638, which is not recommended (according to him). The researcher highlighted how failures frequently happened in the neck area of dog bones manufactured with FDM as a result of stress concentration in the part's transition zones. Nevertheless, notable enhancements were observed when conducting tests on parts in accordance with ASTM D3039. It is important to note that ASTM D638 is primarily intended for testing conventional polymeric bulk materials, while the additive manufacturing parts in question more closely resemble composite structures (Kay, 2014). Conversely, ASTM D3039 is specifically tailored for evaluating composite materials based on their geometry.

Figure 4.3 shows the broken specimens after the tensile test. As it is well known, the breakage/failure is much better to be in the middle of the gauge section than other parts of specimen. Obviously from Figure 8, the broken area for the on-edge orientation was always near the edge of the specimen; the breaks near the gripping area, which is not recommend. In general, the on-edge orientation of FDM samples tends to yield higher strength, as indicated by the findings from various standards investigated. However, the impact of orientation is particularly notable when considering the ASTM D638 and ISO 527 standards. These observations align with the results reported by (Aliheidari et al., 2017), supporting the notion that the mechanical properties are directly influenced by the distinctive characteristics of the layered structure, specifically the adhesion between the layers. In contrast, the fracture in most of the flat printed specimens was almost in the middle.

(**a**) (**b**)

Fig.4.3. Specimens' broken area (a) flat orientation and (b) on-edge orientation.

To distinguish in which geometry shape and printing parameter the specimen's failure was better, the broken area was given a percentage out of 100% (called the good breakage area) considering the fracture place from the middle of the sample; the closer to the middle the higher the percentage, and vice versa. Therefore, if the broken area is near the neck/edge, then it is not considered to get the good fracture. Figure 4.4 shows the percentage of the good breakage area based on the specimens' fractures depicted in Figure 4.3.

When examining fracture surfaces of tensile specimens using an optical microscope, the flat and on-edge orientations offer distinct insights into the material's fracture behavior. The flat orientation allows for a detailed analysis of surface features, crack patterns, and material characteristics, providing valuable information about the material's response to external forces (see Figure 4.5a and 4.5b). In contrast, the on-edge orientation exposes layered structures, internal defects, and interfacial characteristics, offering a deeper understanding of the material's internal properties and structural integrity (see Figure 4.5c and 4.5d). By combining these observations, a comprehensive understanding of fracture mechanisms, contributing factors, and the material's overall response to stress can be achieved. The fracture surfaces observed in both the flat and on-edge orientations exhibit characteristics typically associated with brittle fractures, as demonstrated in Figure 10, which showcase optical microscope images of the fractured specimens. The flat specimen fractured at an angle of 45°, aligning with the structure of its raster direction. On the other hand, the on-edge specimens displayed a fracture angle of 90°. Notably, despite the difference in fracture angles, the on-edge test piece exhibited higher tensile strength, attributed to the robust design of the inner lines and the presence of doubled shell layers. These structural features contribute to improved mechanical properties and enhanced structural integrity, leading to the observed increase in tensile strength.

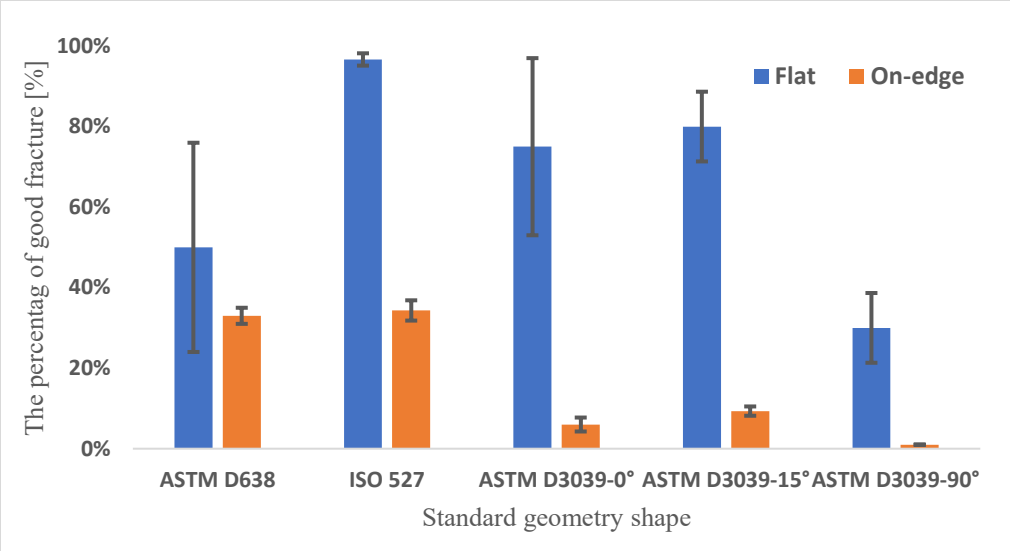

Fig.4.4. The percentage of good breakage area of specimens.

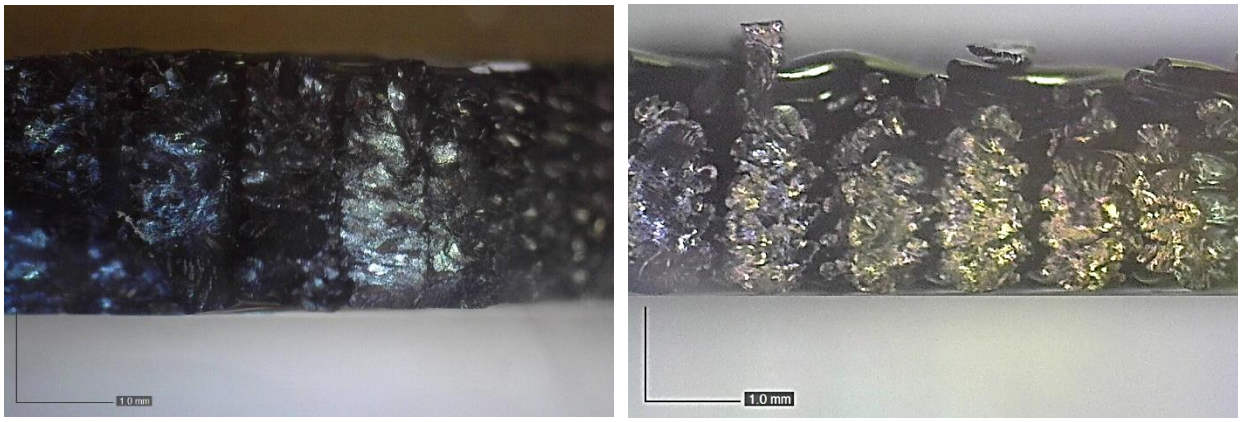

(a) **(b)**

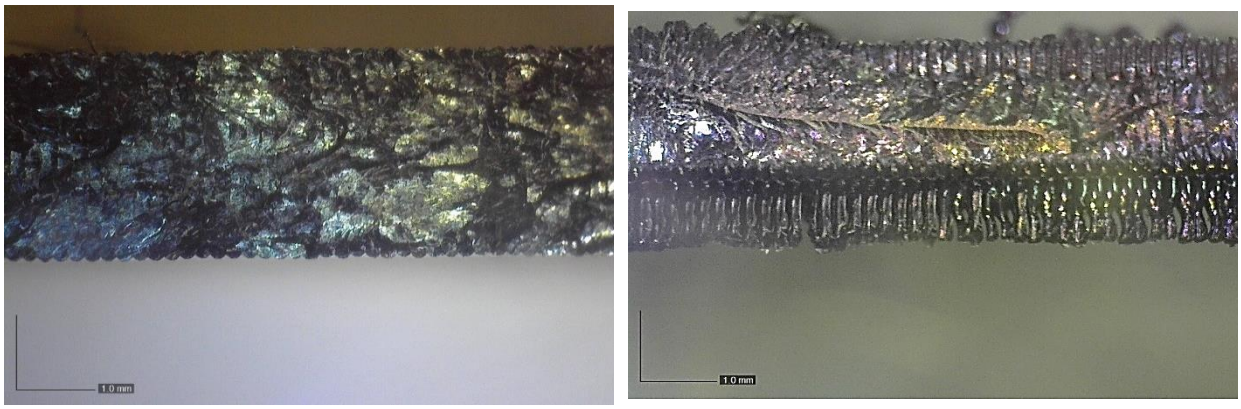

(c) **(d)**

Fig. 4.5. The fracture surface of (a) ASTM D638 specimen in the flat orientation, (b) ASTM D3039 90° in the flat orientation, (c) ASTM D638 specimen in the on-edge orientation, and (d) ASTM D3039 90° in the on-edge orientation.

4.1.2. Numerical results

The specimens were manufactured in the on-edge orientation, where print layers align vertically with the principal loading direction. This orientation was selected as it has been shown to enhance tensile strength and stiffness compared to upright (Z-axis) builds, due to better filament alignment and interlayer bonding.

To ensure the validity of mechanical properties testing, the geometry of the testing specimen must not influence its actual mechanical properties. The presence of any stress risers can introduce artificial stress concentrations, leading to inaccurate experimental results. In structural analysis, the stress-strain behavior of a material can be represented using either linear or nonlinear curves. In linear analysis, the material's stress-strain curve is assumed to be linear, while nonlinear analysis involves implementing a digital representation of the true material stress-strain curve. In this research, linear and nonlinear modeling methods were employed to evaluate the ability of linear models to accurately capture physical phenomena. A Young's modulus of 5250 MPa was considered for the linear models. The nonlinear models incorporated additional material properties such as a yield strength of 70 MPa and a tangent modulus of 10 MPa. Table 4.3 presents the maximum Von Mises stress for each specimen and the shape-specific stress-increasing effects using a stress value of 70 MPa in the boundary conditions.

Table 4.3. Von Mises stress values of different tensile geometry specimens.

Specimen	Linear Model		Nonlinear Model	
	Maximum Stress (MPa)	Multiplier factor %	Maximum Stress (MPa)	Multiplier factor %
ASTM D638	115.64	39.47	89.17	21.50
ASTM D3039-0°	149.11	53.05	77.18	9.30
ASTM D3039-15°	77.27	9.41	71.51	2.11
ASTM D3039-90°	337.1	79.23	71.33	1.86
ISO 527-2	77.18	9.30	71.32	1.85

The results presented in Table 4.3 provide valuable insights into the behavior of the tested specimens. It is evident that the linear stress-strain model tends to overestimate the equivalent stress, while the nonlinear model yields values that are closer to the stress values used in the simulation settings. This discrepancy highlights the importance of using an accurate representation of the material's stress-strain curve for reliable simulations.

4.1.3. Summary and conclusions on the different tensile geometry shapes

In this chapter (4.1) the tensile behaviour of different geometry shapes printed with neat PETG by FDM. Five different geometries were examined for uniaxial tensile studies, utilizing various building orientations (flat and on-edge). The primary aim was to identify the optimal geometry for tensile testing of FDM parts and compare the mechanical performance of different specimen shapes. Additionally, numerical simulations using the finite element method were conducted to identify stress risers in each specimen's geometry. Based on the observations of the obtained results, the consequent conclusions can be drawn:

- Our analysis suggests that rectangular samples with straight edges, such as those conforming to ASTM D3039, exhibit more favorable mechanical characteristics compared to dumbbell-shaped samples with curved edges (ASTM D638 & ISO 527). Experimental data indicate that using ASTM D3039 rectangular specimens with straight edges reduces stress concentration-induced failures and abrupt transition zones. It is important to note that conflicting results for different geometry shapes may arise due to factors such as feedstock material type, printer configuration, printing parameters, and test procedures.
- Effect of print orientation: The on-edge building orientation specimens demonstrated the best tensile properties, surpassing the flat orientation by 39.4%. This improvement can be attributed to the robust inner structure achieved with the on-edge orientation.
- Numerical analysis of stress concentration: The finite element simulations revealed significant stress concentration in the transition area near the gripping location for specimen types ASTM D638 and ASTM D3039. In contrast, the ISO 527-2 specimens exhibited minimal stress raisers near the gripping area, with higher stresses concentrated in the narrow/gauge section away from the clamping location.

4.2 3D-Printed carbon Fiber-reinforced polymer composites and pure polymers

The investigation aimed to enhance stiffness and strength through various parameters, as highlighted in the literature. Tensile and compressive property graphs were constructed by averaging the values from three replicate samples for each condition.

4.2.1 Tensile properties

Figure 4.6 portrays the tensile force-elongation curves for the four materials across distinct building orientations. Notably, the 3D printing building orientation and the material composition distinctly influenced the force-elongation profiles. The results were segregated into two curves based on the building orientation, each delineating the material's behavior concerning the orientation. Discrepancies among the materials may be attributed to distinct material properties and the interlayer adhesion generated during FDM-based specimen construction.

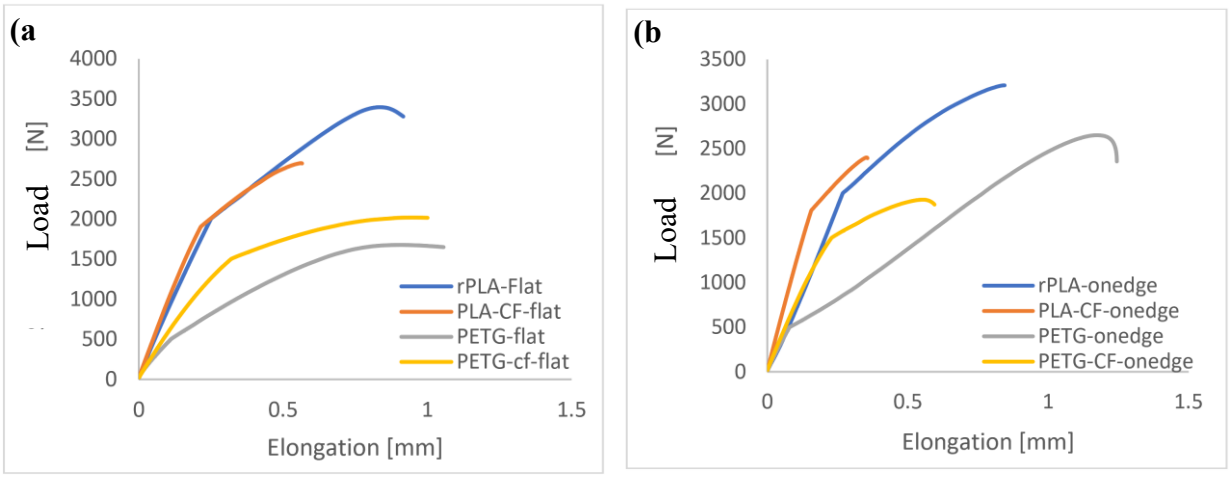

Fig. 4.6 Load-elongation curves for: (a) flat build orientation, (b) on-edge orientation

The rPLA exhibited a maximum force load of 3393 N and 3202 N for flat and on-edge orientations, respectively, surpassing the carbon fiber reinforced PLA. Moreover, PETG and CFPETG exhibited differential responses based on orientation. In the flat orientation, CFPETG demonstrated superior force load due to aligned fibers, displaying 20% higher force than PETG. Conversely, in the on-edge orientation, CFPETG recorded 37% lower force than PETG.

Figure 4.7 summarizes the average tensile test results. In terms of tensile strength, rPLA outperformed other materials with both building orientations. Specifically, rPLA exceeded CFPLA, PETG, and CFPETG by 30%, 100%, and 65.7% for flat orientation, and by 39.2%, 21%, and 77.6% for on-edge orientation, respectively. For tensile modulus, CFPLA displayed superior values for both orientations, indicating lower elasticity in rPLA compared to CFPLA. The comparison between CFPLA and CFPETG revealed CFPLA's tensile strength to be 26.6% and 27.6% higher for flat and on-edge orientations, respectively. Concerning tensile modulus, CFPLA exceeded CFPETG twofold for flat orientation and threefold for on-edge orientation, aligning with the results reported by (Rangisetty & Peel, 2017).

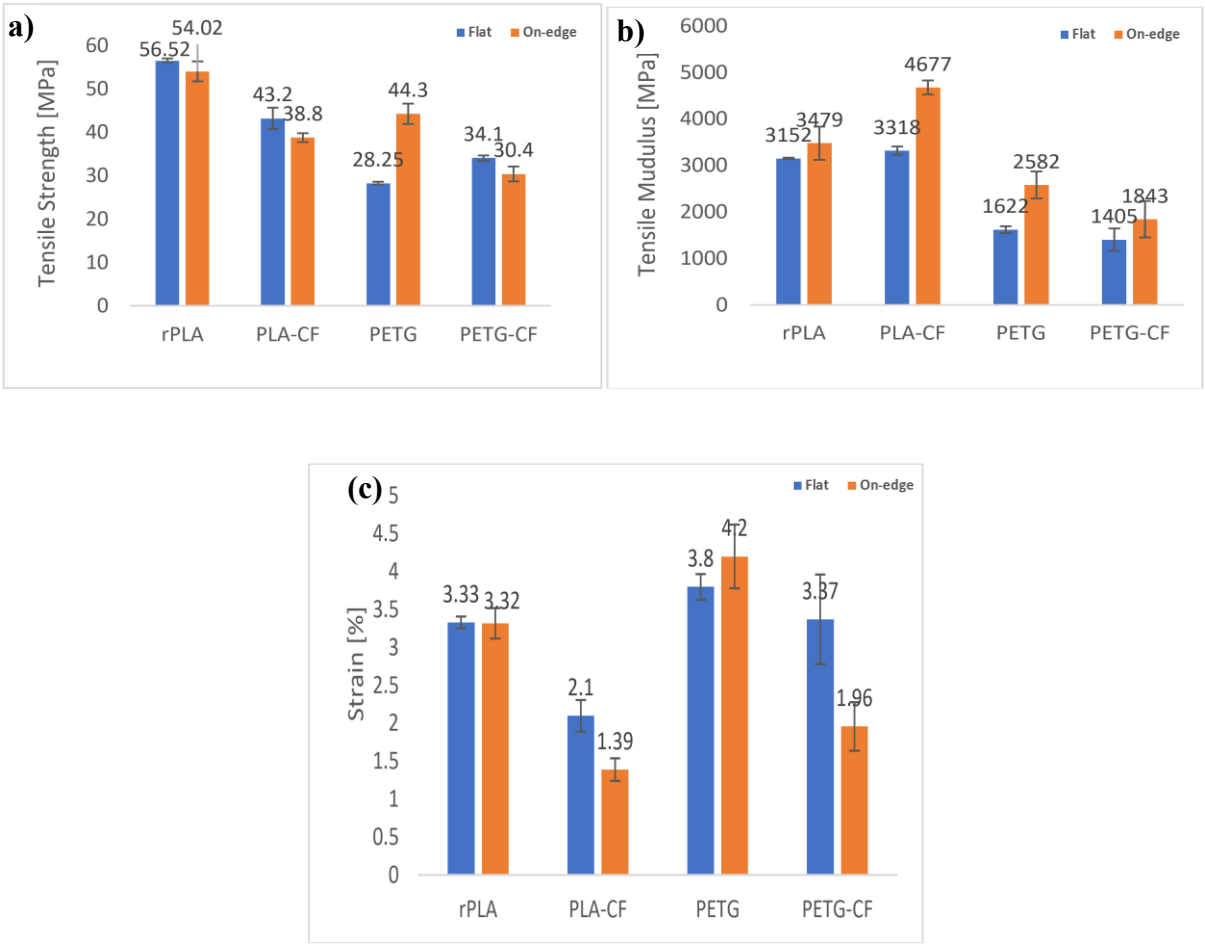

Fig. 4.7 Tensile test results (a) tensile strength, (b) Modulus strength, (c) strain

Principal failure scenarios during tensile tests are depicted in Figure 4.8. The fracture location differed across loading points, with better performance observed in flat orientation specimens.

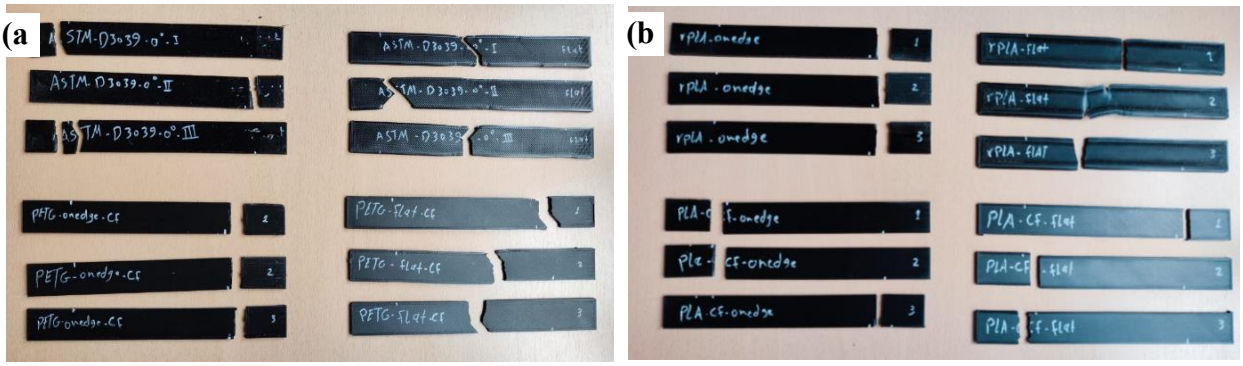

Fig. 4.8 Samples after tensile tests (a) PETG and CFPETG, (b) rPLA and CFPLA with different print orientations

Several studies have reported that short-fiber reinforcements in FDM parts often reduce ductility and may even lower tensile strength compared to neat polymers. This is commonly attributed to poor fiber–matrix adhesion, increased porosity, and fibers acting as stress concentrators when not aligned with the loading direction. Such factors help explain why rPLA outperformed CFPLA and CFPETG in tensile strength, particularly in the on-edge orientation where fiber alignment with the tensile axis is less favorable. In these cases, fibers may act more as inert fillers than true reinforcements, especially when discontinuous and randomly distributed. The reduction in elongation at break is consistent with the increased brittleness reported in literature when fibers hinder polymer chain mobility.

For PETG, natural specimens showed a pronounced orientation effect, with higher tensile strength in the on-edge orientation due to better filament alignment and reduced reliance on interlayer bonding. In contrast, short-fiber reinforcement minimized these orientation-dependent differences by enhancing stress transfer and interlayer adhesion, thereby reducing the anisotropy typically observed in FDM-printed materials.

4.2.2 Compressive properties

Figure 4.9 illustrates the compressive force-elongation curves for the four materials across three specimens. Notably, rPLA and CFPLA displayed the highest and near-highest force loads at 10880 N and 10416 N, respectively. Conversely, CFPETG samples exhibited the lowest compressive force among the materials. Table 4.4 provides average compressive results for all tested materials. Figure 4.10 showcases average maximum compressive stress, Young's modulus, and maximum compressive strain. rPLA demonstrated a maximum compressive stress of 82.3 MPa, surpassing CFPLA by 23.7%. PETG's compressive strength (53.7 MPa) aligned with reported literature values, ranging from 41 to 98 MPa (Amza et al., 2021). PETG and CFPETG exhibited lower compressive deformation, while rPLA demonstrated the largest maximum deformation, in accordance with (Hsueh et al., 2021). The latter found that PLA's mechanical properties surpassed those of PETG, except for thermal deformation.

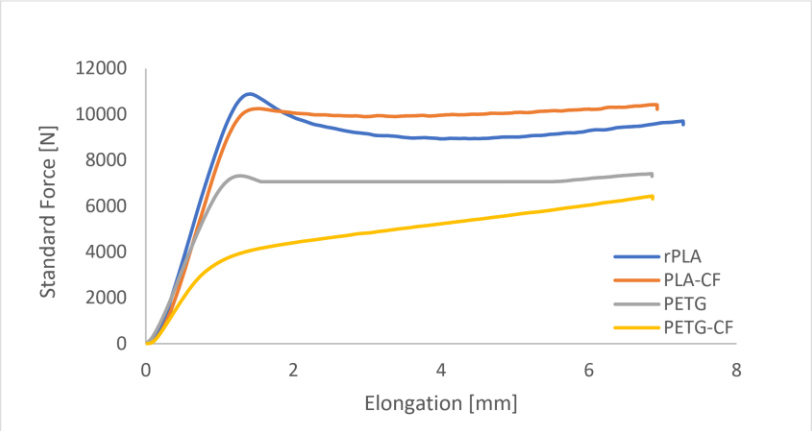

Fig. 4.9 Force-elongation curves for compressive tests

Table 4.4 The compressive properties for the materials examined

Compressive Properties	rPLA	CFPLA	PETG	CFPETG
Compressive strength (MPa)	82.3	66.5	53.7	49.3
Compressive modulus (MPa)	358.1	290.4	241.8	221.8
Compressive strain (%)	2.30	2.29	2.23	2.22

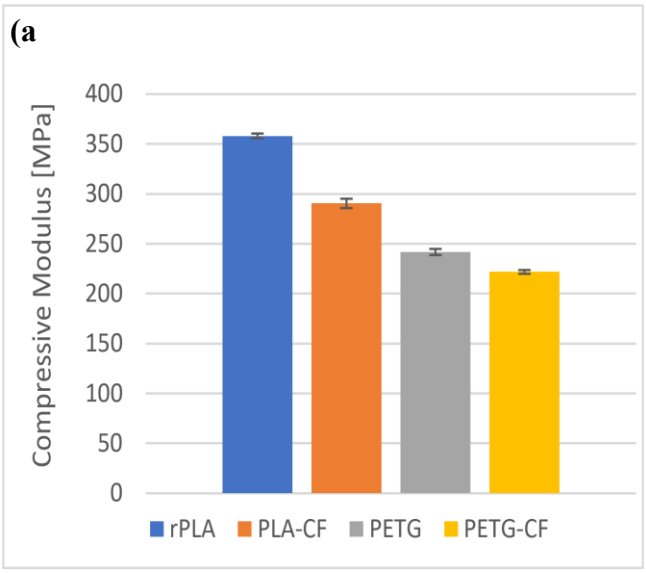

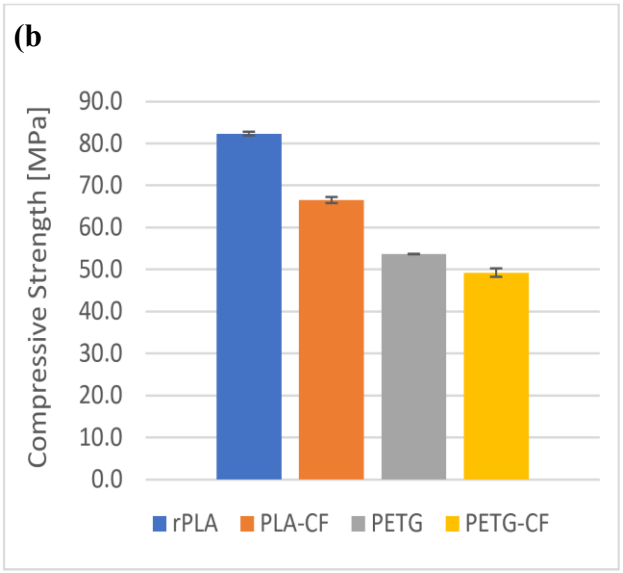

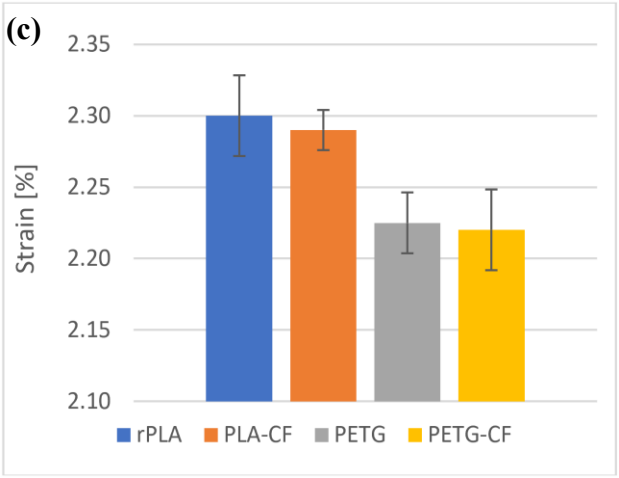

Fig. 4.10 Compressive properties (a) compressive strength, (b) compressive modulus, (c) compressive strain

Figure 4.11 highlights pre- and post-compressive test samples for the four materials. Notably, samples reinforced with carbon fibers, such as rPLA and PETG, exhibited significantly enhanced compressive resistance. The compressive deformation occurred primarily around the pressure application point. Notably, fiber-reinforced samples displayed pressure distribution toward the center, contributing to greater resistance against pressure force in CFPETG and CFPLA samples, compared to rPLA and pure PETG samples.

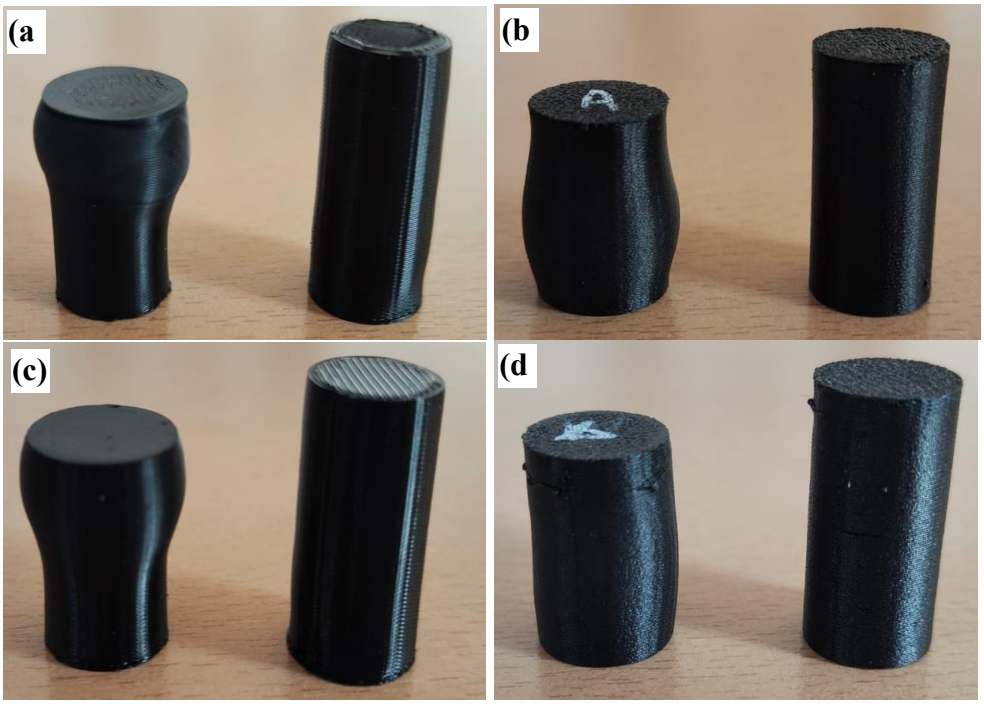

Fig. 4.11 Compressive samples after testing (a) rPLA, (b) CFPLA, (c) PETG, (d) CFPETG

4.2.3 Interface characterization

The impact of incorporating fibers on tensile strength was further explored using an Axio Lab A1 Microscope to scrutinize the interfacial fusion of the diverse materials. The analysis revealed the dispersion of carbon fibers within PLA and PETG filaments, with noticeable carbon fiber agglomeration in the cross-section of CF-PLA and CF-PETG filaments. Optical microscope images of the fractured surfaces of rPLA, PETG, CF-PLA, and CF-PETG specimens are presented in Figure 4.12. The fracture surfaces of rPLA and PETG (Fig. 4.12a and b) appear relatively smooth and uniform, consistent with brittle failure and limited internal heterogeneity. In contrast, the CF-PLA and CF-PETG specimens (Fig. 4.12c and d) exhibit rougher fracture surfaces, with evident signs of short carbon fiber dispersion in various orientations. The presence of micro-voids, fiber pull-out, and occasional fiber breakage is observable, indicating that the addition of carbon fibers introduced localized inhomogeneities. Furthermore, small gaps between the carbon fibers and the surrounding polymer matrix suggest weak interfacial adhesion, which likely contributes to the observed reduction in ductility and tensile strength, particularly in edge-printed configurations. The clustering of fibers and void formation may also exacerbate stress concentration effects, leading to premature failure.

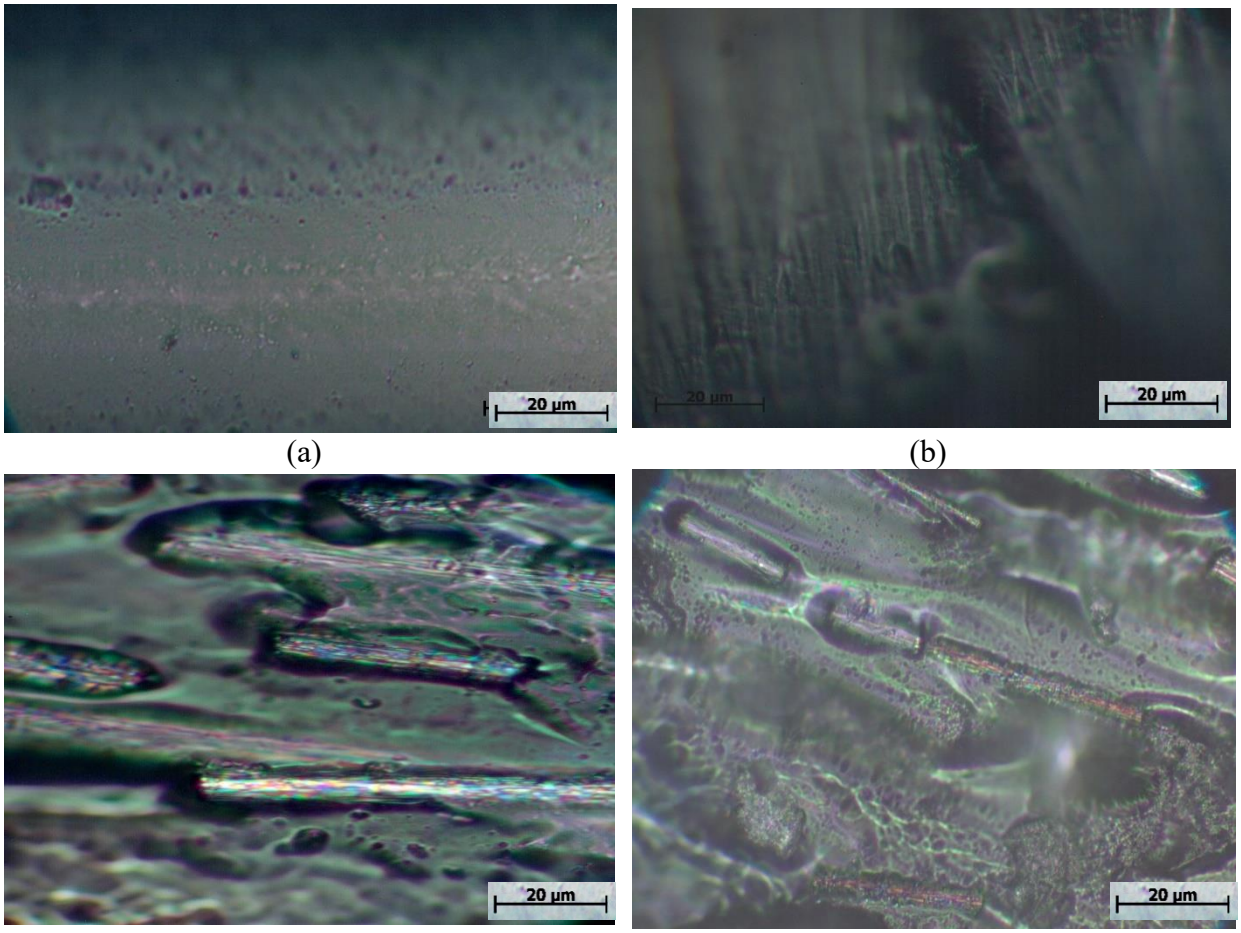

(a) (b)

(c) (d)

Fig 4.12: Optical microscope picture of: (a) rPLA, (b) PETG, (c) CF-PLA, (d) CF-PETG

4.2.4 Summary and conclusions on 3d-printed pure and composite polymer

The present chapter (4.2) investigated the compressive and tensile characteristics of FDM-fabricated rPLA, 10% carbon fiber-reinforced PLA, PETG, and carbon fiber-reinforced PETG, focusing on the effects of various build orientations. The ultimate tensile strength (UTS), Young's modulus, elongation at UTS, and elongation at break were evaluated in line with the observed behavior from the tested print settings. Based on the results, the following conclusions can be made:

- rPLA and 10% carbon fiber-reinforced PLA consistently outperformed PETG and 10% carbon fiber-reinforced PETG in both tensile and compressive tests, across Young's modulus and strength assessments.
- All four materials exhibited distinct tensile and compression asymmetry, with compressive stress surpassing tensile stress.
- rPLA exhibited stronger overall mechanical performance than the fiber-reinforced alternatives. Under tensile loading, it outperformed CFPLA, PETG, and CFPETG by 30%, 100%, and 65.7% respectively in flat orientation. A similar pattern was observed in the on-edge orientation, where rPLA showed gains of 39.2%, 21%, and 77.6% over the same materials.
- In the realm of compressive strength assessment, the findings indicate that rPLA exceeded CFPLA, PETG, and CF-PETG by margins of 23.7%, 53%, and 67%, respectively.

Overall, the mechanical properties analysis revealed that the On-edge print orientation demonstrated the highest tensile strength, attributed to its strong internal structure. Additionally, rPLA exhibited superior compressive properties compared to the other materials.

4.3 Re-manufactured filaments

4.3.1 Original filament tensile test

Tensile testing was conducted on the original filament material, which had not undergone extrusion during the printing process. Figure 4.13 presents the stress-strain curves for the five different filament materials. The figure provides one representative result out of the three tests conducted for each material.

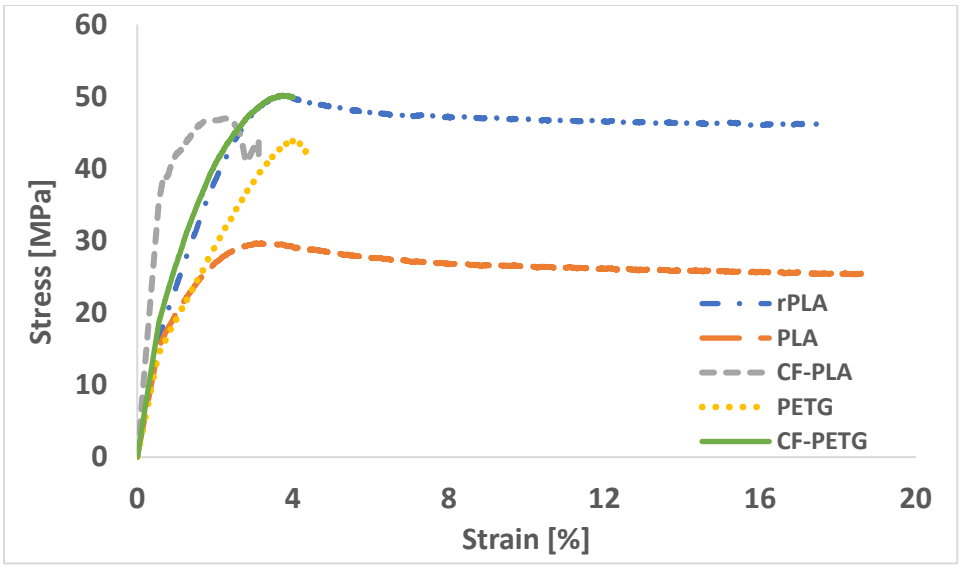

Fig 4.13. Stress-strain curves for the original (non-printed) materials.

The CF-PETG filament exhibited a maximum stress of 50.14 MPa, closely matching the stress of rPLA filaments. The stress of CF-PETG was higher than that of rPLA, PLA, CF-PLA, and PETG by 0.2%, 70%, 6.7%, and 14.4%, respectively. The CF-PETG filament demonstrated consistent stress resistance throughout the specified strain range. In contrast, the other filaments experienced a reduction in stress resistance after reaching their respective peak stress levels. Compared to the tensile strength values provided by the manufacturer, the tensile strength of PLA, rPLA, PETG, and CF-PLA decreased by 30%, 20%, 28%, and 27%, respectively. This reduction can be attributed to several factors, including variations in environmental conditions (such as humidity and temperature), differences in testing equipment or setup (e.g., grip type, alignment, or loading speed), and the storage conditions of the filament prior to testing (see Table 3.3 for manufacturer data). This outcome is consistent with previous studies, as datasheets typically report results from injection-molded or conditioned specimens rather than raw extruded filaments. Environmental exposure, storage history, and extrusion variability are known to reduce filament strength (Ning et al., 2015; Tymrak et al., 2014). Since all filaments were tested under identical conditions in this study, the comparative trends observed remain reliable and scientifically relevant.

4.3.2 Re-manufactured filament tensile test

Tensile tests were conducted on re-manufactured filaments, encompassing a set of five specimens: rPLA, PLA, CF-PLA, PETG, and hemp fiber-reinforced PLA/rPLA filaments. Additionally, jute fiber-reinforced PETG underwent re-manufacturing and testing in this segment. Notably, the re-manufactured PLA and rPLA exhibited superior tensile strength compared to the original filaments, which can be attributed to the consistent layer bonding in the PLA samples. However, the recycled CF-PLA showed a 4% reduction in strength compared to the original filaments. This decrease in tensile strength is likely due to the formation of fiber clusters during recycling, weakening the adhesive bond between the PETG and carbon matrix, as observed in the zoomed-in areas in Figure 4.14. The clusters reduce the mechanical properties of the composite by impairing interlayer adhesion. Regarding PETG filament, the recycled PETG exhibited lower strength than the original filaments. On the contrary, incorporating 7 wt% hemp fiber into PLA

and rPLA filaments and re-manufacturing them resulted in filaments with superior tensile strength compared to the original ones. In the case of white PLA with hemp filaments, the tensile strength surpassed that of the original filaments and pure recycled PLA by 29% and 26%, respectively. Furthermore, adding 7 wt% hemp fiber to rPLA increased its tensile strength by 7% compared to the original rPLA filament, though it resulted in a 6% decrease in tensile strength compared to re-rPLA. Moreover, adding 7 wt% jute fiber to PETG enhanced the tensile strength by 12% and 15% for the original and re-manufactured PETG filaments, respectively. Figure 4.14 shows the sample after the test. Additionally, a comparison between the maximum applied load and ultimate tensile strength (UTS) for both the original and re-manufactured filaments is shown in Table 4.5.

Table 4.5 Maximum applied load and tensile strength, values for the original, re-manufactured, and reinforced filaments.

Filaments	**$F_{original\ filament}$** [N]	**$F_{re\text{-}filament}$** [N]	**$UTS_{re\text{-}filament}$** [MPa]	**$UTS_{original\ filament}$** [MPa]
re-PLA	71.51 ±2.7	18 ±1.2	30.6 ±1.8	29.7 ±3.2
re-rPLA	120 ±4.8	50 ±1.7	58.6 ±2.5	50 ±3.7
re-PETG	105 ±2.5	72 ±3.1	42.43 ±2.3	43.86 ±2.6
re-CFPLA	113 ±3.4	66.8 ±2.6	42.4 ±3.1	47 ±3.6
re-PLA+Hemp	-	18 ±1.1	38.5 ±0.9	-
re-rPLA+Hemp	-	50 ±2.8	53.5 ±2.7	-
re-PETG+Jute	-	62.38 ±3.2	49 ±3.3	-

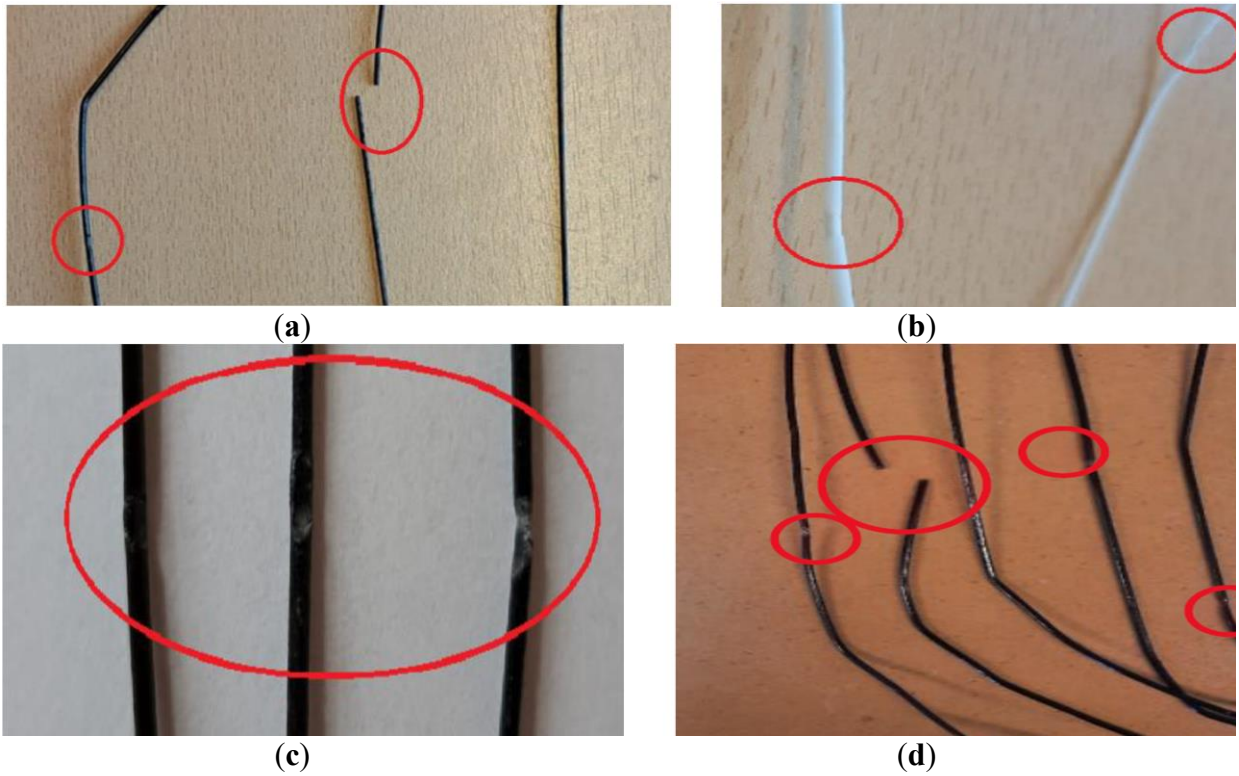

(**a**) (**b**)

(**c**) (**d**)

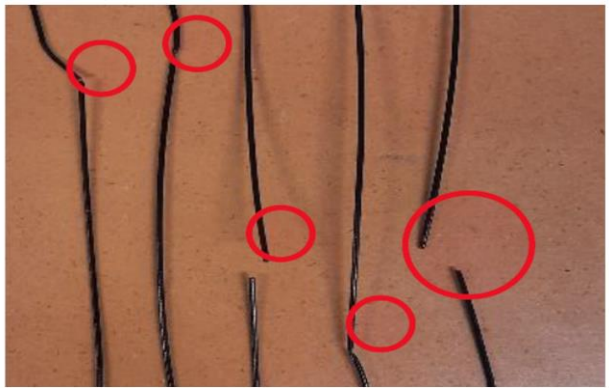

(e)

Fig 4.14. Fractured surfaces of re-manufactured filament samples: (a) re-rPLA, (b) re-PLA, (c) re-PLA+ Hemp fiber, (d) re-PETG, and (e) re-PETG + Jute fiber.

4.3.3 Summary and conclusions on filaments tensile properties

This study presents a comprehensive assessment of the mechanical properties of various filaments, with a focus on reinforcement techniques and processing methods. Rigorous tensile testing provided critical insights into the materials' mechanical performance. The key findings are as follows:

- Among the original filaments, CF-PETG exhibited the highest maximum stress at 50.14 MPa, outperforming rPLA, PLA, CF-PLA, and PETG.
- Recycled filaments showed mixed results. Both CF-PLA and recycled PLA (rPLA) demonstrated increased tensile strengths compared to their original forms, with rPLA achieving a 29% improvement when reinforced with hemp fiber. However, recycled CF-PLA experienced a marginal 4% reduction in strength.
- Re-manufactured PETG exhibited lower tensile strength than the original material. However, the incorporation of jute fiber improved the tensile strength of both recycled and original PETG by 15% and 12%, respectively

4.4 Sandwich Structures

4.4.1 PLA with honeycomb/rhombus core structures

4.4.1.1 Tensile performance of sandwich structures

Figure 4.15a shows the load-displacement curves that were obtained from the tensile test of the honeycomb and rhombus sandwich structures. Obviously, the rhombus core sandwich samples had the greatest maximum load of 714 N in the load-elongation curves. In terms of the tensile strength, which ranged between 19.49 and 23.01 MPa, the better values were from rhombus core sandwich structures (see Figure 4.15b). The increased tensile strength of these specimens is due to their reliable core structure, which had more contact sites at the fracture area under tensile stress than the honeycomb core construction (see Figure 4.15). Therefore, the applied load was distributed across a larger area, resulting in higher resistance to failure. In contrast, honeycomb sandwich structures had the best tensile Young's modulus of 599 MPa compared to rhombus (440 MPa), as shown in Figure 4.20c. (Zaharia et al., 2020) have studied the mechanical properties of different sandwich structures (honeycomb, diamond-celled (resembles the rhombus in the current work), and corrugated). They reported a higher load (required to fracture) and tensile strength for the

diamond structure than the honeycomb, which is in good agreement with the present study findings.

Figure 4.16 shows that sandwich specimens seem to be failed first due to the yielding of the first outer surface (shell), and thereafter the core (inner structure) shear failure. The first outer surface of the sandwich specimens yielded, the fracture progressed through the whole core, and finally terminated at the lower level, causing cracking of the second outer surface(shell). The specimens, as shown in Figures 16a and 16b, had a complete fracture of the whole structure, beginning with the first surface (shell), then the core, and lastly the second surface, for both (honeycomb and rhombus) tested sandwich structures.

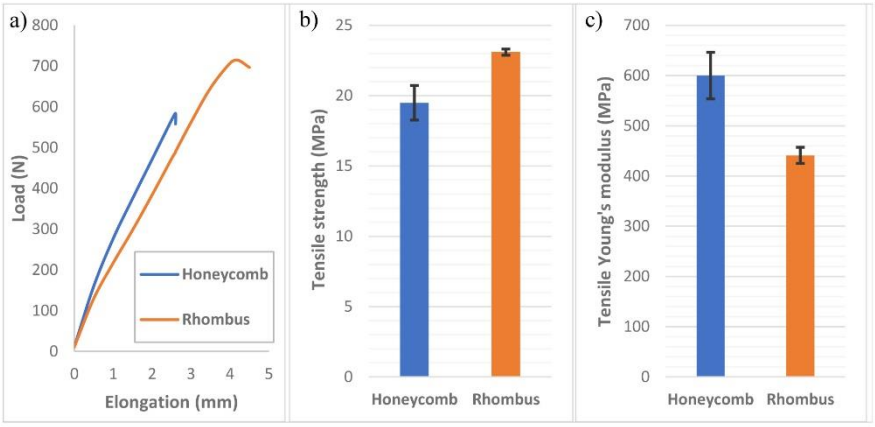

Figure 4.15 Tensile test result of sandwiches structure specimens, a) load-displacement curves, b) tensile strength values, and c) Young's modulus values

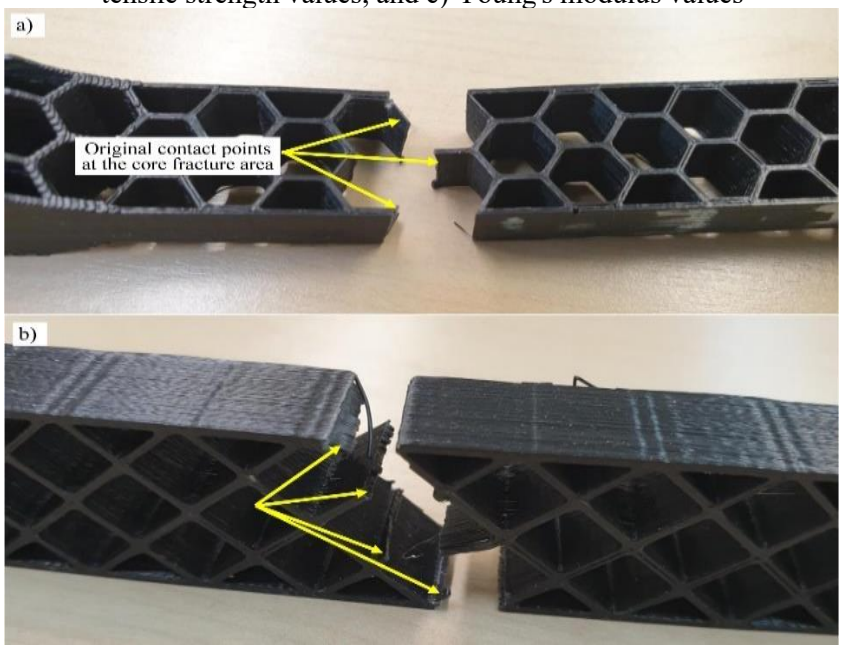

Fig. 4.16 Fracture shape and contact sites at the core structure failure area after the tensile tests of a) honeycomb, and b) rhombus sandwich specimens

4.4.1.2 Three-Point bending performance of sandwich specimens

The flexural performance of the lightweight sandwich constructions (honeycomb and rhombus), including bending strength, bending modulus, and stress-displacement characteristics, was

investigated using this test approach. The load-displacement curves of test specimens for three-point bending have two main stages, as shown in Figure 4.17a: a steady increase between the load applied and the displacement towards the curve's maximum, but then when the specimens broke, there was a sudden decline from the maximum load. (Sugiyama et al., 2018) attributed this non-linearity or sharp decline exhibited in the load curve to the gradual failure progression. They mentioned that in the fracture mode, the crack initially happens at the upper skin while wrinkling occurs at the core, causing the curve to drop. Using Equations (3-9, 3-10) and the sandwich specimen dimensions, the test machine software automatically determined the bending modulus and bending strength, which are the most essential three-point bending aspects.

Three-point bending results were better for the rhombus compartive with honeycomb core sandwich structure. The maximum force reported was about 381 N at a displacement of 4.47 mm of rhombus core specimens, according to the curves shown. In terms of the bending strength, Figure 4.17b exhibits that the rhombus core sandwich models had a bending strength average value of 40% higher than that of the honeycomb core sandwich samples. Furthermore, the bending Young's modulus of rhombus specimens was twice as high as that of honeycomb specimens (see Figure 4.17c).

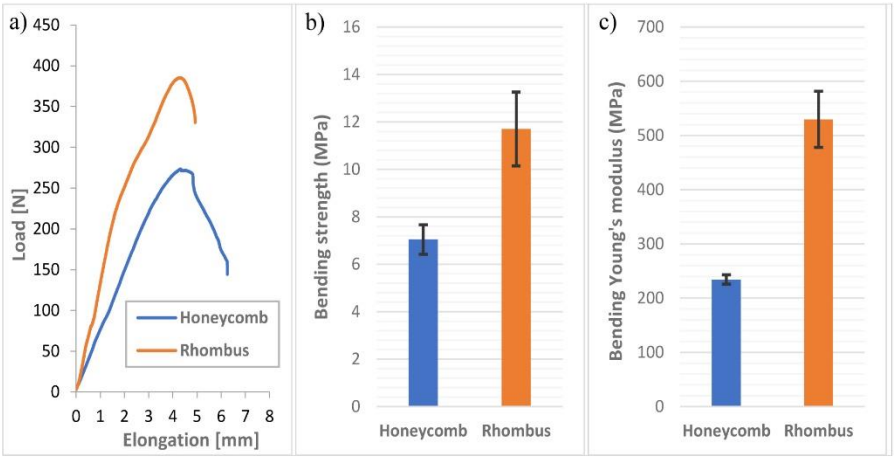

Figure 4.17 Three-point bending test results of sandwich structures, a) load-displacement curves, b) bending strength, c) Young's modulus of bending

The primary failure scenarios of sandwich structures that occurred during three-point bending tests are shown in Figure 4.18. The fracture point pictured in Figure. 4.18a was not at the same loading point while testing. This is due to, at the fracture site, the core being at an angle perpendicular to the longitudinal axis, making fracture/buckling easy (Sugiyama et al., 2018). Sandwich specimens with thin skins may readily fail in a skin yield mode because rhombus core sandwich faces/skins practically withstand all tensile and compressive loads in bending (Zaharia et al., 2020). However, an indentation mode occurs initially when the core sandwich walls are thick enough, but given sufficient impact energy, the sandwich structures will eventually collapse in a skin-yield fracture mode on the top face (Yu et al., 2008). Then, cracks are formed in the rhombus core, followed by propagation of the failure up to the lower face. On the other hand, the bending test results of the honeycomb core structure specimen showed that a tension failure in the upper skin takes place like compression face buckling/wrinkling (see Figure 4.18b). Local short-wavelength wrinkling of skins is another name for this sort of failure mechanism (Samali et al., 2019). The rhombus specimen had a rib under the tool, while the honeycomb had an empty cell in that area. This

variation leads to differences in local stiffness and is likely to influence the failure modes, as supported by prior studies on core geometry effects.

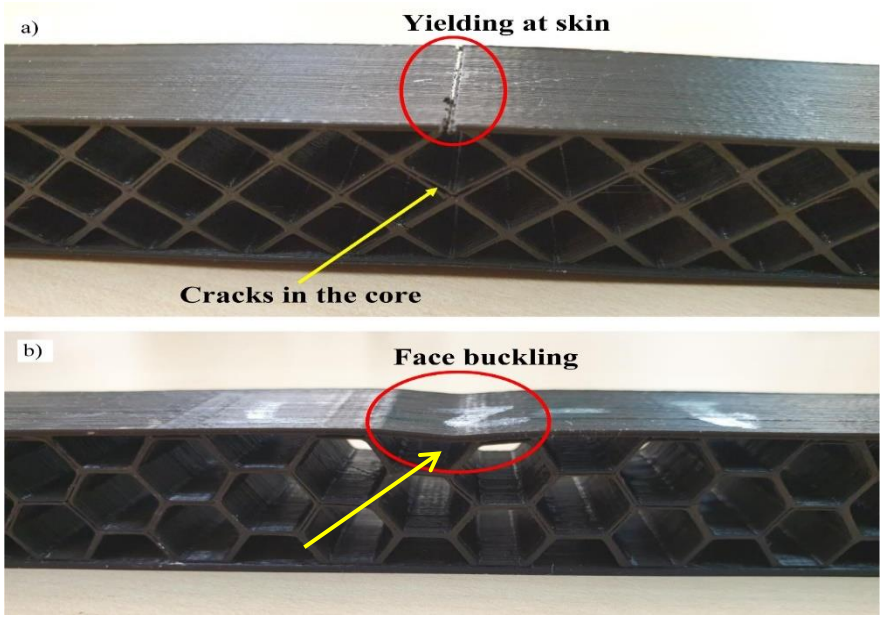

Fig 4.18 Three-point bending test's failure modes of sandwich specimens; a) rhombus, and b) honeycomb core structures

4.4.1.3 Compression behaviour of sandwich structures

The present section discusses the compression test results obtained for 3D-printed rhombus and honeycomb structure specimens. Figure 4.19 exhibits the compression behaviour gained from the compression tests for each examined type of sandwich structure. It is evident from Figure 4.19a that the load-displacement responses are generally linear until the core shear starts, at which point there is a dramatic reduction in load. The maximum force (roughly 5850 N) was found in the rhombus core structures (at an elongation of 1.6 mm) until unredeemable damage in this sandwich structure occurred. However, for the honeycomb structure, irreversible damage occurred when the load force reached 2820 N at 1.35 mm elongation.

The results of compressive stress and modulus are presented in Figure 4.19b and Figure 4.19c, respectively. Again, the rhombus core sandwich structure offered the best performance as the average of its compressive strength (70 MPa) was 35.4% higher than that of the honeycomb (45.8 MPa) and its compressive modulus (891.015 MPa) was 15.54 % better than the honeycomb (752.513 MPa). The dense network of its structures, which also caused these specimens to weigh more, is responsible for the outstanding performance of rhombus core specimens.

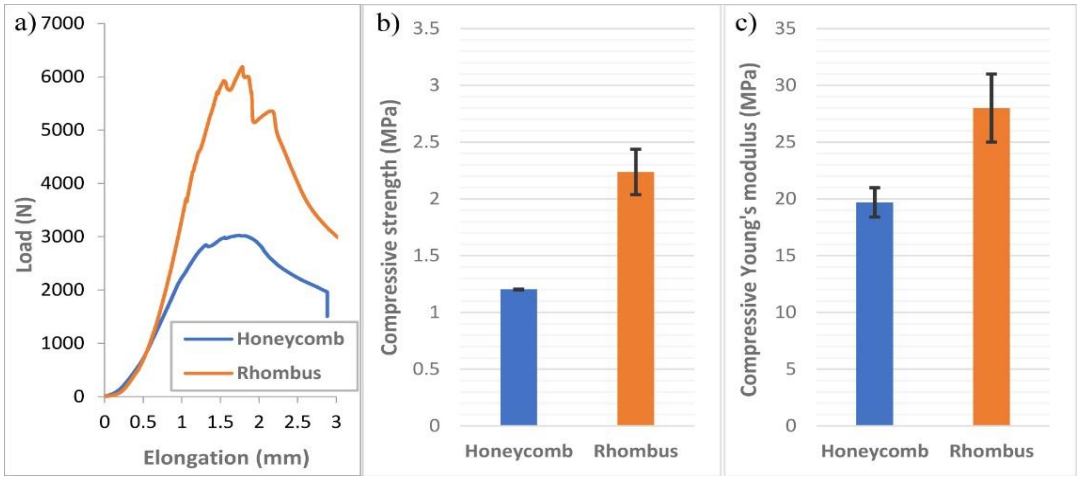

Fig 4.19 Compression test results, a) load-elongation curves, b) compressive strength, and c) Young's modulus of compression

Figure 4.20 shows the specimens after the compression. For the honeycomb specimen (Figure 4.20a), deformations developed in the structure's core as the breakdown was the shearing of the core of the sandwich. This may be explained by the fact that when sandwich structures are compressed, the skins are too thick and robust to be crushed, resulting in a core shear mode. However, in the case of the rhombus structure (Figure 4.20b), the extruded filament layers were debonded and buckled because the sandwich's core had a high degree of flexibility.

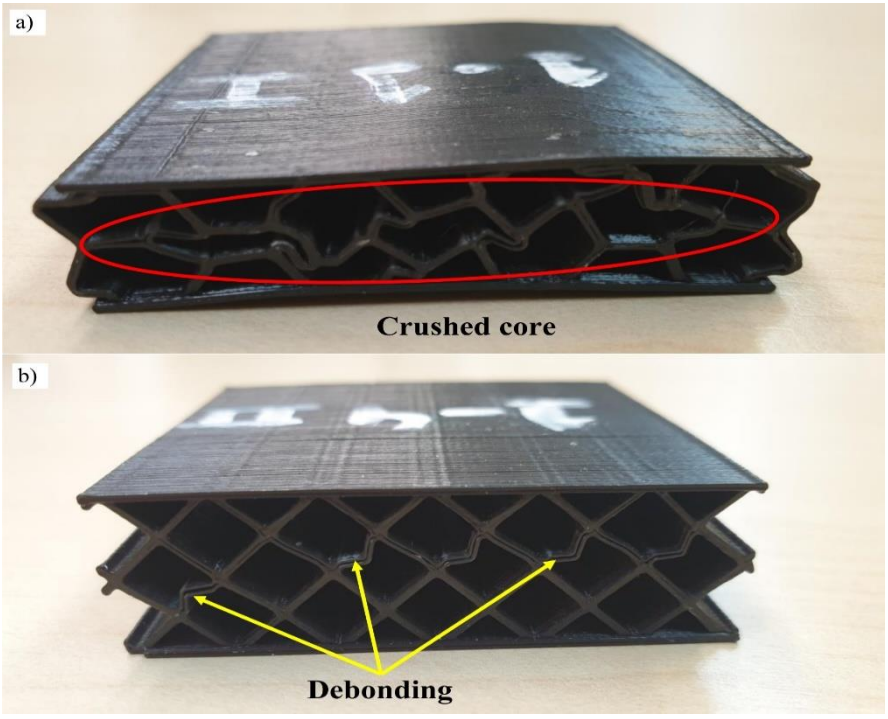

Fig 4.20. Failures mode of the sandwich specimens after the compression, a) core shearing for the honeycomb sandwich structure, and b) debonding of the extruded filament layers for the rhombus specimens

4.4.1.4 Summary and conclusions on PLA printed with honeycomb/rhombus

In this chapter (4.4.1), two different 3D-printed sandwich structures, honeycomb and rhombus, were manufactured and characterized. Initially, tensile, three-point bending, and compression test specimens were prepared using PLA filament via the fused deposition modeling technique. Subsequently, the properties of the PLA-based sandwich structures were thoroughly investigated through the conducted tests.

- The rhombus sandwich samples demonstrated superior tensile strength, exhibiting a 15.3% increase compared to the honeycomb structure, attributed to their robust core design.
- Additionally, the rhombus specimens achieved maximum compression and flexural strengths, surpassing the honeycomb structure by 35.4% and 39.8%, respectively.

It was noticed that 3D-printed sandwich structural collapse is primarily due to the failure of the core.

4.4.2 Wood/PLA composites with re-entrant honeycomb core

The selection of Wood/PLA filament in this chapter is justified by its improved mechanical properties, natural aesthetic qualities, and environmental sustainability, aligning with the objectives of producing functional and eco-friendly 3D-printed components. Tensile tests were performed to determine Young's modulus of the solid 3D printed material and to assess the mechanical properties of wood/PLA material. The tensile strength of 3D-printed solid material is 29 MPa. Young's modulus was calculated at 2085 MPa from the stress-strain curve.

4.4.2.1 Experimental bending test

Experimental stress-strain curves obtained from the bending tests for all examined re-entrant core orientations (in-plane (vertical, V) and out-of-plane (horizontal, H)) are shown in Figure 4.21a. The samples with in-plane core position and 1.6 mm face layer exhibited the highest stress, reaching 124 MPa. This stress level surpassed that of the in-plane core position with a 0.8 mm face layer by 30% and exceeded the out-of-plane core positions with 1.6 mm and 0.8 mm face layers by 26% and 195%, respectively. Conversely, the lowest stress was observed in the out-of-plane core position with a 0.8 mm face layer.

Figure 4.21b shows the flexural modulus, the specimen with a 1.6 mm face layer thickness and in-plane core position (1.6 V) exhibits the highest E modulus at approximately 374.47 MPa. The out-of-plane core position (H) with a 0.8 mm face layer has an E modulus of about 265 MPa, which is the lowest among all tested configurations. Increasing the face layer thickness to 1.6 mm while maintaining the in-plane core position (1.6 V) results in an increase in E modulus by 31% compared with 0.8V specimens. The out-of-plane core position (H) with a 0.8 mm face layer also shows a lower E modulus than the out-of-plane specimens with 1.6 mm by 24%. It is evident that both the orientation of the core and the thickness of the face layer play crucial roles in determining the flexural properties of wood/PLA materials. It is important to note that the better performance of the in-plane core position is not only due to increased material presence under loading but also due to the unique structural benefits of the re-entrant design. This design optimizes material distribution, which enhances performance in the in-plane direction compared to typical porous structures. The improvement in bending stiffness with a thicker face layer follows the principle of moment of inertia. While this result is expected, experimental confirmation is essential to validate theoretical predictions and optimize the balance between structural weight and mechanical performance.

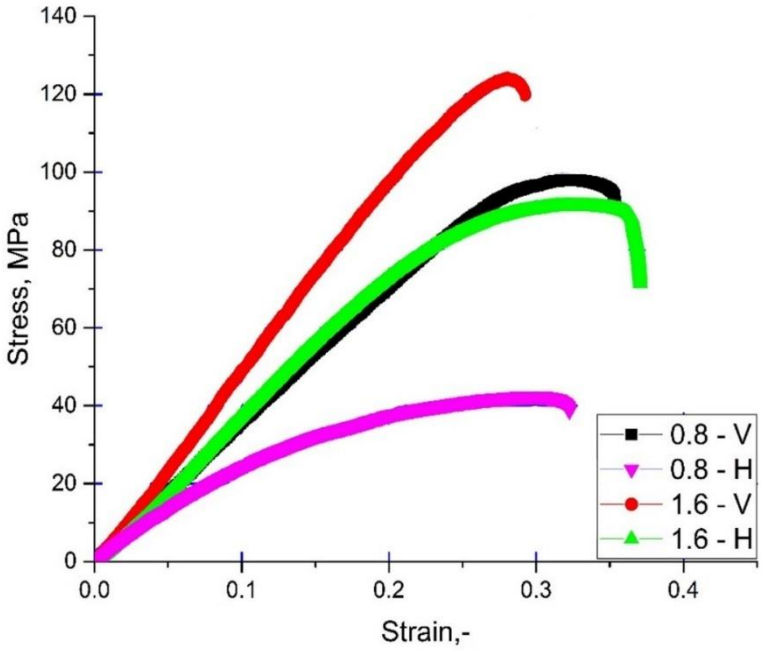

(a)

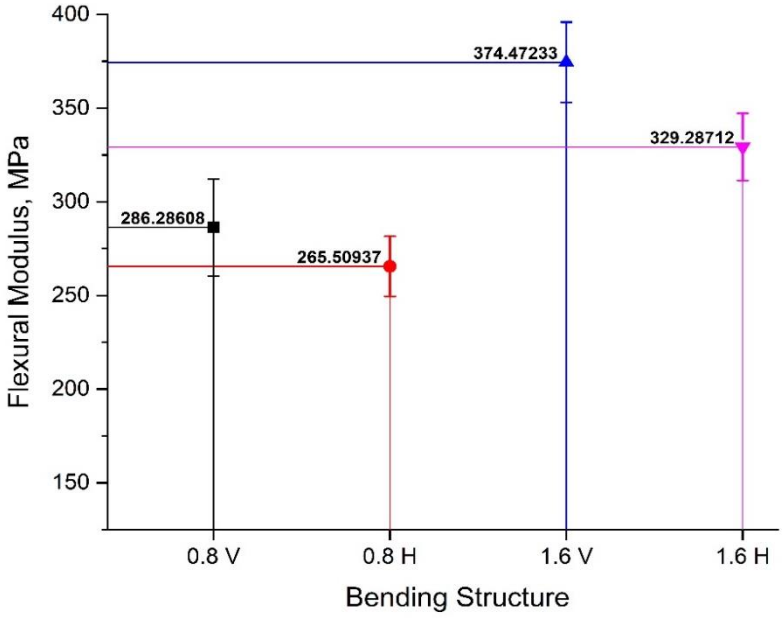

(b)

Fig 4.21. (a) Bending stress-strain curves and (b) flexural modulus of the bending re-entrant honeycomb structure

Examining the failure surfaces can provide insights into the specific failure modes, such as cracks, delamination between layers, or deformation patterns. The appearance of the surfaces can help identify the critical points where failure is initiated. Comparing the failure surfaces of out-of-plane and in-plane specimens allows for an assessment of how the material responds to bending in different orientations.

Certain fracture surfaces of specific specimens subjected to 3-point bending are illustrated in Figure 4.22. When subjected to bending loads, distinct stress distributions emerge: the upper face sheet undergoes compression stress, the core primarily experiences transverse shear, and the lower face sheet encounters tensile stress. Sandwich structures tend to fracture through diverse mechanisms, encompassing debonding, face sheet buckling, and core shearing, as elucidated by (Lu et al., 2018). However, peeling failure on the adhesive surface between the skin and the core, which is common in these conditions (De Castro et al., 2021), was not observed. Figure 8 depicts the typical bending behavior of the sandwich structures. The cracks develop vertically (cross-section) from the bottom to the top of the skin. The lower skin of sandwich structures first experienced tension failure, succeeded by a subsequent compressive failure on the upper skin. The propagation of cracks followed truncated, irregular zigzag trajectories, occasionally punctuated by gaps between the layers. Such behavior aligns with the anticipated conduct of 3D printed materials exhibiting a horizontal ± 45° composition (Ameri et al., 2022; K. Wang et al., 2019). Furthermore, the sandwich structure's upper and bottom layers slightly tended to separate during bending, resulting in a crack pattern that matched the structural arrangement (as depicted in Figure 4.22a and 4.22b). Prior observations have indicated that within 3D-printed components, the crack growth planes delaminate in response to bending loads (Ameri et al., 2021). On the other hand, the bending test results of the in-plane core structure specimens showed more tensile failure in the bottom surface than the out-of-plane core structure takes place, like compression face buckling/wrinkling (see Figure 4.22).

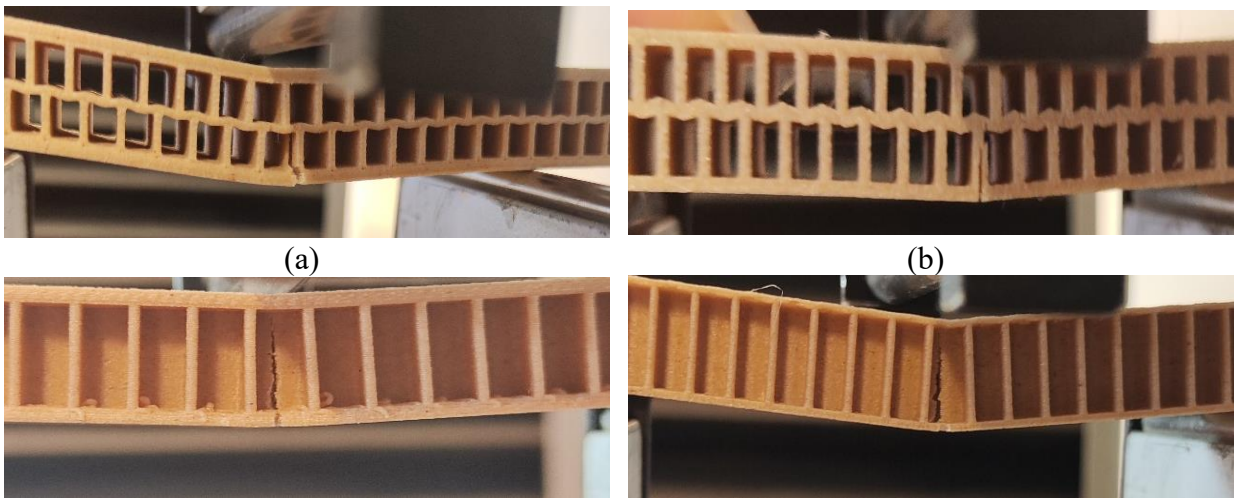

Fig 4.22. The failure mode of 3D-printed specimens after performing bending tests for the structure: (a) out-of-plane with 1.6 mm surface thickness, (b) out-of-plane with 0.8 mm, (c) in-plane with 1.6 mm, (d) in-plane with 0.8 mm

To clarify the relationship between structural strength and weight, the specific strength has been computed, which is associated with the maximum specific stress-to-mass ratio. This computation enables a comparison among all printed specimens and reveals a new characteristic of the examined structures. Figure 4.23 illustrates the specific strength obtained from the bending test. The maximum specific strength was to the in-plane specimens with a 1.6 mm face layer (1.6 V) at 7156 MPa/Kg, and the lowest was to the out-of-plane specimens with 0.8 mm face layer (0.8 H) at 3235 MPa/Kg.

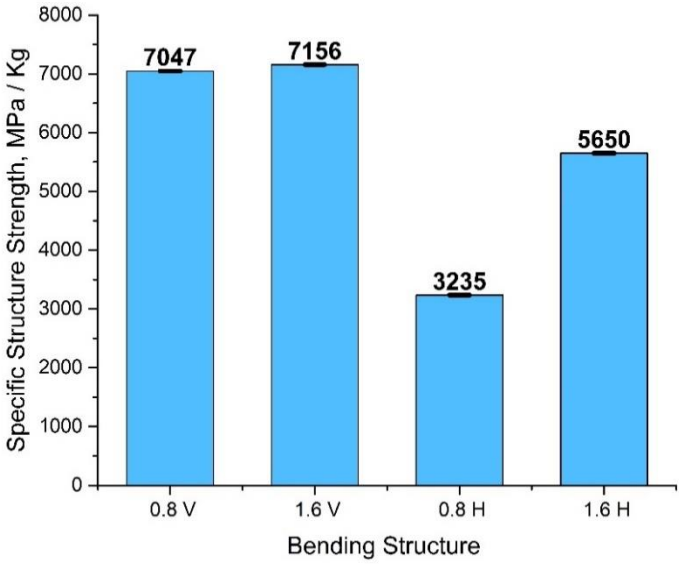

Figure 4.23. The specific strength exhibited from the bending test

4.4.2.2 Experimental compressive Test

Since the areas subjected to compressive stress in the printed specimens are not fully filled with material, the actual cross-sectional areas were calculated using SolidWorks software, as presented in Figure 4.24 and calculated in Table 4.6. Here, A_S is the smallest subjected area and A_L is the largest subjected area.

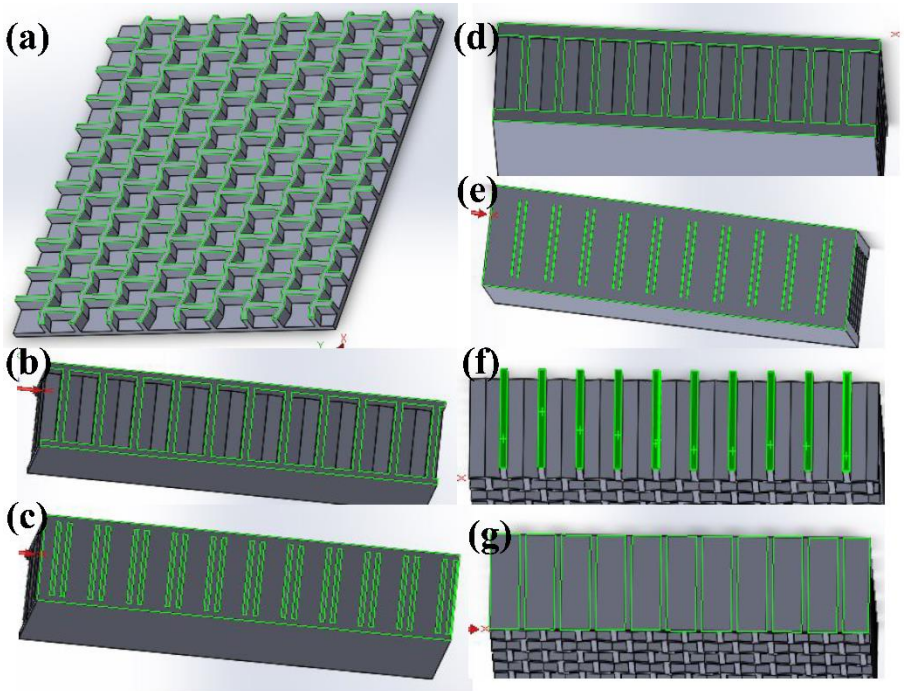

Fig 4.24. Compressive specimens' area of (a) flatwise, (b) A_S of edgewise 0.8 mm face, (c) A_L of edgewise 0.8 mm face, (d) A_S of edgewise 1.6 mm face, (e) A_L of edgewise 1.6 mm face, (f) A_S of edgewise 0 mm face (without face), (g) A_L of edgewise 0 mm face.

Table 4.6. Cross-sectional areas corresponding to various compressive positions, as shown in Figure 4.29.

Compressive test position	**A_s**	**A_L**
Flatwise with (0, 0.8, 1.6 mm) face layer	(a) 718.38	
Edgewise with (0 mm) face layer, without face	(b) 80 mm^2	(c) 453.4 mm^2
Edgewise with (0.8 mm) face layer	(d) 168mm^2	(e) 473.7 mm^2
Edgewise with (1.6 mm) face layer	(f) 248 mm^2	(g) 641.6 mm^2

Figure 4.25 illustrates the stress-strain curves derived from two distinct positions in the compressive test. The outcomes reveal variations in the mechanical properties of the materials under stress between these two positions (edgewise and flatwise). In the edgewise position (Figure 4.25b), the maximum stress is delineated across two cross-section areas: small (A_S) and large (A_L) cross-sections. Specifically, the edgewise configuration with a 1.6 mm face layer displayed a maximum stress of 44 MPa for V_S and 15 MPa for V_L. where V_s represents the compressive load applied over the small area, and V_L corresponds to the compressive load applied over the large area. Contrastingly, specimens lacking a face layer achieved a peak stress of 48 MPa in the flatwise test position (Figure 4.25a). This value surpasses the maximum stress obtained by specimens with 0.8 mm and 1.6 mm face layers by 20% and 23%, respectively. This is because removing the face layer can significantly enhance the structure's performance by increasing flexibility, reducing weight, and improving stress distribution within the core material. These factors collectively contribute to a higher maximum load capacity.

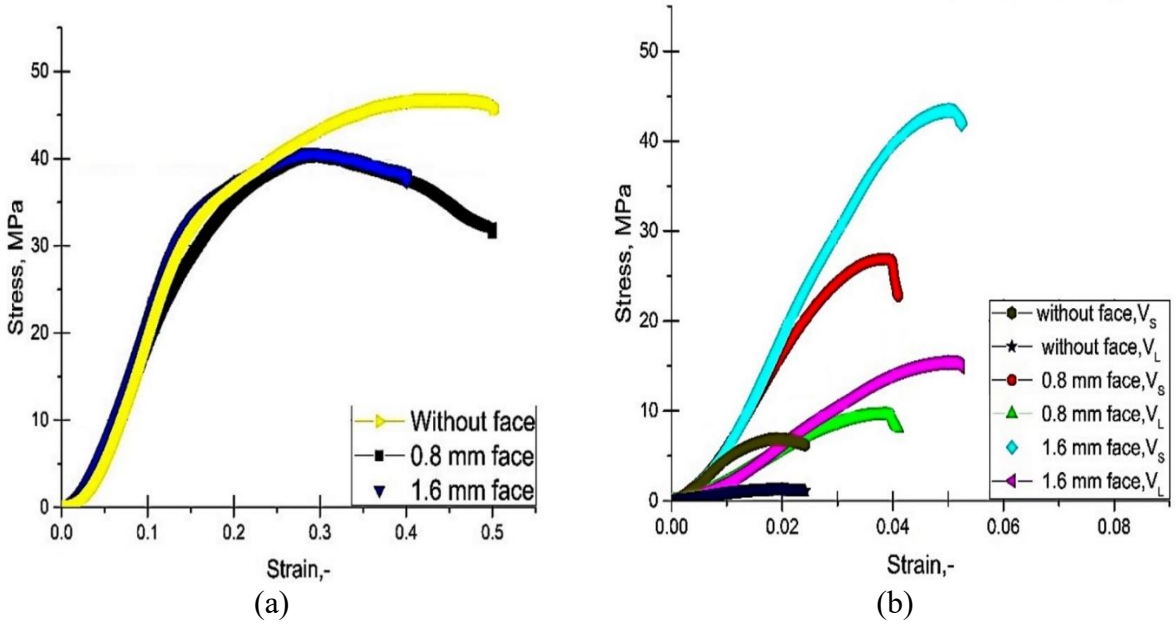

Fig 4.25. Stress-strain curves of the compression specimens: (a) flatwise (vertical to the surface), (b) edgewise (parallel to the surface)

Flatwise tests are typically more representative of the core's compressive strength, while edgewise tests evaluate the shear strength of the core. The differences in results between the two

tests highlight the anisotropic nature of the material, meaning its properties vary with direction. The flatwise test yielded significantly higher maximum loads compared to the edgewise test for all face layer thicknesses. The displacement at maximum load varied between the flatwise and edgewise tests. The differences in displacement may be related to the mode of failure (e.g., buckling, delamination), which could vary between the two test orientations. The flatwise test generally exhibited higher displacements, which may be due to the different loading directions and the response of the structures under compression. Within the flatwise tests, the face layer thickness (0.8 mm vs. 1.6 mm) did not seem to significantly affect the maximum load or the displacement at maximum load. This suggests that a 0.8 mm face layer might perform similarly to a 1.6 mm skin face in flatwise compressive strength.

The choice between the two face layer thicknesses appears to have a more noticeable impact in the edgewise orientation, where the 1.6 mm face layer thickness achieved the highest maximum load. These results indicate that the presence of the face layer effectively prevents buckling by enhancing rigidity and providing vital confinement to the core material. In contrast, specimens without a face layer are more prone to buckling under edgewise compressive loads, which consequently diminishes the structure's capacity to support higher loads. These results suggest that the face layer's orientation and presence should be considered when designing re-entrant honeycomb sandwiches, as they substantially impact their compressive strength and deformation behavior.

Subjected to compressive edgewise loading specimens without a face layer experienced layer-by-layer crushing. When the deformed layer was completely crushed, the neighboring layer started to deform, and the force began to drop. This layer-by-layer crushing resulted in oscillations in the force-displacement curve. The crushing of one layer of cells corresponds to one period (trough-peak–trough) of the Force-displacement curve (Figure 4.26a). A small lateral contraction was observed, as illustrated by the measured dimensions in Figure 4.26d. This deformation pattern continued until all layers were completely crushed, forming densification. Snapthrough instability is a common name for this phenomenon (Shilkrut, 2002). The concept of snap-through instability is employed in the design of materials featuring polymer-based multistable structures that can respond to both compressive and tensile loads (Rafsanjani et al., 2015).

In the case of specimens with a 0.8 mm face layer, fracture initiation began on the skin face. As the compressive load was applied, an inflection point or a point of bending appeared in the skin face. This is because the skin face initially resists the load, causing it to deform or bend before failing. As the load increased, it began to transfer to the inside structural layers. The scenario for specimens with a 1.6 mm face layer was similar but with a notable difference (Figure 4.26 b,c,f). In this case, there was a more significant separation between the re-entrant structure (the core) and the skin face. This gap or split may have provided more flexibility for the skin face before it started transferring the load to the core. The load transfer and deformation started similarly with the skin face experiencing an initial crack and deformation.

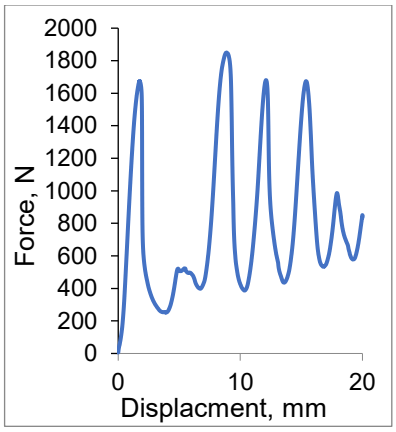
Force, N
2000
1800
1600
1400
1200
1000
800
600
400
200
0
0
10
20
Displacment, mm

(a)

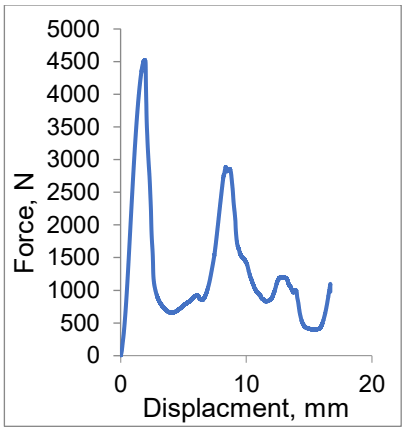
Force, N
5000
4500
4000
3500
3000
2500
2000
1500
1000
500
0
0
10
20
Displacment, mm

(b)

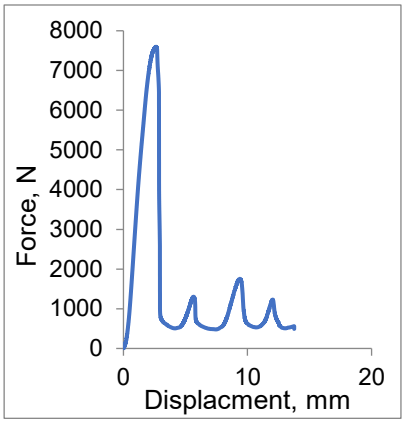
Force, N
8000
7000
6000
5000
4000
3000
2000
1000
0
0
10
20
Displacment, mm

(c)

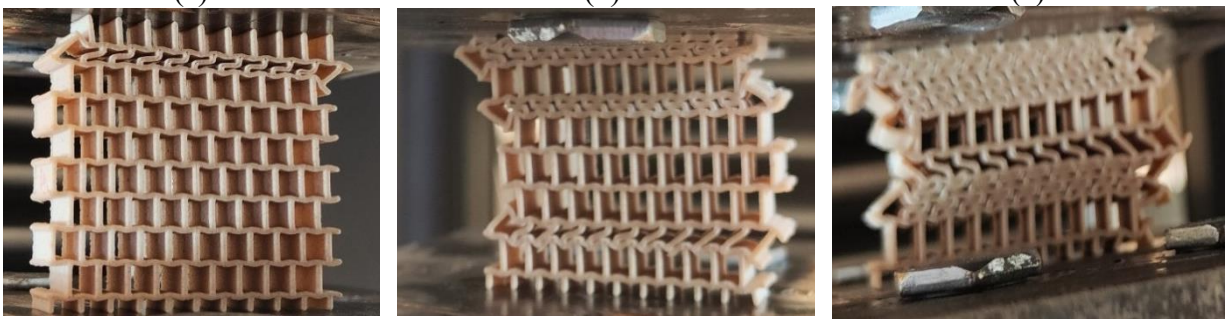

(d)

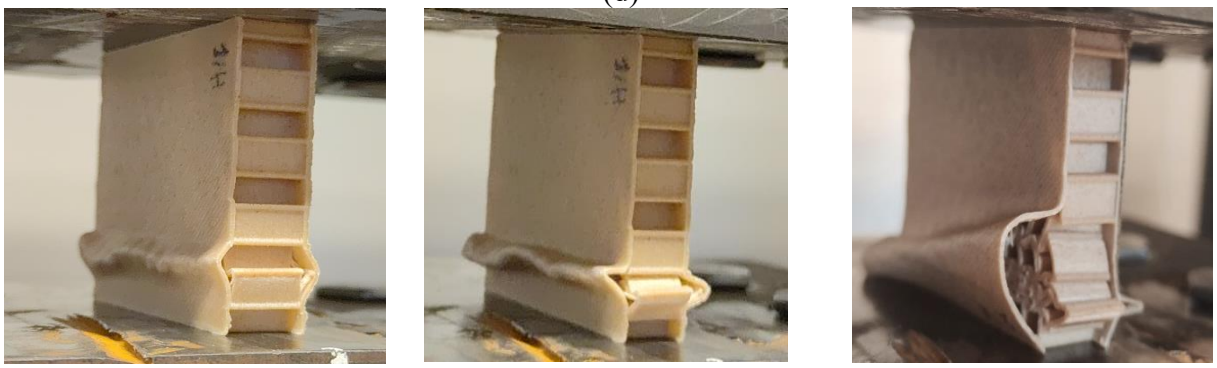

(e)

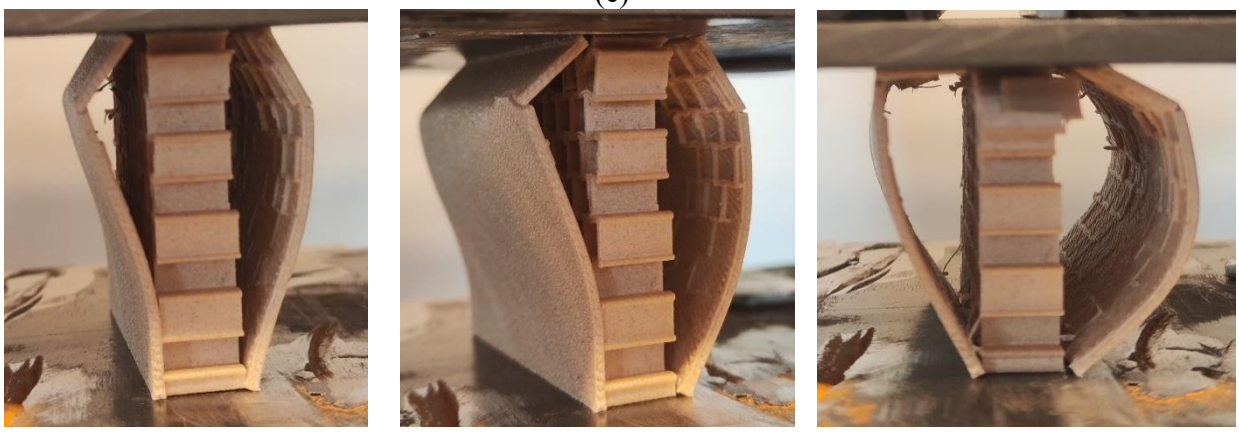

(f)

Fig 4.26. Edgewise compression results: (a-c) Load-displacement curves for specimens with different face layers (none, 0.8 mm, 1.6 mm); (d-f) Photographs of testing stages for each specimen.

When subjected to the flatwise compressive test, the samples exhibit a linear elastic response until the initiation of matrix cracking, leading to a subsequent decrease in load attributed to core yield. This sequence persists until the stacks experience total failure, prompting the face sheets to compress the stacks, resulting in a subsequent increase in load. All compression-tested sandwich structures exhibited the same deformation mechanism, namely, the buckling of the honeycomb core (Figure 4.27a). Thus, the sandwich structures experienced crushing of the honeycomb core, while the skin showed no failures (Figure 4.27b and 4.27c).

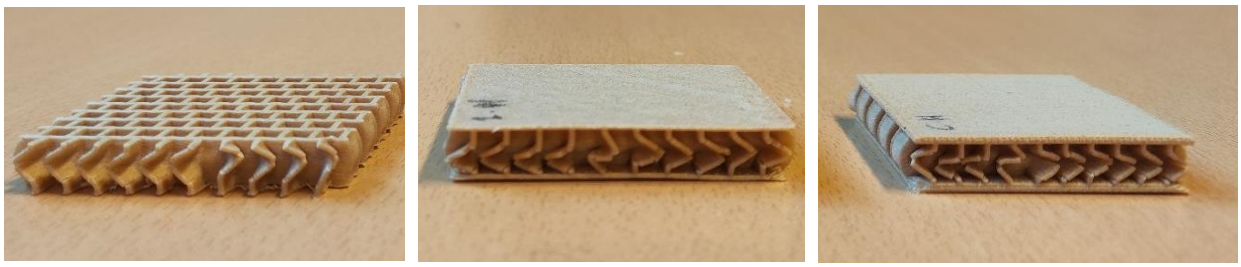

(a) (b) (c)

Fig 4.27. Flatwise compression test results: (a) sample without face layer, (b) sample with 0.8 mm face layer, and (c) sample with 1.6 mm face layer.

The maximum stress-to-mass ratio for compressive specimens was also studied. Figure 4.32 illustrates the specific strength obtained from the compressive test. The maximum specific strength for the edgewise-examined specimens was for the specimens with a 1.6 mm face layer at 2580 MPa/Kg, on the other hand, for the flatwise examined specimens the maximum specific strength was to the specimens without face layer at 5440 MPa/Kg. The lowest specific strength for the compressed specimens was for the edgewise specimens at 805 MPa/Kg.

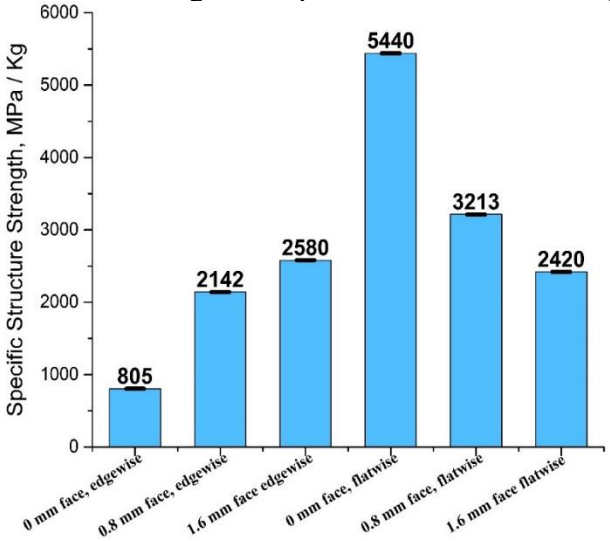

Fig 4.28. Specific strength derived from the compressive tests.

4.4.2.3 Numerical analysis of Bending and Compression Tests

By comparing simulations results with experimental data, we can validate and enhance our comprehension of material behavior under different loading conditions. Figure 4.29 represents the comparison of experimental flexural modulus and simulated flexural modulus. The outcomes of the simulation and the experiment are in good accord. Flexural experimental modules show lower values than flexural simulated modules, which may be due to the existence of layer air gaps, and impurities which make it difficult to achieve homogeneity of the mechanical properties (Rafsanjani et al., 2015).

Table 4-7 presents the maximum bending strength (MBS) and flexural modulus (E) of experimental and simulated works. Table 4-8 presents the maximum compressive strength (MCS) and the compressive modulus of elasticity (E) for all compressive tested specimens, for both experimental and simulated results.

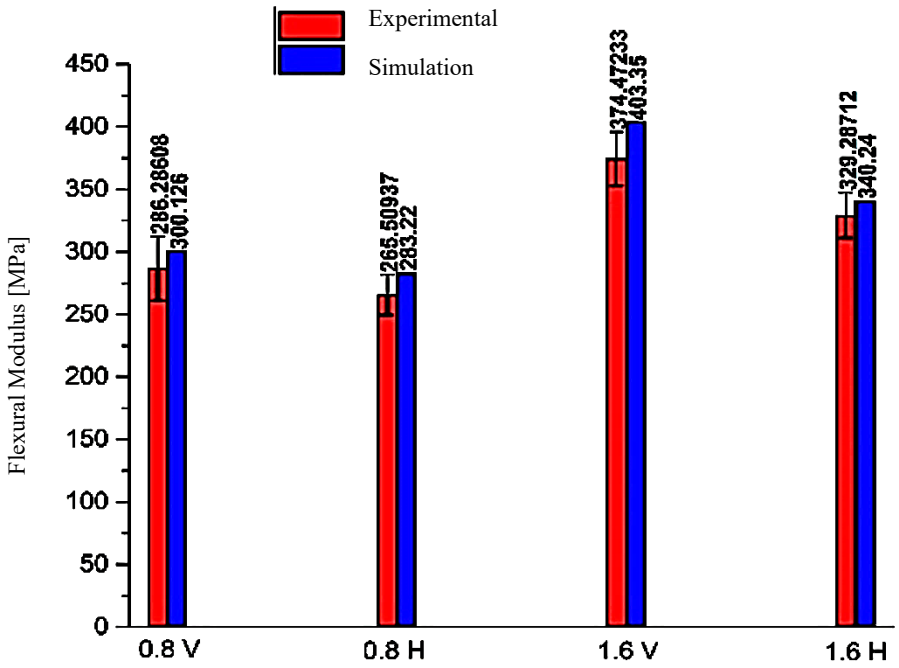

Fig 4.29. Comparison of experimental and simulated flexural modulus

Table 4.7 Maximum bending strength (MBS) and flexural modulus (E) values for different bending positions.

Specimens, Position	**MBS experimental (MPa)**	**E experimental (MPa)**	**E numerical (MPa)**
In-plane with 0.8 mm face layer	91.19	286.29	300.13
In-plane with 1.6 mm face layer	124.02	374.47	403.35
Out-of-plane with 0.8 mm face layer	42	265.51	283
Out-of-plane with 1.6 mm face layer	98.02	329.29	340.24

In the case of the compression test, discrepancies between the experimental modulus of elasticity and simulated modulus of elasticity were observed. The maximum deviations of the

simulated modulus of elasticity compared to the experimented modulus of elasticity are around 17% and 10% in the cases of flatwise and edgewise, respectively. The Comparison of the experimental compression modulus of elasticity and simulated modulus of elasticity in the compression tests is shown in Figure 4.30.

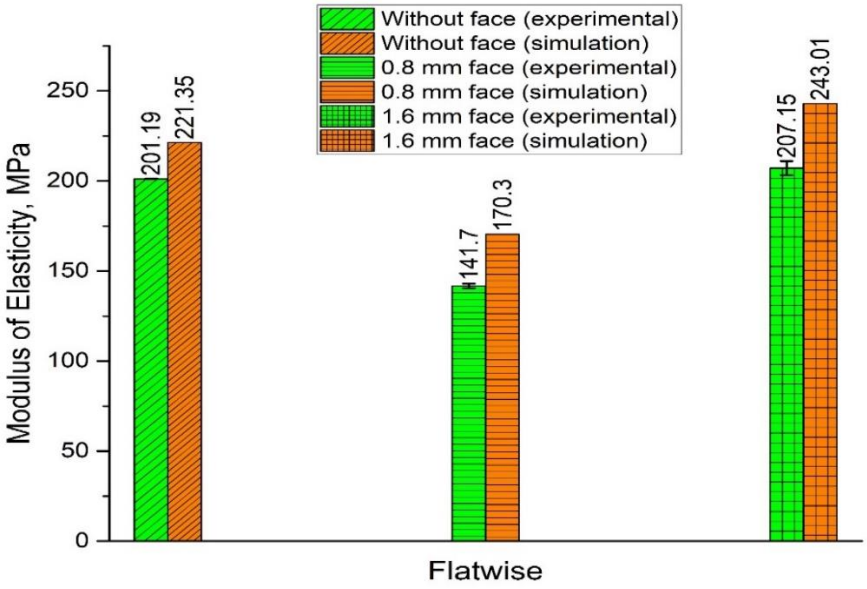

(a)

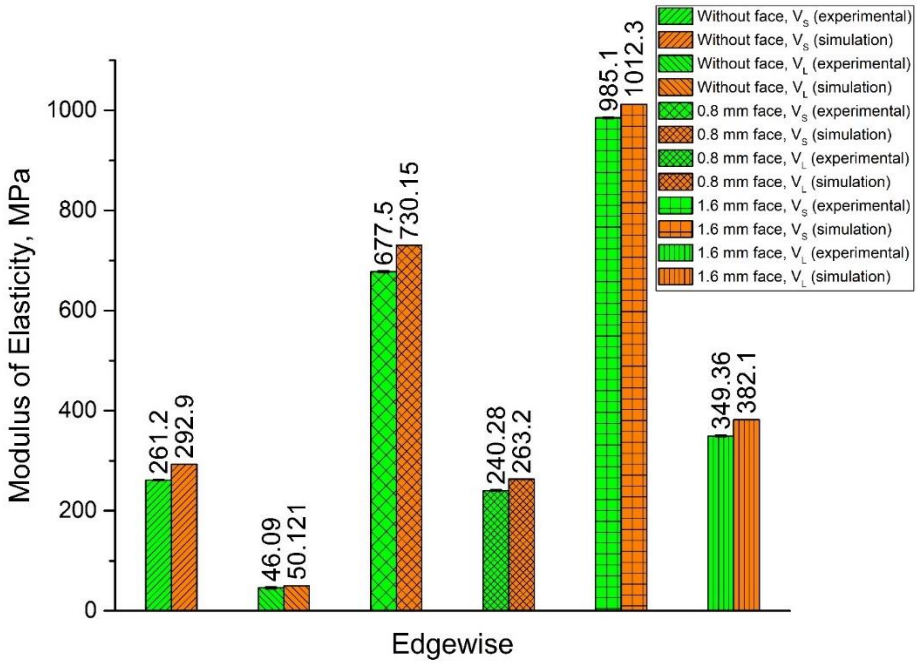

(b)

Fig 4.30. Comparison of experimental and simulated compression modulus of elasticity: (a) flatwise, (b) edgewise.

Table 4.8 Maximum compressive strength (MCS) and compressive modulus of elasticity (E) values at various compressive positions.

Specimens and position	**MCS $_{experimental}$ (MPa)**	**E $_{experimental}$ (MPa)**	**E $_{numerical}$ (MPa)**
Flatwise without face layer (0 mm)	46.7	201.2	221.35
Flatwise with (0.8 mm) face layer	40.2	141.7	170.3
Flatwise with (1.6 mm) face layer	40.7	207.15	243
Edgewise without face layer (0 mm), As	6.91	261.2	292.9
Edgewise without face layer (0 mm), A_l	1.22	46.1	50.12
Edgewise with face layer (0.8 mm), As	26.8	677.5	730.15
Edgewise without face layer (0.8 mm), A_l	9.5	240.28	263.2
Edgewise with face layer (1.6 mm), As	43.4	985.1	1012.13
Edgewise without face layer (1.6 mm), A_l	15.4	349.36	382.1

4.4.2.4 Summary and conclusions on re-entrant honeycomb core

In chapter (4.4.2), the compression/ bending properties of wood/PLA sandwich re-entrant honeycomb structures have been studied. The effects of different face layer thicknesses under different core positions (in-plane and out-of-plane) for bending properties and different applied loads (edgewise and flatwise) for compression properties were studied. The following conclusions can be drawn:

- The face layer thickness significantly impacted the 3-point bending properties of the in-plane and out-of-plane specimens. As the face layer thickness increased, the bending properties improved substantially.
- Different failure mechanisms arise under bending loads: compressive stress occurs in the upper face sheet, transverse shear significantly affects the core, and tensile stress develops in the lower face sheet.
- The addition of the face layer greatly increased the maximum load the structure could withstand when compressed edgewise. However, this test primarily assessed the buckling behavior of the face sheet rather than the overall compressive strength of the structure. Additionally, thicker face skins delayed load transfer and increased the gap between the face and core. The re-entrant honeycomb's anisotropic and heterogeneous nature impacts this behavior, underscoring the need for targeted design optimization.
- The flatwise compressive tests showed that the re-entrant structure without a face layer achieved the highest maximum load. Introducing face layers led to reduced displacement, indicating increased stiffness and decreased deformability. However, during the test, the re-entrant core of the sandwich construction was crushed, while the skin remained intact.
- The experimental and numerical (simulation) results showed good convergence and agreement in the modulus of elasticity, flexural modulus (stress-strain data), and stress concentration.

The results emphasize the importance of considering material anisotropy and the role of face layers in determining the compressive and bending behaviors of wood/PLA composite structures. These findings provide valuable insights for optimizing the design and application of such materials across various engineering contexts. This methodology holds significant potential in industries, particularly in the manufacturing and design of prototypes. Further exploration of cellular structure geometries and topologies can lead to improved mechanical properties of sandwich panels, advancing the application of these materials.

4.5. Neat, single, and multi-gradient composites

4.5.1 Tensile performance of neat, single, and multi-gradient composites

Figure 4.31 presents the tensile properties of neat (100% PLA (P), 100% PETG (G), 100% CF-PLA (CFP), 100% CF-PETG (CFG)), single (50% PLA + 50% CF-PLA (PCFP), 50% PETG + 50% CF-PETG (GCFG), 50% PLA + 50% PETG (PG)), and multi-graded (25% PLA + 50% CF-PLA + 25% PLA (PCFPP), 25% PETG + 50% CF-PETG + 25% PETG (GCFGG), 25% PETG + 50% PLA + 25% PETG (GPG)) materials. Specifically, Figure 4.31(a) shows the tensile force-elongation curves for the neat, single, and functionally graded composites. Figures 4.31(b) and 4.31(c) display the Young's modulus (E modulus) and tensile strength of different graded composites for the PLA, CF-PLA, PETG, and CF-PETG materials. In addition, Table 4.8 provides a detailed comparison of the tensile properties of the examined specimen materials. The results indicate that the tensile strengths of the neat materials are quite similar, with neat PLA exhibiting a slightly higher tensile strength than PETG by 0.03%. Generally, PLA is recognized for its higher tensile strength compared to PETG, making it a more rigid material with lower elongation at break. Conversely, PETG demonstrates higher elongation at break, making it more flexible, impact-resistant, and less brittle than PLA. For specimens composed of 100% layers, the tensile strength of CF-PLA was 0.04% higher than that of neat PLA. In contrast, the tensile strength of CF-PLA decreased by 65% compared to neat PETG. This reduction could be attributed to the introduction of carbon fibers, which potentially increases the occurrence of microvoids within the printed layers, thereby diminishing the overall tensile strength of the composite.

To compare the tensile strength of various additively manufactured specimens, the highest tensile strength, 47.4 MPa, was achieved by specimens composed of PCFPP. This was close to the specimens manufactured by PCFP, which showed a tensile strength of 46.2 MPa. Specimens manufactured with multi-layers of CFPLA and PLA composite showed improved tensile strength, with increases of 4% for PCFP and 7% for PCFPP compared to neat PLA. Conversely, specimens manufactured with multi-material layers of PETG and CF-PETG experienced a reduction in tensile strength compared to neat PETG. The tensile strength decreased by 4% for GCFGG and by 5% for GCFG. These results demonstrate the distinct impacts of material compositions on tensile strength, showcasing the advantages of CFPLA in enhancing tensile properties while also highlighting the challenges of integrating carbon fiber with PETG.

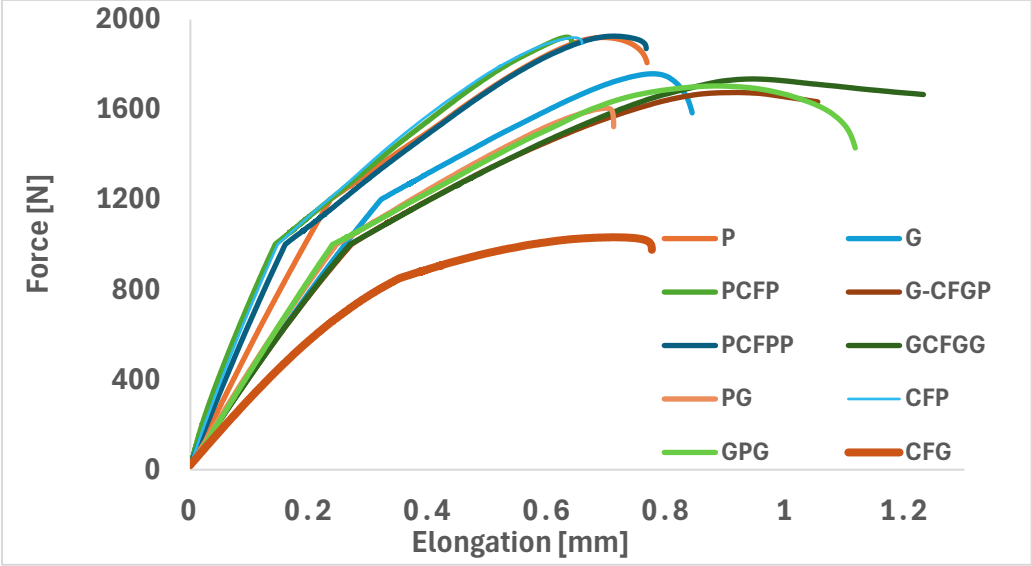

(a)

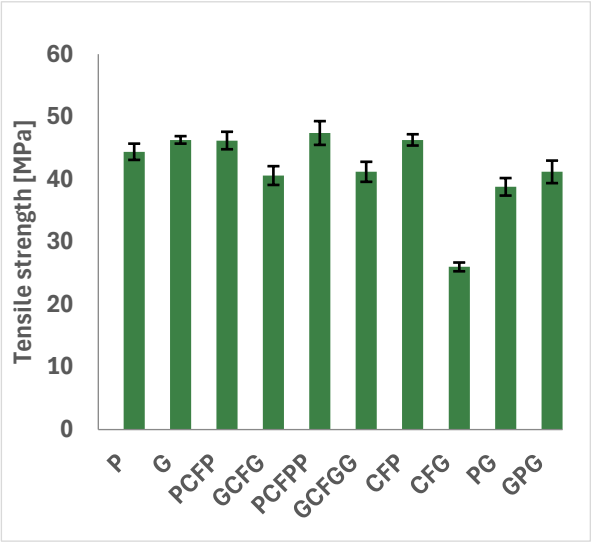

(b)

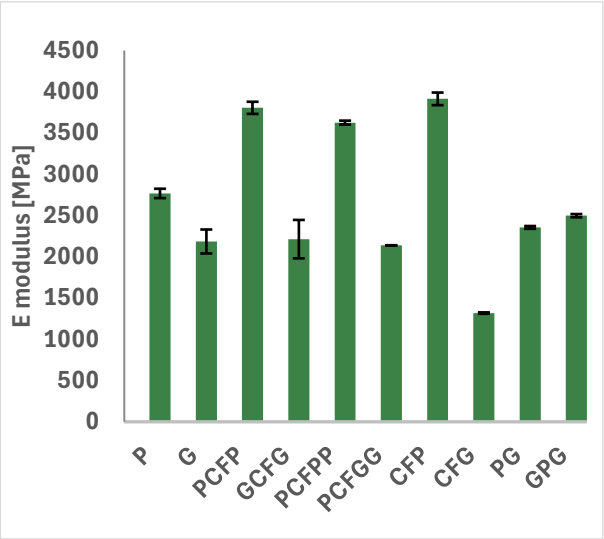

(c)

Fig 4.31. Tensile testing results: (a) Load-elongation curves, (b) tensile strength values, and (c) E-modulus measurements.

For the composite specimens of PLA and PETG, the highest tensile strength was observed in the GPG specimens, reaching 41.19 MPa. This value is lower than the tensile strength of specimens manufactured with 100% layers of neat PLA and neat PETG. The results suggest that while there are certain benefits to using a layered composite of PLA and PETG, the tensile strength of such composites does not always surpass that of using either material alone. This underscores the importance of optimizing the adhesion and intermolecular forces between different materials in composites to fully leverage their individual advantages. Enhancing the interfacial adhesion between PLA and PETG may facilitate the development of composite materials that optimally exploit the complementary mechanical properties of each constituent, representing a promising direction for future research.

For the tensile modulus, specimens manufactured with 100% CF-PLA layers exhibited the highest tensile modulus at 3914 MPa. Among the single and multi-graded PLA + CFPLA multi-material composites, the specimens composed of 50% PLA + 50% CF-PLA showed a relatively high tensile modulus of 3805 MPa, outperforming other multi-layered composites. Conversely, the lowest tensile modulus was observed in the specimens manufactured with 100% CF-PETG, with a value of 1318 MPa. Furthermore, the multi-layered composites of PLA and PETG displayed reduced mechanical properties, which can be attributed to inadequate interfacial bonding between the two polymers. This poor adhesion likely stems from the differences in optimal printing temperatures and material characteristics of PLA and PETG, which hinder the formation of a strong, cohesive bond during the AM process.

Table 4.9. Mechanical qualities of the single, multi-graded, and neat materials.

Materials	**Maximum applied load [N]**	**Elongation at maximum applied load [mm]**	**Maximum stress [MPa]**	**E-modulus [MPa]**
P	1920 ±65.2	0.69 ±0.07	44.4 ±2.5	2768 ±96
G	1759 ±119.5	0.77 ±0.09	42.9 ±3.19	2185 ±105
PCFP	1921.7 ±82.1	0.63 ±0.13	46.2 ±3.56	3805 ±173
GCFG	1675 ±96.7	0.91 ±0.05	40.6 ±1.47	2214 ±151
PCFPP	1926.2 ±102.6	0.71 ±0.04	47.4 ±2.41	3626 ±127
GCFGG	1736 ±67.7	0.94 ±0.16	41.2 ±1.53	2138 ±208
CFP	1919.8 ±76.1	0.64 ±0.15	46.3 ±1.62	3914 ±76
CFG	1032 ±82.8	0.7 ±0.06	26 ±2.61	1318 ±84
PG	1606 ±99.7	0.69 ±0.09	38.8 ±2.2	2356 ±169
GPG	1705 ±52.9	0.88 ±0.17	41.19 ±1.84	2498 ±197

Optical microscope images of the fractured surfaces of the neat, single, and multi-graded composite material specimens are presented in Figure 4.32. The fractured surfaces of PLA appeared brittle, as indicated by the clear and sharp fracture edges. The fracture process exhibited deformation and elongation of the PETG, highlighting an increase in toughness (Figure 4.32d). Moreover, the fracture of the PLA matrix within the CFPLA layers exhibited brittleness, and clear gaps between the PLA substrate and the carbon fibers suggested an inadequate bonding interface (Figure 4.32d). In CF-PETG, noticeable structural changes around the fibers can be observed, demonstrating how the stiffness of PETG interacts with the gritty texture of the carbon fibers (Figure 4.32 h). The composite specimens manufactured by PLA mixed with PETG exhibited a clear, sharp boundary between the different parts. This difference in behavior between the materials can create some pressure, possibly causing the layers to separate (see Figure 4.32 j).

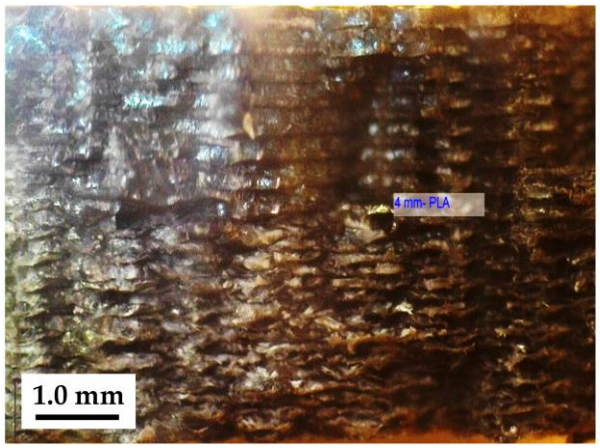

(**a**) (100% PLA)

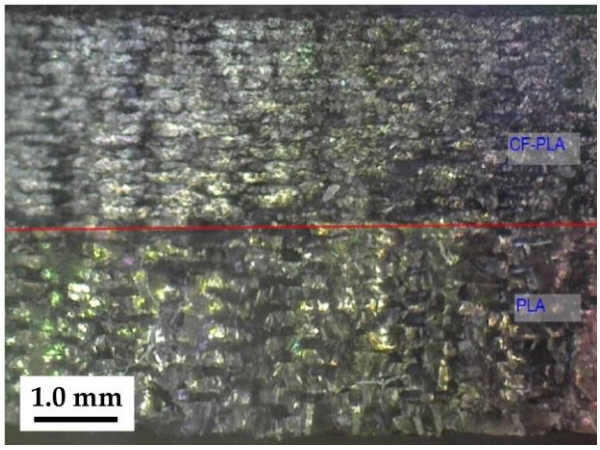

(**b**) (50% PLA + 50% CF-PLA)

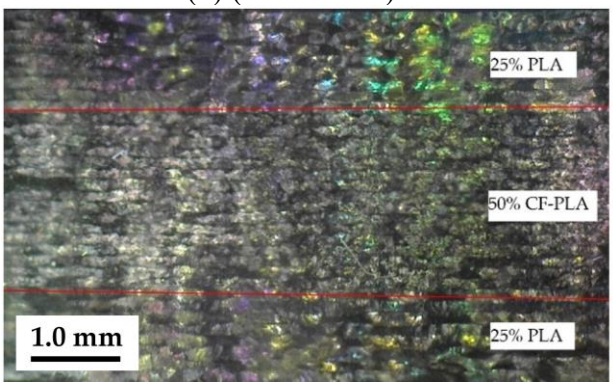

(**c**) (25% PLA + 50% CF-PLA + 25% PLA)

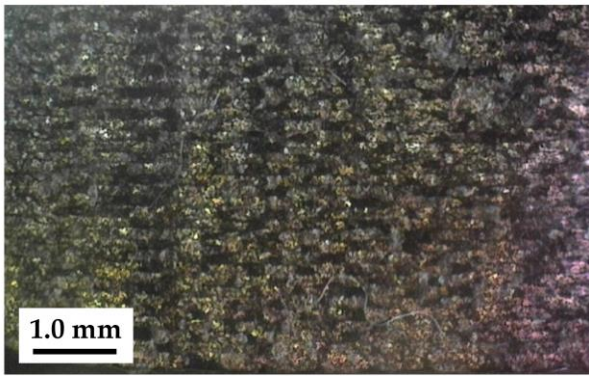

(**d**) (100% CF-PLA)

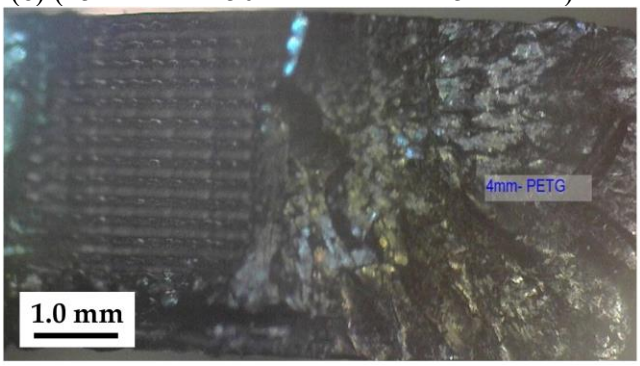

(**e**) (100% PETG)

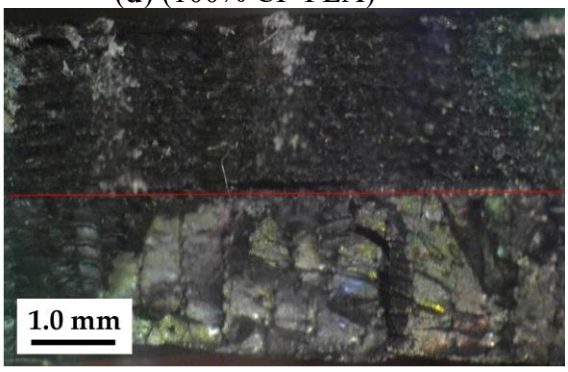

(**f**) (50% PETG + 50 % CF-PETG)

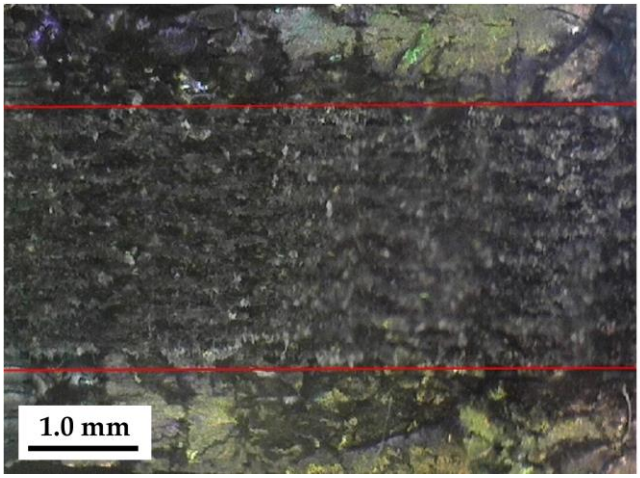

(**g**) (25%PETG + 50%CF-PETG + 25%PETG)

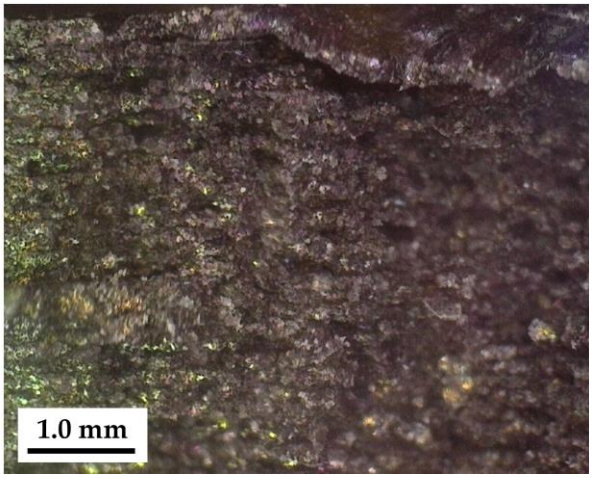

(**h**) (100% CF-PETG)

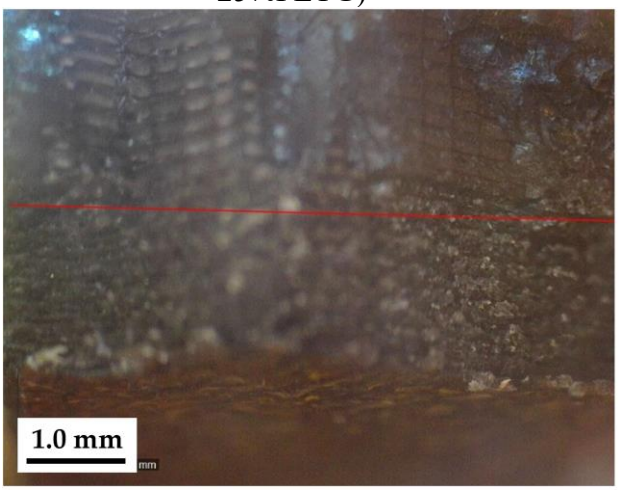

(**i**) (50% PLA+ 50 % PETG)

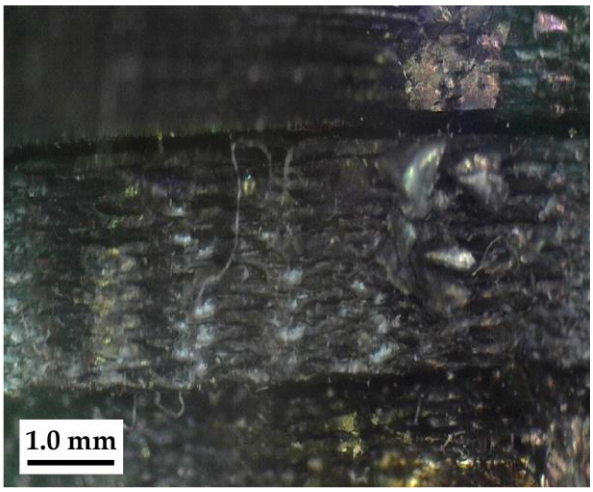

(**j**) (25% PETG + 50% PLA+ 25% PETG)

Fig 4.32. Microscopy images of fractured zones in test specimens: (a) P, (b) PCFP, (c) PCFPP, (d) CFP, (e) G, (f) GCFG, (g) GCFGG, (h) CFG, (i) PG, and (j) GPG.

The multi-material composite designs explored in this research can be applied to other polymer-based materials, providing valuable insights for the additive manufacturing and materials science communities. These findings encourage further exploration into sustainable materials for real-world applications like short-life-cycle or non-critical components such as accessories, tool holders, robotic effectors, educational models, disposable items, and general-purpose prototyping, where PLA and PETG's properties, such as ease of printing and rigidity, can be effectively utilized.

4.5.2. Summary and conclusions on neat, single, and multi-gradient composites

This research offers an in-depth evaluation of mechanical properties, focusing on the influence of material composition. Extensive tensile testing revealed significant insights into the mechanical behavior of the specimens. The main conclusions of this study are as follows:

- Specimens made entirely of CF-PLA showed a tensile modulus of 3914 MPa, while a 50% PLA + 50% CF-PLA multi-material composite demonstrated effective

reinforcement with a tensile modulus of 3805 MPa. However, 100% CF-PETG had the lowest tensile modulus at 1318 MPa, pointing to potential fiber-matrix interaction issues.

- Multi-layered PLA and PETG composites showed reduced mechanical performance, largely due to sharp interfaces between the materials causing stress at the transition points, which can lead to delamination. Optimizing the adhesion at the PLA–PETG interface could enable the design of composite materials that synergistically combine the strengths of both polymers, providing a valuable avenue for future study.

4.6 New scientific results

The mechanical characteristics of 3D-printed polymers, polymer composites, sandwich structures were comprehensively investigated in this study. The following points are noteworthy to be mentioned:

1. ***Mechanical Characterization of 3D-Printed Polymers: Role of Re-Manufacturing and Fiber Reinforcement***

I investigated the mechanical behaviour of both original and re-manufactured polymer and fiber-reinforced filaments used in 3D printing The study encompasses a range of materials, including PLA, recycled PLA (rPLA), PETG, carbon fiber-reinforced PLA and PETG (CF-PLA, CF-PETG), as well as natural fiber-reinforced variants. Among all tested materials, recycled PLA (rPLA) demonstrated the most favorable mechanical properties, outperforming both pure and carbon fiber-reinforced variants in tensile and compressive strength, by up to 100% and 67%, respectively.

Further analysis revealed that re-manufacturing impacted tensile performance depending on the material type. While recycled CF-PLA showed a slight 4% reduction in strength due to fiber clustering, re-manufacturing CF-PETG proved more challenging due to extrusion inconsistencies.

In a further effort to enhance sustainability, natural fibers were introduced as reinforcement agents. The inclusion of 7 wt% hemp fiber in rPLA resulted in a 7% increase in tensile strength relative to the original material. Likewise, the addition of 7 wt% jute fiber to PETG improved its tensile strength by 12% compared to the original and by 15% compared to its recycled form. Although variability in filament diameter posed challenges for compatibility with certain 3D printers, the production of mechanically reliable samples was successfully achieved and tested.

2. ***Influence of the core orientation and face skin thickness on bending and compressive properties.***

I offered valuable insights into the mechanical behavior of 3D-printed re-entrant honeycomb sandwich structures, focusing on the effects of face layer thickness, core orientation, and loading conditions. I confirmed that increasing the thickness of the face skin significantly enhances bending strength and stiffness.

Additionally, the in-plane core orientation demonstrated higher bending strength compared to the out-of-plane orientation. In flatwise compression, the re-entrant core without a face layer remarkably sustained a maximum load, which improved flexibility and stress distribution, enhancing compressive strength, suggesting that lighter structures can withstand substantial loads.

3. Effects of neat, single, and multi-graded composites on tensile strength properties

In this research, I investigated the tensile properties of various neat and composite materials, specifically neat PLA, PETG, CF-PLA, CF-PETG, and their combinations.

I demonstrated that multi-layer composites comprising CF-PLA and PLA exhibited an increase in tensile strength of 4% for the PCFP configuration and 7% for the PCFPP configuration compared to neat PLA. Additionally, I found that the tensile strength of multi-material PETG and CF-PETG composites declined relative to neat PETG, with reductions of 4% for the GCFGG configuration and 5% for the PCFP configuration.

I also observed that the highest tensile strength among the composite specimens made from PLA and PETG was found in the GP configuration, although this strength was lower than that of the neat materials.

Furthermore, my microscopic analysis revealed brittle fractures in the PLA specimens and clear separation between layers in the PLA/PETG composites, indicating poor adhesion at the interfaces.

5. CONCLUSION AND SUGGESTIONS

In this study, the mechanical behavior of FDM printing pure PLA/ PETG, and PLA/PETG composites were reviewed exhaustively. Based on the assessment of the results, the following observations can be drawn:

- The ASTM 3039 standard geometry demonstrated superior tensile properties compared to the dumbbell-shaped samples with curved edges, as defined by ISO 527 and ASTM 638.
- Numerical analysis of stress concentration: The ISO 527-2 specimens showed reduced stress concentration near the gripping area, with higher stress localized in the narrow gauge section, away from the clamping zones.
- The Young's modulus and UTS are maximum at On-edge print orientation due to its robust construction, while elongation at break is better at Flat orientation.
- The choice of standard should be application-specific: ISO 527 is preferable for fracture behavior studies, while ASTM D3039 is better suited for assessing tensile performance
- Carbon fiber-reinforced PLA (CF-PLA) obtained better compressive and tensile properties than carbon fiber-reinforced PETG polymer.
- rPLA filament obtained better compressive and tensile properties in compared with CF-PLA, CF-PETG, and PETG polymer (CF-PETG).
- Among the original filaments, CF-PETG exhibited the highest filaments tensile strength, surpassing PLA, PETG, CF-PLA, and rPLA.
- In the case of re-manufactured filaments, the results were more varied. Recycled PLA (rPLA) demonstrated a significant 29% increase in tensile strength when reinforced with hemp fibers, outperforming its original filaments. Conversely, recycled CF-PLA showed a slight 4% decrease in tensile strength compared to its original filaments. For PETG, the re-manufactured filaments exhibited lower tensile strength than the original; however, the addition of jute fibers significantly enhanced the performance of both recycled and original PETG.
- The rhombus sandwich samples demonstrated better tensile, compressive, and flexure strength compared to the honeycomb structure, attributed to their robust core design
- Increasing the face layer thickness significantly enhanced the bending properties of both in-plane and out-of-plane re-entrant sandwich structure core specimens.
- Thicker face skin enhances the maximum applied load when compressed from the edgewise, creating a more pronounced gap between the face skin and the core.
- Flatwise compressive tests indicated that the re-entrant structure, when lacking a face layer, exhibited the highest maximum load capacity.
- Tensile tests of multi-material layers revealed that % CF-PLA exhibited the highest modulus of elasticity, with the 50% PLA + 50% CF-PLA composite showing nearly equivalent results. In comparison, 100% CF-PETG displayed the lowest modulus, suggesting possible issues with fiber-matrix interaction.

Further innovation in core designs for sandwich structures is also needed, particularly through exploring advanced auxetic or lattice cores that could improve strength-to-weight ratios and resistance to impact. Another important direction is to evaluate the performance of FDM-printed materials under diverse environmental conditions such as changes in temperature, humidity, and chemical exposure. Long-term studies should also be conducted on the degradation of the mechanical properties of FDM composites under cyclic loading and environmental stresses.

Moreover, exploring methods for recycling printed components and composites would reduce environmental impact and promote circular material use.

The findings of this study also highlight several avenues for advancing numerical modeling. Extending finite element modeling by adopting fully anisotropic constitutive laws, incorporating multi-orientation testing, and implementing cohesive-zone adhesion would provide a more comprehensive representation of both global structural responses and localized failure mechanisms in FDM parts. Comparative analyses with pure PLA specimens are recommended to isolate and evaluate the specific effects of recycling and reinforcement on material integrity and structural performance. In addition, developing optimized re-extrusion methods to produce dimensionally stable reinforced filaments would enable stronger correlations between filament properties and the mechanical behavior of printed structures.

Further investigation into sandwich structures should also incorporate cyclic and vibration-based flatwise compression tests to capture progressive damage and collapse mechanisms in cores with out-of-plane orientations. Linear regression should be applied across the elastic region of tensile curves in future studies to provide a more statistically robust estimation of Young's modulus, thereby strengthening the reliability of inter-specimen comparisons. Benchmark testing of solid specimens would also be beneficial in quantifying the trade-offs between strength and weight, while simultaneously highlighting the structural efficiency and lightweight advantages of rhombus and honeycomb cores for practical engineering applications.

Additionally, the implementation of cohesive zone models (CZM) to explicitly capture interlayer adhesion, particularly under loading conditions parallel to the build orientation such as edgewise compression, would refine predictive capacity for delamination and failure mechanisms, complementing the global behavior analyses performed in this work.

Finally, Improved interfacial compatibility between PLA and PETG may lead to composites with enhanced mechanical performance, highlighting an important focus for subsequent research efforts

6. SUMMARY

This study provides a comprehensive evaluation of the mechanical behavior of Fused Deposition Modeling (FDM) 3D-printed components, with a particular focus on the influence of print orientation, geometric configurations, sandwiches structures and multi-material compositions. The research investigates ASTM D3039 rectangular specimens printed at 0°, 15°, and 90° angles and compares them against other tensile samples in accordance with ASTM and ISO standards. All specimens were fabricated using polyethylene terephthalate glycol (PETG) material and were tested in two distinct print orientations: flat and on-edge. Finite Element Analysis (FEA) was employed to identify stress concentrations and weak points in each configuration. The study also extends to evaluating tensile and compressive behavior of various material compositions, including recycled polylactic acid (rPLA), PLA with carbon fiber reinforcement (CF-PLA), pristine PETG, and PETG reinforced with 10 wt.% carbon fiber (CF-PETG). Furthermore, the performance of pre-consumer recycled PETG and rPLA filaments reinforced with varying percentages of hemp and jute fibers was assessed. Additionally, the study examines the mechanical properties of sandwich structures using rhombus and honeycomb core geometries made from PLA. The research also analyzes the effect of face layer thickness variations (0 mm, 0.8 mm, and 1.6 mm) on re-entrant honeycomb core sandwich structures made from wood/PLA composite filaments. Material characterizations included bending tests, compressive tests, and finite element analysis (FEA) to identify stress concentration areas.. Finally, the mechanical behavior of multi-material composites, including neat PLA and PETG, single-graded combinations, and multi-gradient configurations, was thoroughly evaluated.

The ASTM D3039 specimens printed at 0° in the on-edge orientation exhibited the highest tensile properties, whereas the flat orientation showed superior results in terms of failure area. ISO 527-2 specimens consistently demonstrated lower tensile properties across all orientations. FEA analysis revealed minimal stress concentrations in ISO 527-2 specimens, with higher stress localized in the narrow regions, isolated from the gripping zones. Among the material compositions, rPLA exhibited the best overall tensile and compressive performance, outperforming both CF-PLA and CF-PETG, regardless of print orientation. PLA with carbon fiber reinforcement showed superior mechanical properties compared to its PETG counterparts. Recycled PLA filaments reinforced with hemp fibers significantly improved tensile strength compared to the original PLA, and jute-reinforced PETG showed notable strength improvements over the pristine PETG and its recycled versions. For the sandwich structures, rhombus cores displayed superior mechanical behavior, with enhanced tensile, bending, and compressive strengths compared to honeycomb configurations. Increasing face layer thickness greatly improved resistance to bending, and specimens with an in-plane orientation demonstrated higher bending strength than those with out-of-plane orientation due to increased material engagement. In flatwise compressive testing, specimens without a face layer exhibited the highest compressive strength due to greater displacement capacity. In contrast, edgewise compression tests indicated significant buckling behavior of the face sheet, with maximum stress increasing proportionally with face layer thickness. These results were validated through FEA, closely aligning with experimental findings. Lastly, multi-material composites generally showed lower mechanical performance compared to neat PLA and PETG due to reduced interlayer adhesion. These findings underscore the need for optimizing core architectures, material combinations, and reinforcement strategies to enhance the mechanical properties of 3D-printed composite structures for advanced manufacturing applications.

7. ÖSSZEFOGLALÁS (SUMMARY IN HUNGARIAN)

Ez a tanulmány a Fused Deposition Modeling (FDM) 3D-nyomtatott komponenseinek mechanikai viselkedését vizsgálja, különös figyelmet fordítva a nyomtatási orientációkra, geometriai konfigurációkra, szendvics szerkezetekre és több anyagú kompozitokra. A kutatás során 0°, 15° és 90°-os szögekben nyomtatott ASTM D3039 mintákat teszteltek különböző húzó- és nyomópróbákkal, valamint végeselem-elemzést (FEA) végeztek a feszültségkoncentrációk azonosítására. A vizsgált anyagok között szerepelnek a PETG, újrahasznosított PLA (rPLA), szénszál-erősített PLA (CF-PLA) és PETG (CF-PETG), továbbá kender- és jutaszálakkal erősített újrahasznosított szálak. A szendvicsszerkezetek mechanikai tulajdonságait is értékelték, figyelembe véve a fa/PLA kompozitok hajlítási és nyomópróbáit. A kutatás a több anyagú kompozitok mechanikai viselkedését is alaposan elemzi.

Az ASTM D3039 minták, amelyeket 0°-os szögben nyomtattak a szélen lévő tájolásban, a legmagasabb szakítószilárdságot mutatták, míg a lapos tájolás kiváló eredményeket mutatott a tönkremeneteli terület tekintetében. Az ISO 527-2 szabvány szerinti minták következetesen alacsonyabb szakítószilárdságot mutattak minden tájolásban. A FEM analízis minimális feszültségkoncentrációt mutatott ki az ISO 527-2 próbatestekben, nagyobb feszültséget a szűk régiókban lokalizálva, elkülönítve a megfogási zónáktól. Az anyagösszetételek közül az rPLA mutatta a legjobb általános húzó- és nyomóteljesítményt, felülmúlva a CF-PLA-t és a CF-PETG-t, függetlenül a nyomtatási tájolástól. A szénszál erősítésű PLA kiváló mechanikai tulajdonságokat mutatott PETG társaihoz képest. A kenderrosttal megerősített újrahasznosított PLA filamentek jelentősen javították a szakítószilárdságot az eredeti PLA-hoz képest, és a jutával megerősített PETG jelentős szilárdsági javulást mutatott az érintetlen PETG-hez és annak újrahasznosított változataihoz képest. A szendvicsszerkezetek esetében a rombuszmagok kiváló mechanikai viselkedést mutattak, nagyobb húzó-, hajlító- és nyomószilárdsággal a méhsejtszerkezetekhez képest. Az arcréteg vastagságának növelése nagymértékben javította a hajlítással szembeni ellenálló képességet, és a síkban orientált minták nagyobb hajlítószilárdságot mutattak, mint a síkon kívüli tájolásúak a megnövekedett anyagmozgás miatt. A lapos nyomóvizsgálat során a felületi réteg nélküli próbatestek mutatták a legnagyobb nyomószilárdságot a nagyobb elmozdulási kapacitás miatt. Ezzel szemben az élirányú kompressziós tesztek a homloklap jelentős kihajlási viselkedését mutatták ki, a maximális feszültség arányosan nőtt az arcréteg vastagságával. Ezeket az eredményeket a FEA-n keresztül validáltuk, szorosan összhangban a kísérleti eredményekkel. Végül a több anyagból álló kompozitok általában alacsonyabb mechanikai teljesítményt mutattak a tiszta PLA-hoz és PETG-hez képest a csökkent rétegközi tapadás miatt. Ezek az eredmények alátámasztják a magarchitektúrák, az anyagkombinációk és a megerősítési stratégiák optimalizálásának szükségességét a 3D-nyomtatott kompozit szerkezetek mechanikai tulajdonságainak javítása érdekében a fejlett gyártási alkalmazásokhoz.

8. APPENDICES

A1: Bibliography

1. Ahn, D., Kweon, J.-H., Choi, J., & Lee, S. (2012). Quantification of surface roughness of parts processed by laminated object manufacturing. *Journal of Materials Processing Technology*, *212*(2), 339–346. https://doi.org/10.1016/j.jmatprotec.2011.08.013
2. Aliheidari, N., Tripuraneni, R., Ameli, A., & Nadimpalli, S. (2017). Fracture resistance measurement of fused deposition modeling 3D printed polymers. *Polymer Testing*, *60*, 94–101. https://doi.org/10.1016/j.polymertesting.2017.03.016
3. Ameri, B., Taheri-Behrooz, F., & Aliha, M. R. M. (2021). Evaluation of the geometrical discontinuity effect on mixed-mode I/II fracture load of FDM 3D-printed parts. *Theoretical and Applied Fracture Mechanics*, *113*, 102953.
4. Ameri, B., Taheri-Behrooz, F., & Aliha, M. R. M. (2022). Mixed-mode tensile/shear fracture of the additively manufactured components under dynamic and static loads. *Engineering Fracture Mechanics*, *260*, 108185.
5. Amza, C. G., Zapciu, A., Constantin, G., Baciu, F., & Vasile, M. I. (2021). Enhancing Mechanical Properties of Polymer 3D Printed Parts. *Polymers*, *13*(4), 562. https://doi.org/10.3390/polym13040562
6. Anandkumar, R., & Babu, S. R. (2019). FDM filaments with unique segmentation since evolution: A critical review. *Progress in Additive Manufacturing*, *4*(2), 185–193.
7. Araya-Calvo, M., López-Gómez, I., Chamberlain-Simon, N., León-Salazar, J. L., Guillén-Girón, T., Corrales-Cordero, J. S., & Sánchez-Brenes, O. (2018). Evaluation of compressive and flexural properties of continuous fiber fabrication additive manufacturing technology. *Additive Manufacturing*, *22*, 157–164.
8. Assidi, M., & Ganghoffer, J.-F. (2012). Composites with auxetic inclusions showing both an auxetic behavior and enhancement of their mechanical properties. *Composite Structures*, *94*(8), 2373–2382. https://doi.org/10.1016/j.compstruct.2012.02.026
9. ASTM. (2014). *ASTM D638-14: Standard test method for tensile properties of plastics*.
10. ASTM, I. (2007). Standard test methods for flexural properties of unreinforced and reinforced plastics and electrical insulating materials. *ASTM D790-07*.
11. Bak, D. (2003). Rapid prototyping or rapid production? 3D printing processes move industry towards the latter. *Assembly Automation*, *23*(4), 340–345. https://doi.org/10.1108/01445150310501190
12. Bakarich, S. E., Gorkin, R., in het Panhuis, M., & Spinks, G. M. (2014). Three-Dimensional Printing Fiber Reinforced Hydrogel Composites. *ACS Applied Materials & Interfaces*, *6*(18), 15998–16006. https://doi.org/10.1021/am503878d
13. Bettini, P., Alitta, G., Sala, G., & Di Landro, L. (2017). Fused deposition technique for continuous fiber reinforced thermoplastic. *Journal of Materials Engineering and Performance*, *26*(2), 843–848.
14. Biron, M. (2012). *Thermoplastics and thermoplastic composites*. William Andrew.
15. Bogoeva-Gaceva, G., Raka, L., & Sorrentino, A. (2017). The effect of matrix morphology on dynamic-mechanical properties of polypropylene/layered silicate nanocomposites. *Macedonian Journal of Chemistry and Chemical Engineering*, *36*(2), 251–264.
16. Bondeson, D., & Oksman, K. (2007). Polylactic acid/cellulose whisker nanocomposites modified by polyvinyl alcohol. *Composites Part A: Applied Science and Manufacturing*, *38*(12), 2486–2492. https://doi.org/10.1016/j.compositesa.2007.08.001

17. Bryll, K., Piesowicz, E., Szymański, P., Ślączka, W., & Pijanowski, M. (2018). Polymer composite manufacturing by FDM 3D printing technology. *MATEC Web of Conferences*, *237*, 02006.
18. Caminero, M. A., Chacón, J. M., García-Moreno, I., & Rodríguez, G. P. (2018). Impact damage resistance of 3D printed continuous fibre reinforced thermoplastic composites using fused deposition modelling. *Composites Part B: Engineering*, *148*, 93–103. https://doi.org/10.1016/j.compositesb.2018.04.054
19. *Carbon PLA 1,75 mm / 1000 g*. (n.d.). 3DJake België. Retrieved May 16, 2025, from https://www.3djake.be/nl-BE/spectrum/carbon-pla
20. Carneiro, O. S., Silva, A. F., & Gomes, R. (2015). Fused deposition modeling with polypropylene. *Materials & Design*, *83*, 768–776. https://doi.org/10.1016/j.matdes.2015.06.053
21. Castoro, M., & Kumpaty, S. (2013). Impact of laser power and build orientation on the mechanical properties of selectively laser sintered parts. *Proceedings of The National Conference on Undergraduate Research (NCUR). University of Wisconsin La Crosse, WI*.
22. Chaturvedi, E., Rajput, N. S., Upadhyaya, S., & Pandey, P. K. (2017). Experimental Study and Mathematical Modeling for Extrusion using High Density Polyethylene. *Materials Today: Proceedings*, *4*(2), 1670–1676.
23. Chiulan, I., Frone, A., Brandabur, C., & Panaitescu, D. (2017). Recent Advances in 3D Printing of Aliphatic Polyesters. *Bioengineering*, *5*(1), 2. https://doi.org/10.3390/bioengineering5010002
24. Chuang, K. C., Grady, J. E., Arnold, S. M., Draper, R. D., Shin, E., Patterson, C., Santelle, T., Lao, C., Rhein, M., & Mehl, J. (2015). A Fully Nonmetallic Gas Turbine Engine Enabled by Additive Manufacturing. *Polymer Composites*, 24.
25. Chybowski, L., & Gawdzińska, K. (2016). On the Possibilities of Applying the AHP Method to a Multi-criteria Component Importance Analysis of Complex Technical Objects. In Á. Rocha, A. M. Correia, H. Adeli, L. P. Reis, & M. Mendonça Teixeira (Eds.), *New Advances in Information Systems and Technologies* (Vol. 445, pp. 701–710). Springer International Publishing. https://doi.org/10.1007/978-3-319-31307-8_71
26. Czél, G., Jalalvand, M., & Wisnom, M. R. (2016). Hybrid specimens eliminating stress concentrations in tensile and compressive testing of unidirectional composites. *Composites Part A: Applied Science and Manufacturing*, *91*, 436–447. https://doi.org/10.1016/j.compositesa.2016.07.021
27. D. Slavko and K. Matic,. (2010). *Selective laser sintering of composite materials technologies* (Vol. 21). Annals of DAAAM & Proceedings.
28. Dave, H. K., & Davim, J. P. (2021). *Fused Deposition Modeling Based 3D Printing*. Springer Nature.
29. De Castro, B. D., Magalhães, F. D. C., Panzera, T. H., & Campos Rubio, J. C. (2021). An Assessment of Fully Integrated Polymer Sandwich Structures Designed by Additive Manufacturing. *Journal of Materials Engineering and Performance*, *30*(7), 5031–5038. https://doi.org/10.1007/s11665-021-05604-8
30. Der Klift, F. V., Koga, Y., Todoroki, A., Ueda, M., Hirano, Y., & Matsuzaki, R. (2016). 3D Printing of Continuous Carbon Fibre Reinforced Thermo-Plastic (CFRTP) Tensile Test Specimens. *Open Journal of Composite Materials*, *06*(01), 18–27. https://doi.org/10.4236/ojcm.2016.61003

31. Dey, A., Hoffman, D., & Yodo, N. (2020). Optimizing multiple process parameters in fused deposition modeling with particle swarm optimization. *International Journal on Interactive Design and Manufacturing (IJIDeM)*, *14*(2), 393–405.
32. Dharmalingam, G., Arun Prasad, M., & Salunkhe, S. (2022). Investigation of impact strength at different infill rates biodegradable PLA constituent through fused deposition modeling. *Materials Today: Proceedings*, *62*, 551–558. https://doi.org/10.1016/j.matpr.2022.03.591
33. Dickson, A. N., Barry, J. N., McDonnell, K. A., & Dowling, D. P. (2017). Fabrication of continuous carbon, glass and Kevlar fibre reinforced polymer composites using additive manufacturing. *Additive Manufacturing*, *16*, 146–152. https://doi.org/10.1016/j.addma.2017.06.004
34. Dilberoglu, U. M., Gharehpapagh, B., Yaman, U., & Dolen, M. (2017). The Role of Additive Manufacturing in the Era of Industry 4.0. *Procedia Manufacturing*, *11*, 545–554. https://doi.org/10.1016/j.promfg.2017.07.148
35. Dudek, P. (2013). FDM 3D Printing Technology in Manufacturing Composite Elements. *Archives of Metallurgy and Materials*, *58*(4), 1415–1418. https://doi.org/10.2478/amm-2013-0186
36. Dul, S., Fambri, L., & Pegoretti, A. (2016). Fused deposition modelling with ABS–graphene nanocomposites. *Composites Part A: Applied Science and Manufacturing*, *85*, 181–191. https://doi.org/10.1016/j.compositesa.2016.03.013
37. *Extrudr PETG Black—3DJake Belgium*. (n.d.). Retrieved May 16, 2025, from https://www.3djake.be/nl-BE/extrudr/petg-zwart-3
38. Faidallah, R. F., Hanon, M. M., Szakál, Z., & Oldal, I. (2022a). Biodegradable Materials Used in FDM 3D Printing Technology: A Critical Review. *Journal of Modern Mechanical Engineering and Technology*, *9*, 90–105. https://doi.org/10.31875/2409-9848.2022.09.11
39. Faidallah, R. F., Hanon, M. M., Szakál, Z., & Oldal, I. (2022b). Biodegradable Materials Used in FDM 3D Printing Technology: A Critical Review. *Journal of Modern Mechanical Engineering and Technology*, *9*, 90–105.
40. Ferreira, R. T. L., Amatte, I. C., Dutra, T. A., & Bürger, D. (2017). Experimental characterization and micrography of 3D printed PLA and PLA reinforced with short carbon fibers. *Composites Part B: Engineering*, *124*, 88–100. https://doi.org/10.1016/j.compositesb.2017.05.013
41. Ficzere, P., Lukacs, N. L., & Borbas, L. (2021). The investigation of interlaminar failures caused by production parameters in case of additive manufactured polymers. *Polymers*, *13*(4), 556.
42. Garoushi, S., Säilynoja, E., Vallittu, P. K., & Lassila, L. (2013). Physical properties and depth of cure of a new short fiber reinforced composite. *Dental Materials*, *29*(8), 835–841.
43. Gibson, I., Rosen, D., Stucker, B., & Khorasani, M. (2021). *Additive manufacturing technologies* (Third edition). Springer.
44. Glasschroeder, J., Prager, E., & Zaeh, M. F. (2015). Powder-bed-based 3D-printing of function integrated parts. *Rapid Prototyping Journal*, *21*(2), 207–215. https://doi.org/10.1108/RPJ-12-2014-0172
45. Goh, G. D., Dikshit, V., Nagalingam, A. P., Goh, G. L., Agarwala, S., Sing, S. L., Wei, J., & Yeong, W. Y. (2018). Characterization of mechanical properties and fracture mode of additively manufactured carbon fiber and glass fiber reinforced thermoplastics. *Materials & Design*, *137*, 79–89. https://doi.org/10.1016/j.matdes.2017.10.021

46. Goh, G. D., Yap, Y. L., Agarwala, S., & Yeong, W. Y. (2019). Recent Progress in Additive Manufacturing of Fiber Reinforced Polymer Composite. *Advanced Materials Technologies*, *4*(1), 1800271. https://doi.org/10.1002/admt.201800271
47. Goh, G. D., & Yeong, W. Y. (2018). Mode I interlaminar fracture toughness of additively manufactured carbon fibre thermoplastic. *Proceedings of the 3rd International Conference on Progress in Additive Manufacturing*, 505–510.
48. Goryl, K., Pollák, M., Kočiško, M., & Korol', M. (2024). Comparison of PLA and PLA Carbon Fiber Materials on Tensile Test. In B. Gapiński, O. Ciszak, V. Ivanov, & J. M. Machado (Eds.), *Advances in Manufacturing IV* (pp. 73–82). Springer Nature Switzerland. https://doi.org/10.1007/978-3-031-56463-5_6
49. Griffini, G., Invernizzi, M., Levi, M., Natale, G., Postiglione, G., & Turri, S. (2016). 3D-printable CFR polymer composites with dual-cure sequential IPNs. *Polymer*, *91*, 174–179.
50. Guo, N., & Leu, M. C. (2013). Additive manufacturing: Technology, applications and research needs. *Frontiers of Mechanical Engineering*, *8*(3), 215–243. https://doi.org/10.1007/s11465-013-0248-8
51. Gupta, A., Hasanov, S., & Fidan, I. (2019). *Processing and Characterization of 3D-Printed Polymer Matrix Composites Reinforced with Discontinuous Fibers*. https://doi.org/10.26153/TSW/17341
52. Halip, J. A., Hua, L. S., Ashaari, Z., Tahir, P. M., Chen, L. W., & Anwar Uyup, M. K. (2019). Effect of treatment on water absorption behavior of natural fiber–reinforced polymer composites. In *Mechanical and Physical Testing of Biocomposites, Fibre-Reinforced Composites and Hybrid Composites* (pp. 141–156). Elsevier. https://doi.org/10.1016/B978-0-08-102292-4.00008-4
53. Hao, W., Liu, Y., Zhou, H., Chen, H., & Fang, D. (2018). Preparation and characterization of 3D printed continuous carbon fiber reinforced thermosetting composites. *Polymer Testing*, *65*, 29–34. https://doi.org/10.1016/j.polymertesting.2017.11.004
54. Hofstätter, T., Pedersen, D. B., Nielsen, J. S., Mischkot, M., & Hansen, H. N. (2016). Investigation of digital light processing using fibre-reinforced polymers. *Euspen's 16th International Conference & Exhibition*.
55. Hsueh, M.-H., Lai, C.-J., Wang, S.-H., Zeng, Y.-S., Hsieh, C.-H., Pan, C.-Y., & Huang, W.-C. (2021). Effect of printing parameters on the thermal and mechanical properties of 3d-printed pla and petg, using fused deposition modeling. *Polymers*, *13*(11), 1758.
56. International, A. (2007). *Standard test method for tensile properties of polymer matrix composite materials*. ASTM international.
57. ISO, B. (2009). 527-5. Plastics-Determination of tensile properties-Part 5: Test conditions for unidirectional fibre-reinforced plastic composites. *European Committee for Standardisation*.
58. ISO, E. (1997). 527-4. Plastics-Determination of tensile properties-Part 4: Test conditions for isotropic and orthotropic fibre-reinforced plastic composites. *International Organization for Standardization (ISO), Geneva, Switzerland*.
59. Iso, E. (2012a). 527-1. Plastics—Determination of tensile properties—Part 1: General principles. *International Organization of Standardization: Geneva, Switzerland*.
60. Iso, E. (2012b). 527-1. Plastics—Determination of tensile properties—Part 1: General principles. *International Organization of Standardization: Geneva, Switzerland*.
61. Ivey, M., Melenka, G. W., Carey, Jason. P., & Ayranci, C. (2017). Characterizing short-fiber-reinforced composites produced using additive manufacturing. *Advanced Manufacturing: Polymer & Composites Science*, *3*(3), 81–91. https://doi.org/10.1080/20550340.2017.1341125

62. Jasiuk, I., Abueidda, D. W., Kozuch, C., Pang, S., Su, F. Y., & McKittrick, J. (2018). An overview on additive manufacturing of polymers. *Jom*, *70*(3), 275–283.
63. Jiang, Y., & Raney, J. R. (2019). 3D Printing of Amylopectin-Based Natural Fiber Composites. *Advanced Materials Technologies*, *4*(11), 1900521. https://doi.org/10.1002/admt.201900521
64. Justo, J., Távara, L., García-Guzmán, L., & París, F. (2018). Characterization of 3D printed long fibre reinforced composites. *Composite Structures*, *185*, 537–548. https://doi.org/10.1016/j.compstruct.2017.11.052
65. Kabir, S. F., Mathur, K., & Seyam, A.-F. M. (2020). A critical review on 3D printed continuous fiber-reinforced composites: History, mechanism, materials and properties. *Composite Structures*, *232*, 111476.
66. Kang, J., Shangguan, H., Deng, C., Hu, Y., Yi, J., Wang, X., Zhang, X., & Huang, T. (2018). Additive manufacturing-driven mold design for castings. *Additive Manufacturing*, *22*, 472–478.
67. Kasala, S. (2018). *Recycled technical plastics as raw material for plastics and composite products*.
68. Kauffman, G. B. (2010). *Book Review of Polymer Data Handbook*. ACS Publications.
69. Kay, R. (2014). *Effect of raster orientation on the structural properties of components fabricated by fused deposition modeling*. The Ohio State University.
70. Kim, K., Park, J., Suh, J., Kim, M., Jeong, Y., & Park, I. (2017). 3D printing of multiaxial force sensors using carbon nanotube (CNT)/thermoplastic polyurethane (TPU) filaments. *Sensors and Actuators A: Physical*, *263*, 493–500.
71. Kladovasilakis, N., Charalampous, P., Tsongas, K., Kostavelis, I., Tzetzis, D., & Tzovaras, D. (2021). Experimental and Computational Investigation of Lattice Sandwich Structures Constructed by Additive Manufacturing Technologies. *Journal of Manufacturing and Materials Processing*, *5*(3), 95. https://doi.org/10.3390/jmmp5030095
72. Kumar, S., & Kruth, J.-P. (2010). Composites by rapid prototyping technology. *Materials & Design*, *31*(2), 850–856. https://doi.org/10.1016/j.matdes.2009.07.045
73. Kuo, C.-C., Liu, L.-C., Teng, W.-F., Chang, H.-Y., Chien, F.-M., Liao, S.-J., Kuo, W.-F., & Chen, C.-M. (2016). Preparation of starch/acrylonitrile-butadiene-styrene copolymers (ABS) biomass alloys and their feasible evaluation for 3D printing applications. *Composites Part B: Engineering*, *86*, 36–39.
74. Latha, G. M., Venkateswarlu, H., Krishnaraj, P., Allam, S. K., Anusree, K. V., & Krishna, A. (2024). Science and Technology of Additive Manufacturing Applied to Geotechnical Engineering. *Indian Geotechnical Journal*, *54*(1), 85–95. https://doi.org/10.1007/s40098-023-00777-6
75. Le Duigou, A., Castro, M., Bevan, R., & Martin, N. (2016). 3D printing of wood fibre biocomposites: From mechanical to actuation functionality. *Materials & Design*, *96*, 106–114. https://doi.org/10.1016/j.matdes.2016.02.018
76. Lee, J.-Y., An, J., & Chua, C. K. (2017). Fundamentals and applications of 3D printing for novel materials. *Applied Materials Today*, *7*, 120–133.
77. Li, J. H., Huang, X. D., Durandet, Y., & Ruan, D. (2021). A review of the mechanical properties of additively manufactured fiber reinforced composites. *IOP Conference Series: Materials Science and Engineering*, *1067*(1), 012105. https://doi.org/10.1088/1757-899X/1067/1/012105

78. Li, N., Li, Y., & Liu, S. (2016a). Journal of Materials Processing Technology Rapid prototyping of continuous carbon fiber reinforced polylactic acid composites by 3D printing'. *J. Mater. Process. Technol.*, *238*, 218–225.
79. Li, N., Li, Y., & Liu, S. (2016b). Rapid prototyping of continuous carbon fiber reinforced polylactic acid composites by 3D printing. *Journal of Materials Processing Technology*, *238*, 218–225. https://doi.org/10.1016/j.jmatprotec.2016.07.025
80. Liao, G., Li, Z., Cheng, Y., Xu, D., Zhu, D., Jiang, S., Guo, J., Chen, X., Xu, G., & Zhu, Y. (2018). Properties of oriented carbon fiber/polyamide 12 composite parts fabricated by fused deposition modeling. *Materials & Design*, *139*, 283–292. https://doi.org/10.1016/j.matdes.2017.11.027
81. Ligon, S. C., Liska, R., Stampfl, J., Gurr, M., & Mülhaupt, R. (2017). Polymers for 3D Printing and Customized Additive Manufacturing. *Chemical Reviews*, *117*(15), 10212–10290. https://doi.org/10.1021/acs.chemrev.7b00074
82. Liu, Y., Wang, W., & Zhang, L.-C. (2017). Additive manufacturing techniques and their biomedical applications. *Family Medicine and Community Health*, *5*(4), 286–298. https://doi.org/10.15212/FMCH.2017.0110
83. Liu, Z., Wang, Y., Wu, B., Cui, C., Guo, Y., & Yan, C. (2019). A critical review of fused deposition modeling 3D printing technology in manufacturing polylactic acid parts. *The International Journal of Advanced Manufacturing Technology*, *102*(9–12), 2877–2889. https://doi.org/10.1007/s00170-019-03332-x
84. Liu, Z., Zhang, L., Yu, E., Ying, Z., Zhang, Y., Liu, X., & Eli, W. (2015). Modification of Glass Fiber Surface and Glass Fiber Reinforced Polymer Composites Challenges and Opportunities: From Organic Chemistry Perspective. *Current Organic Chemistry*, *19*(11), 991–1010. https://doi.org/10.2174/1385272819111506101009l4
85. Low, Z.-X., Chua, Y. T., Ray, B. M., Mattia, D., Metcalfe, I. S., & Patterson, D. A. (2017). Perspective on 3D printing of separation membranes and comparison to related unconventional fabrication techniques. *Journal of Membrane Science*, *523*, 596–613. https://doi.org/10.1016/j.memsci.2016.10.006
86. Lu, C., Qi, M., Islam, S., Chen, P., Gao, S., Xu, Y., & Yang, X. (2018). Mechanical performance of 3D-printing plastic honeycomb sandwich structure. *International Journal of Precision Engineering and Manufacturing-Green Technology*, *5*(1), 47–54. https://doi.org/10.1007/s40684-018-0005-x
87. Mark, J. E. (Ed.). (2009). *Polymer data handbook* (2nd ed). Oxford University Press.
88. *Markforged Composite and Metal 3D Printers*. (n.d.). Retrieved April 26, 2025, from https://www.freedee.hu/3d-nyomtatok/markforged/
89. Matsuzaki, R., Ueda, M., Namiki, M., Jeong, T.-K., Asahara, H., Horiguchi, K., Nakamura, T., Todoroki, A., & Hirano, Y. (2016). Three-dimensional printing of continuous-fiber composites by in-nozzle impregnation. *Scientific Reports*, *6*(1), 23058. https://doi.org/10.1038/srep23058
90. Matthews, F. L., & Rawlings, R. D. (1999). *Composite materials: Engineering and science*. Woodhead Publishing.
91. Mazzanti, V., Malagutti, L., & Mollica, F. (2019). FDM 3D printing of polymers containing natural fillers: A review of their mechanical properties. *Polymers*, *11*(7), 1094.
92. Melenka, G. W., Cheung, B. K. O., Schofield, J. S., Dawson, M. R., & Carey, J. P. (2016). Evaluation and prediction of the tensile properties of continuous fiber-reinforced 3D printed

structures. *Composite Structures*, *153*, 866–875. https://doi.org/10.1016/j.compstruct.2016.07.018
93. Monaghan, T., Capel, A. J., Christie, S. D., Harris, R. A., & Friel, R. J. (2015). Solid-state additive manufacturing for metallized optical fiber integration. *Composites Part A: Applied Science and Manufacturing*, *76*, 181–193.
94. Mostafa, N., Syed, H. M., Igor, S., & Andrew, G. (2009). A study of melt flow analysis of an ABS-Iron composite in fused deposition modelling process. *Tsinghua Science & Technology*, *14*, 29–37.
95. N. Turner, B., Strong, R., & A. Gold, S. (2014). A review of melt extrusion additive manufacturing processes: I. Process design and modeling. *Rapid Prototyping Journal*, *20*(3), 192–204. https://doi.org/10.1108/RPJ-01-2013-0012
96. Nancharaiah, T., Raju, D. R., & Raju, V. R. (2010). An experimental investigation on surface quality and dimensional accuracy of FDM components. *International Journal on Emerging Technologies*, *1*(2), 106–111.
97. Nandi, C., Caspi, A., Grossman, D., & Tatlock, Z. (2017). Programming language tools and techniques for 3D printing. *2nd Summit on Advances in Programming Languages (SNAPL 2017)*.
98. Nassar, M., El Farahaty, M. A., Ibrahim, S., & Hassan, Y. R. (2019). Design of 3D filament extruder for Fused Deposition Modeling (FDM) additive manufacturing. *International Design Journal*, *9*(4), 55–62.
99. Nazeer, A. (2018). A Review on Secondary Process of Hot Extrusion on Aluminum Metal Matrix Composite. *Juniper Online Journal Material Science*, *4*(4). https://doi.org/10.19080/JOJMS.2018.04.555642
100. Ning, F., Cong, W., Hu, Y., & Wang, H. (2017). Additive manufacturing of carbon fiber-reinforced plastic composites using fused deposition modeling: Effects of process parameters on tensile properties. *Journal of Composite Materials*, *51*(4), 451–462. https://doi.org/10.1177/0021998316646169
101. Ning, F., Cong, W., Qiu, J., Wei, J., & Wang, S. (2015). Additive manufacturing of carbon fiber reinforced thermoplastic composites using fused deposition modeling. *Composites Part B: Engineering*, *80*, 369–378.
102. Niu, C., Luan, C., Shen, H., Song, X., Fu, J., Zhang, L., Sun, Y., Xu, G., & Ruan, Z. (2022). Tunable soft–stiff hybridized fiber-reinforced thermoplastic composites using controllable multimaterial additive manufacturing technology. *Additive Manufacturing*, *55*, 102836. https://doi.org/10.1016/j.addma.2022.102836
103. Nukala, S. G., Kong, I., Kakarla, A. B., Patel, V. I., & Abuel-Naga, H. (2023). Simulation of Wood Polymer Composites with Finite Element Analysis. *Polymers*, *15*(9), 1977. https://doi.org/10.3390/polym15091977
104. Oksman, K., Mathew, A. P., Bondeson, D., & Kvien, I. (2006). Manufacturing process of cellulose whiskers/polylactic acid nanocomposites. *Composites Science and Technology*, *66*(15), 2776–2784. https://doi.org/10.1016/j.compscitech.2006.03.002
105. Onwubolu, G. C., & Rayegani, F. (2014). Characterization and optimization of mechanical properties of ABS parts manufactured by the fused deposition modelling process. *International Journal of Manufacturing Engineering*, *2014*.
106. Palaniyappan, S., Annamalai, G., Sivakumar, N. K., & Muthu, P. (2023). Development of functional gradient multi-material composites using Poly Lactic Acid and walnut shell

reinforced Poly Lactic Acid filaments by fused filament fabrication technology. *Journal of Building Engineering*, *65*, 105746. https://doi.org/10.1016/j.jobe.2022.105746
107. Park, S., & Fu, K. (Kelvin). (2021). Polymer-based filament feedstock for additive manufacturing. *Composites Science and Technology*, *213*, 108876. https://doi.org/10.1016/j.compscitech.2021.108876
108. Park, S., Shou, W., Makatura, L., Matusik, W., & Fu, K. (Kelvin). (2022). 3D printing of polymer composites: Materials, processes, and applications. *Matter*, *5*(1), 43–76. https://doi.org/10.1016/j.matt.2021.10.018
109. Penumakala, P. K., Santo, J., & Thomas, A. (2020). A critical review on the fused deposition modeling of thermoplastic polymer composites. *Composites Part B: Engineering*, *201*, 108336.
110. Pu'ad, N. M., Haq, R. A., Noh, H. M., Abdullah, H. Z., Idris, M. I., & Lee, T. C. (2020). Review on the fabrication of fused deposition modelling (FDM) composite filament for biomedical applications. *Materials Today: Proceedings*, *29*, 228–232.
111. Rafsanjani, A., Akbarzadeh, A., & Pasini, D. (2015). Snapping Mechanical Metamaterials under Tension. *Advanced Materials*, *27*(39), 5931–5935. https://doi.org/10.1002/adma.201502809
112. Rahim, T. N. A. T., Abdullah, A. M., & Md Akil, H. (2019). Recent developments in fused deposition modeling-based 3D printing of polymers and their composites. *Polymer Reviews*, *59*(4), 589–624.
113. Rangisetty, S., & Peel, L. D. (2017). The Effect of Infill Patterns and Annealing on Mechanical Properties of Additively Manufactured Thermoplastic Composites. *Volume 1: Development and Characterization of Multifunctional Materials; Mechanics and Behavior of Active Materials; Bioinspired Smart Materials and Systems; Energy Harvesting; Emerging Technologies*, V001T08A017. https://doi.org/10.1115/SMASIS2017-4011
114. Rauwendaal, C. (2014). *Polymer extrusion*. Carl Hanser Verlag GmbH Co KG.
115. *ReForm—rPLA Black 1,75 mm*. (n.d.). 3DJake België. Retrieved May 16, 2025, from https://www.3djake.be/nl-BE/formfutura/reformtm-rpla-black
116. Regassa, Y., Lemu, H. G., & Sirabizuh, B. (2019). Trends of using polymer composite materials in additive manufacturing. *IOP Conference Series: Materials Science and Engineering*, *659*(1), 012021. https://doi.org/10.1088/1757-899X/659/1/012021
117. Salcedo, E., Baek, D., Berndt, A., & Ryu, J. E. (2018). Simulation and validation of three dimension functionally graded materials by material jetting. *Additive Manufacturing*, *22*, 351–359. https://doi.org/10.1016/j.addma.2018.05.027
118. Salifu, S., Ogunbiyi, O., & Olubambi, P. A. (2022). Potentials and challenges of additive manufacturing techniques in the fabrication of polymer composites. *The International Journal of Advanced Manufacturing Technology*, *122*(2), 577–600. https://doi.org/10.1007/s00170-022-09976-6
119. Samali, B., Nemati, S., Sharafi, P., Tahmoorian, F., & Sanati, F. (2019). Structural Performance of Polyurethane Foam-Filled Building Composite Panels: A State-Of-The-Art. *Journal of Composites Science*, *3*(2), 40. https://doi.org/10.3390/jcs3020040
120. Sang, L., Han, S., Peng, X., Jian, X., & Wang, J. (2019). Development of 3D-printed basalt fiber reinforced thermoplastic honeycombs with enhanced compressive mechanical properties. *Composites Part A: Applied Science and Manufacturing*, *125*, 105518. https://doi.org/10.1016/j.compositesa.2019.105518

121. Serrano, M. C., Gutiérrez, M. C., & del Monte, F. (2014). Role of polymers in the design of 3D carbon nanotube-based scaffolds for biomedical applications. *Progress in Polymer Science*, *39*(7), 1448–1471.
122. Shabdin, M. K., Rahman, A., Azizi, M., Mazlan, S. A., Hapipi, N. M., Adiputra, D., Aziz, A., Aishah, S., Bahiuddin, I., & Choi, S.-B. (2019). Material characterizations of gr-based magnetorheological elastomer for possible sensor applications: Rheological and resistivity properties. *Materials*, *12*(3), 391.
123. Shahrubudin, N., Lee, T. C., & Ramlan, R. (2019). An Overview on 3D Printing Technology: Technological, Materials, and Applications. *Procedia Manufacturing*, *35*, 1286–1296. https://doi.org/10.1016/j.promfg.2019.06.089
124. Shilkrut, D. (2002). Spherical Caps Subjected to Multi-Parameter Loading. The Deformation Map. Influence of the Loading Path on the Cap's Behavior. Thermo-Elastic Deformations. In *Studies in Applied Mechanics* (Vol. 48, pp. 215–288). Elsevier.
125. Shofner, M. L., Rodríguez-Macías, F. J., Vaidyanathan, R., & Barrera, E. V. (2003). Single wall nanotube and vapor grown carbon fiber reinforced polymers processed by extrusion freeform fabrication. *Composites Part A: Applied Science and Manufacturing*, *34*(12), 1207–1217. https://doi.org/10.1016/j.compositesa.2003.07.002
126. Shubhra, Q. T., Alam, A., & Quaiyyum, M. (2013). Mechanical properties of polypropylene composites: A review. *Journal of Thermoplastic Composite Materials*, *26*(3), 362–391. https://doi.org/10.1177/0892705711428659
127. Sonnenschein, R., Gajdosova, K., & Holly, I. (2016). FRP Composites and their Using in the Construction of Bridges. *Procedia Engineering*, *161*, 477–482. https://doi.org/10.1016/j.proeng.2016.08.665
128. Spinelli, G., Kotsilkova, R., Ivanov, E., Petrova-Doycheva, I., Menseidov, D., Georgiev, V., Di Maio, R., & Silvestre, C. (2019). Effects of filament extrusion, 3D printing and hot-pressing on electrical and tensile properties of poly (lactic) acid composites filled with carbon nanotubes and graphene. *Nanomaterials*, *10*(1), 35.
129. Sugiyama, K., Matsuzaki, R., Ueda, M., Todoroki, A., & Hirano, Y. (2018). 3D printing of composite sandwich structures using continuous carbon fiber and fiber tension. *Composites Part A: Applied Science and Manufacturing*, *113*, 114–121. https://doi.org/10.1016/j.compositesa.2018.07.029
130. Sun, Q., Rizvi, G. M., Bellehumeur, C. T., & Gu, P. (2008). Effect of processing conditions on the bonding quality of FDM polymer filaments. *Rapid Prototyping Journal*, *14*(2), 72–80. https://doi.org/10.1108/13552540810862028
131. Tan, D. K., Maniruzzaman, M., & Nokhodchi, A. (2018). Advanced pharmaceutical applications of hot-melt extrusion coupled with fused deposition modelling (FDM) 3D printing for personalised drug delivery. *Pharmaceutics*, *10*(4), 203.
132. Tatlıer, M. S. (2022). A comparative analysis of the in-plane energy absorption capacities of auxetic structures. *Transactions of the Canadian Society for Mechanical Engineering*, *46*(2), 216–224. https://doi.org/10.1139/tcsme-2021-0112
133. Technologies, A. C. F. on A. M., & Terminology, A. C. F. on A. M. T. S. F. 91 on. (2012). *Standard terminology for additive manufacturing technologies*. Astm International.
134. Tekinalp, H. L., Kunc, V., Velez-Garcia, G. M., Duty, C. E., Love, L. J., Naskar, A. K., Blue, C. A., & Ozcan, S. (2014). Highly oriented carbon fiber–polymer composites via additive manufacturing. *Composites Science and Technology*, *105*, 144–150. https://doi.org/10.1016/j.compscitech.2014.10.009

135. Terekhina, S., Skornyakov, I., Tarasova, T., & Egorov, S. (2019). Effects of the infill density on the mechanical properties of nylon specimens made by filament fused fabrication. *Technologies*, *7*(3), 57.
136. Tian, X., Liu, T., Yang, C., Wang, Q., & Li, D. (2016). Interface and performance of 3D printed continuous carbon fiber reinforced PLA composites. *Composites Part A: Applied Science and Manufacturing*, *88*, 198–205. https://doi.org/10.1016/j.compositesa.2016.05.032
137. Tuan Rahim, T. N. A., Abdullah, A. M., Md Akil, H., Mohamad, D., & Rajion, Z. A. (2015). Preparation and characterization of a newly developed polyamide composite utilising an affordable 3D printer. *Journal of Reinforced Plastics and Composites*, *34*(19), 1628–1638.
138. Tymrak, B. M., Kreiger, M., & Pearce, J. M. (2014). Mechanical properties of components fabricated with open-source 3-D printers under realistic environmental conditions. *Materials & Design*, *58*, 242–246. https://doi.org/10.1016/j.matdes.2014.02.038
139. Vakharia, V. S., Kuentz, L., Salem, A., Halbig, M. C., Salem, J. A., & Singh, M. (2021). Additive Manufacturing and Characterization of Metal Particulate Reinforced Polylactic Acid (PLA) Polymer Composites. *Polymers*, *13*(20), 3545. https://doi.org/10.3390/polym13203545
140. Van der Zwaag, S., Grande, A. M., Post, W., Garcia, S. J., & Bor, T. C. (2014). Review of current strategies to induce self-healing behaviour in fibre reinforced polymer based composites. *Materials Science and Technology*, *30*(13), 1633–1641.
141. Van Krevelen, D. W., & Te Nijenhuis, K. (2009). *Properties of polymers: Their correlation with chemical structure; their numerical estimation and prediction from additive group contributions*. Elsevier.
142. Wang, J., Goyanes, A., Gaisford, S., & Basit, A. W. (2016). Stereolithographic (SLA) 3D printing of oral modified-release dosage forms. *International Journal of Pharmaceutics*, *503*(1–2), 207–212. https://doi.org/10.1016/j.ijpharm.2016.03.016
143. Wang, K., Li, S., Rao, Y., Wu, Y., Peng, Y., Yao, S., Zhang, H., & Ahzi, S. (2019). Flexure behaviors of ABS-based composites containing carbon and Kevlar fibers by material extrusion 3D printing. *Polymers*, *11*(11), 1878.
144. Wang, P., Zou, B., Xiao, H., Ding, S., & Huang, C. (2019). Effects of printing parameters of fused deposition modeling on mechanical properties, surface quality, and microstructure of PEEK. *Journal of Materials Processing Technology*, *271*, 62–74.
145. Wang, X., Jiang, M., Zhou, Z., Gou, J., & Hui, D. (2017). 3D printing of polymer matrix composites: A review and prospective. *Composites Part B: Engineering*, *110*, 442–458.
146. Wang, X., Zhao, L., Fuh, J. Y. H., & Lee, H. P. (2019). Effect of Porosity on Mechanical Properties of 3D Printed Polymers: Experiments and Micromechanical Modeling Based on X-ray Computed Tomography Analysis. *Polymers*, *11*(7), 1154. https://doi.org/10.3390/polym11071154
147. Wang, Y., Müller, W.-D., Rumjahn, A., & Schwitalla, A. (2020). Parameters influencing the outcome of additive manufacturing of tiny medical devices based on PEEK. *Materials*, *13*(2), 466.
148. Wei, X., Li, D., Jiang, W., Gu, Z., Wang, X., Zhang, Z., & Sun, Z. (2015). 3D Printable Graphene Composite. *Scientific Reports*, *5*(1), 11181. https://doi.org/10.1038/srep11181
149. Wimpenny, D. I., Pandey, P. M., & Kumar, L. J. (Eds.). (2017). *Advances in 3D Printing & Additive Manufacturing Technologies*. Springer Singapore. https://doi.org/10.1007/978-981-10-0812-2

150. Wohlers, T., & Gornet, T. (2011). *" History of Additive Manufacturing," Wohlers Report: Additive Manufacturing and 3D Printing State of the Industry Annual Worldwide Progress Report*.
151. Wohlers, T., & Gornet, T. (2014). History of additive manufacturing. *Wohlers Report*, *24*(2014), 118.
152. Yang, C., Tian, X., Liu, T., Cao, Y., & Li, D. (2017). 3D printing for continuous fiber reinforced thermoplastic composites: Mechanism and performance. *Rapid Prototyping Journal*, *23*(1), 209–215. https://doi.org/10.1108/RPJ-08-2015-0098
153. Yang, S., Qi, C., Wang, D., Gao, R., Hu, H., & Shu, J. (2013). A Comparative Study of Ballistic Resistance of Sandwich Panels with Aluminum Foam and Auxetic Honeycomb Cores. *Advances in Mechanical Engineering*, *5*, 589216. https://doi.org/10.1155/2013/589216
154. Yermurat, B., Seçgin, Ö., & Taşdemir, V. (2023). Multi-material additive manufacturing: Investigation of the combined use of ABS and PLA in the same structure. *Materials Testing*, *65*(7), 1119–1126. https://doi.org/10.1515/mt-2022-0368
155. Yetgin, S. H. (2020). Tribological properties of compatabilizer and graphene oxide-filled polypropylene nanocomposites. *Bulletin of Materials Science*, *43*(1), 1–8.
156. Yu, J., Wang, E., Li, J., & Zheng, Z. (2008). Static and low-velocity impact behavior of sandwich beams with closed-cell aluminum-foam core in three-point bending. *International Journal of Impact Engineering*, *35*(8), 885–894. https://doi.org/10.1016/j.ijimpeng.2008.01.006
157. Zaharia, S. M., Enescu, L. A., & Pop, M. A. (2020). Mechanical performances of lightweight sandwich structures produced by material extrusion-based additive manufacturing. *Polymers*, *12*(8), 1740.
158. Zhang, J., Chevali, V. S., Wang, H., & Wang, C.-H. (2020). Current status of carbon fibre and carbon fibre composites recycling. *Composites Part B: Engineering*, *193*, 108053. https://doi.org/10.1016/j.compositesb.2020.108053
159. Zhang, X., Ding, H., An, L., & Wang, X. (2015). Numerical Investigation on Dynamic Crushing Behavior of Auxetic Honeycombs with Various Cell-Wall Angles. *Advances in Mechanical Engineering*, *7*(2), 679678. https://doi.org/10.1155/2014/679678
160. Zhang, Z., Sun, C., Xu, X., & Liu, L. (2018). Surface quality and forming characteristics of thin-wall aluminium alloy parts manufactured by laser assisted MIG arc additive manufacturing. *International Journal of Lightweight Materials and Manufacture*, *1*(2), 89–95. https://doi.org/10.1016/j.ijlmm.2018.03.005
161. Zhong, W., Li, F., Zhang, Z., Song, L., & Li, Z. (2001a). Research on rapid-prototyping/part manufacturing (RP&M) for the continuous fiber reinforced composite. *Materials and Manufacturing Processes*, *16*(1), 17–26.
162. Zhong, W., Li, F., Zhang, Z., Song, L., & Li, Z. (2001b). Short fiber reinforced composites for fused deposition modeling. *Materials Science and Engineering: A*, *301*(2), 125–130. https://doi.org/10.1016/S0921-5093(00)01810-4
163. Zied, K., Osman, M., & Elmahdy, T. (2015). Enhancement of the in-plane stiffness of the hexagonal re-entrant auxetic honeycomb cores: Enhancement of in-plane stiffness of hexagonal auxetic honeycombs. *Physica Status Solidi (b)*, *252*(12), 2685–2692. https://doi.org/10.1002/pssb.201552164
164. Zienkiewicz, O. C., & Taylor, R. L. (2005). *The finite element method for solid and structural mechanics*. Elsevier.

165. Zindani, D., & Kumar, K. (2019). An insight into additive manufacturing of fiber reinforced polymer composite. *International Journal of Lightweight Materials and Manufacture*, *2*(4), 267–278. https://doi.org/10.1016/j.ijlmm.2019.08.004
166. Zoumaki, M., Mansour, M. T., Tsongas, K., Tzetzis, D., & Mansour, G. (2022). Mechanical Characterization and Finite Element Analysis of Hierarchical Sandwich Structures with PLA 3D-Printed Core and Composite Maize Starch Biodegradable Skins. *Journal of Composites Science*, *6*(4), 118. https://doi.org/10.3390/jcs6040118

A2: Publications related to the dissertation

Refereed papers in foreign languages:

1. **Faidallah, R. F**., Szakál, Z., & Oldal, I. (2021). Introduction to 3D printing: Techniques, materials and agricultural applications. *Hungarian Agricultural Engineering*, *40*, 47–58. https://doi.org/10.17676/HAE.2021.40.47

2. **Faidallah, R. F**., Hanon, M. M., Szakál, Z., & Oldal, I. (2022). Biodegradable Materials Used in FDM 3D Printing Technology: A Critical Review. *Journal of Modern Mechanical Engineering and Technology*, *9*, 90–105. DOI: 10.31875/2409-9848.2022.09.11

3. **Faidallah, R. F**., Hanon, M. M., Szakál, Z., & Oldal, I. (2023). Study of the Mechanical Characteristics of Sandwich Structures FDM 3D-printed. *Acta Polytechnica Hungarica*, *20*(6). DOI: 10.12700/APH.20.6.2023.6.1

4. **Faidallah, R. F**., Hanon, M. M., Vashist, V., Habib, A., Szakál, Z., & Oldal, I. (2023b). Effect of Different Standard Geometry Shapes on the Tensile Properties of 3D-Printed Polymer. *Polymers*, *15*(14), 3029. https://doi.org/10.3390/polym15143029

5. **Faidallah, R. F**., Hanon, M. M., Szakál, Z., & Oldal, I. (2024). Mechanical characterization of 3D-Printed carbon fiber-reinforced polymer composites and pure polymers: Tensile and compressive behavior analysis. *International Review of Applied Sciences and Engineering*. https://doi.org/10.1556/1848.2024.00796

6. **Faidallah, R. F.,** Abd-El Nabi, A. M., Hanon, M. M., Szakál, Z., & Oldal, I. (2024). Compressive and bending properties of 3D-printed wood/PLA composites with Re-entrant honeycomb core. *Results in Engineering*, *24*, 103023. https://doi.org/10.1016/j.rineng.2024.103023

7. **Faidallah, R. F,** M. Hanon, N Salman, Ibrahim Y, Noman MD, T Gaaz T, Szakál, Z., & Oldal, I. Oldal. (2024). Development of Fiber-Reinforced Polymer Composites for Additive Manufacturing and Multi-Material Structures in Sustainable Applications, . *Processes*, *12*(10), 2217. https://doi.org/10.3390/pr12102217

8. N Salman, **Faidallah, R. F**, M. Hanon. (2024). Review of sustainable 3D printing criteria using FDM technology and their settings impact on mechanical properties of additively manufactured elements, IOP Conference Series: Earth and Environmental Science, Accepted, in process

9. Vashist, V., **Faidallah, R. F**., Szakál, Z., & Oldal, I.(2024). Influence of Process Parameters on the Mechanical Properties of 3D printed Metallic Specimens of Steel 1.2709 and 1.4542, polymer, under review.

A3: Tensile stress-strain curves of standard geometry shapes specimens

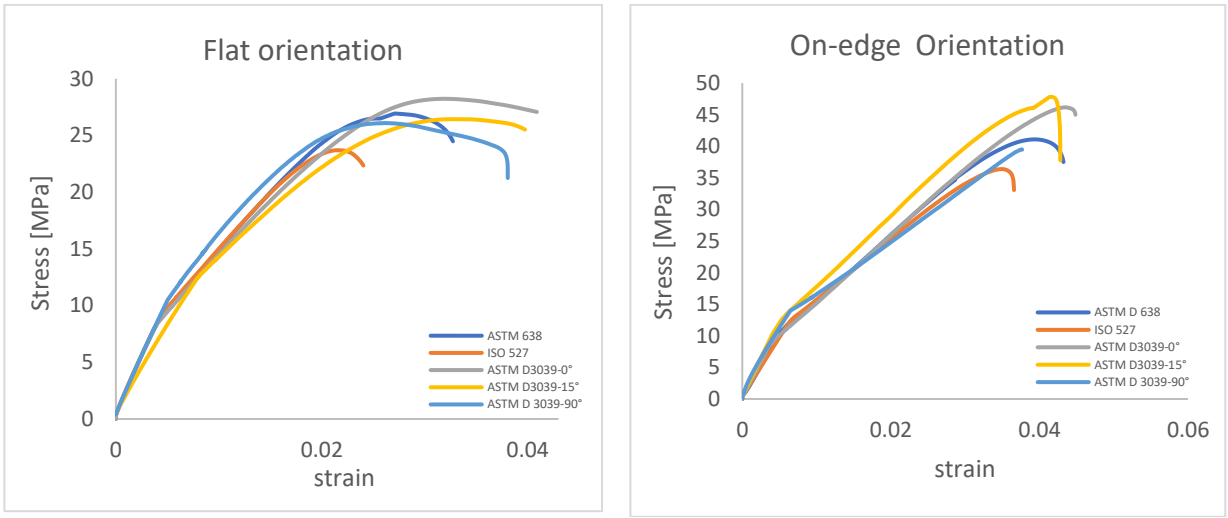

(a) (b)

Fig. 8.1 Tensile stress-strain curves of standard geometry shapes specimens for (a) flat building orientation and (b) on-edge orientation.

A4: Comparison of tested wood/PLA sandwich structure and simulated force-displacement curves

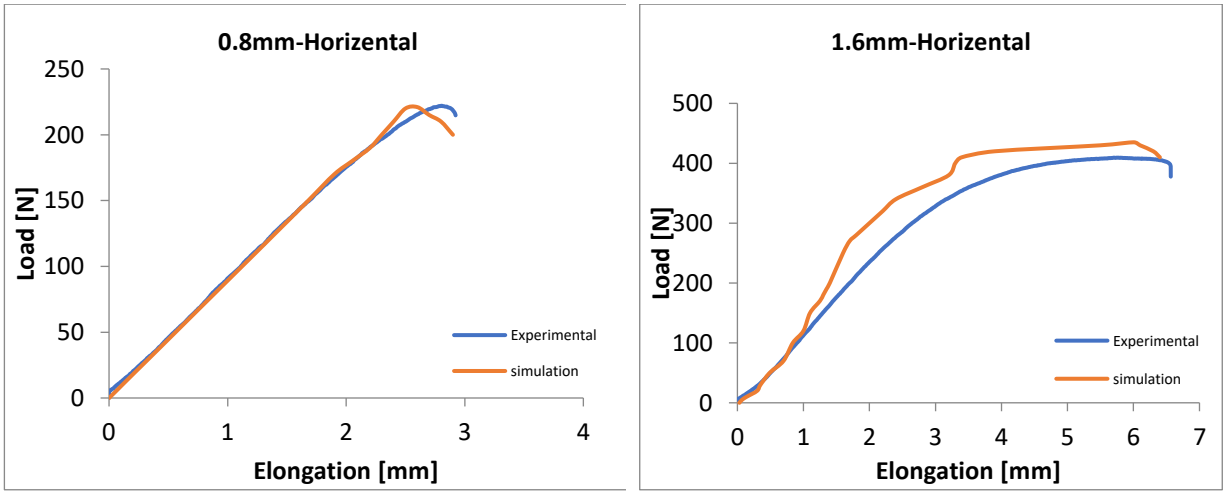

(a) (b)

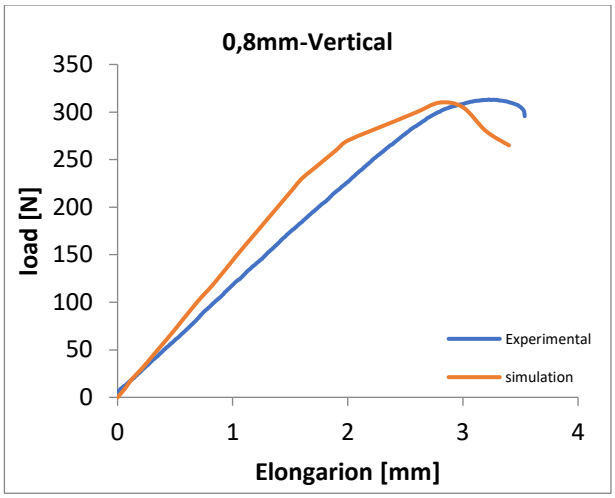

(c)

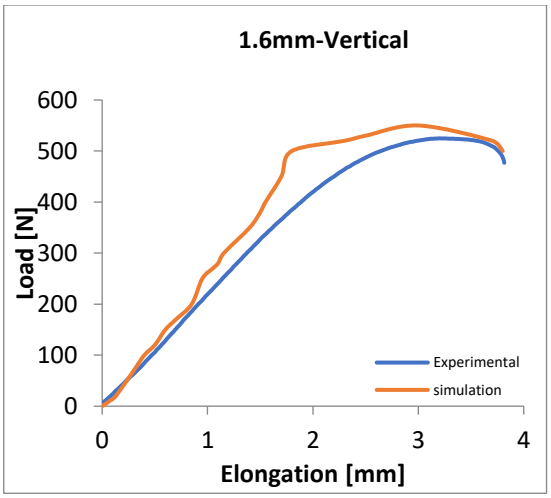

(d)

Fig.8.2 Comparison of experimental and simulated force-displacement: (a) 0.8mm-Horizental, (b) 1.6mm-Horizental, (c) 0.8mm-Vertical, (d) 1.6mm-Vertical

10. ACKNOWLEDGEMENT

I would like to express my sincere gratitude for my supervisor Dr. Oldal István, and Dr. Zoltán Szakál for their guidance and support throughout my PhD journey which started in 2021. Their invaluable insights and expertise have been instrumental in shaping my research and pushing me to strive for excellence.

This work has been supported financially by the Stipendium Hungaricum Scholarship Programme and accomplished under the direction of the Mechanical Engineering Doctoral School at MATE (Szent István University formerly), Gödöllő, Hungary.

I would like to extend my sincere gratitude to Prof. Gábor Kalácska, the current head of the Mechanical Engineering Doctoral School.Prof. In addition, I want to express my gratitude and appreciation for Dr. Seres István, whose suggestions, and support throughout my study have facilitated the fulfillment of all requirements for obtaining this PhD. In addition

I would also like to thank the faculty and staff at The Hungarian University of Agriculture and Life Sciences for providing me with the resources and facilities necessary to carry out my research. Their support and encouragement have been a constant source of motivation.

I am deeply grateful to my family (brothers and sister), especially my beloved father and mother, for their unwavering love, support, and encouragement throughout this challenging journey. Their constant belief in me, even during the hardest moments, gave me the strength to keep moving forward.

I am profoundly grateful to my aunt's family. Without their generosity, unwavering support, and the peaceful environment they offered, especially thanks to Zeena, I would not have been able to concentrate or complete my research. Despite their own busy lives, they continuously looked after me with warmth and care. I will always be thankful for their kindness and presence throughout this journey.

I extend my heartfelt gratitude to my dear friend Baraah, who has been like a sister and a steadfast source of strength throughout this journey. Her unwavering support, thoughtful encouragement, and genuine belief in my potential have been a constant reminder to persevere and take pride in my work. Her presence has been both grounding and inspiring, for which I am deeply thankful.

I would like to express my sincere appreciation to Simáné Dolányi Edit, the International PhD Coordinator at the University's Doctoral and Ms. Zsuzsanna Tassy, who deserves special recognition for their invaluable support and assistance throughout my PhD studies. It's difficult to put into words just how grateful I am for the guidance and help that they have provided me with.

Thank you once again for your support and guidance. I will always be grateful for your contribution to my academic and personal growth.

Sincerely,

Gödöllő, 18. 05. 2025

Rawabe Fatima Faidallah